



CAN UNCLASSIFIED



DRDC | RDDC
technologysciencetechnologie

Simulation of Raw Digital Signals Received by Space-Based Synthetic Aperture Radar for use in Jamming Studies

Alan D. Thomson
DRDC – Ottawa Research Centre

Defence Research and Development Canada

Scientific Report

DRDC-RDDC-2018-R297

June 2019

CAN UNCLASSIFIED

IMPORTANT INFORMATIVE STATEMENTS

This document was reviewed for Controlled Goods by Defence Research and Development Canada (DRDC) using the Schedule to the *Defence Production Act*.

Disclaimer: This publication was prepared by Defence Research and Development Canada an agency of the Department of National Defence. The information contained in this publication has been derived and determined through best practice and adherence to the highest standards of responsible conduct of scientific research. This information is intended for the use of the Department of National Defence, the Canadian Armed Forces ("Canada") and Public Safety partners and, as permitted, may be shared with academia, industry, Canada's allies, and the public ("Third Parties"). Any use by, or any reliance on or decisions made based on this publication by Third Parties, are done at their own risk and responsibility. Canada does not assume any liability for any damages or losses which may arise from any use of, or reliance on, the publication.

Endorsement statement: This publication has been peer-reviewed and published by the Editorial Office of Defence Research and Development Canada, an agency of the Department of National Defence of Canada. Inquiries can be sent to: Publications.DRDC-RDDC@drdc-rddc.gc.ca.

Abstract

A simulation of digital signals produced by a space-based Synthetic Aperture Radar (SAR) receiver is developed to provide a source of raw signal data that can be used to assess the vulnerability of space-based SAR to jamming and to investigate protection measures that may allow space-based SAR to operate in a contested electromagnetic environment. Key features of the simulation are a flexible time-domain approach, rotating spheroidal Earth geometry, calculation of absolute signal magnitudes, and the ability to generate large scenes. These are required so that jamming signals with specific quantitative properties (e.g., transmitted power) can be easily introduced into the simulation environment for specific geometries of interest and so that the effects of the jamming can be properly assessed in a quantitative fashion. The simulation uses the metadata of an actual space-based SAR collection to define the geometry for a given case. The image data corresponding to the real SAR collection is used to define the Earth surface reflectivity field that is measured by the simulated space-based SAR. Signal data corresponding to the surface of the earth, radar system noise, and test targets are generated, coherently combined, and converted into digital signals that can be processed using SAR image formation algorithms. An option to decompress and scale real, raw, range-compressed signals, measured by the RADARSAT-2 MODEX mode and combine them with test target signals is also developed. The scaling of the real data is required to adjust the absolute magnitudes of data measured in the real world to the levels that would be measured in the simulated environment. This option allows the validity of the simulated signals to be assessed through comparison with real data. The accuracy of the simulation is evaluated by comparing the properties of simulated signals and images with theoretical expectations and with the properties of real signal and image data. Good agreement is achieved for all aspects compared. This provides confidence that the simulated signals effectively approximate realistic raw received SAR signals and that the simulation can be used for its stated purpose.

Significance to defence and security

The Canadian space-based synthetic aperture radar systems, RADARSAT and RADARSAT-2, have provided Canadian government departments with a variety of products that aid maritime surveillance, ice monitoring, disaster management, environmental monitoring, resource management, and mapping. Some of these capabilities cannot currently be provided reliably and affordably through other means. Canada is now in the process of developing the RADARSAT Constellation Mission, which will be owned by the Government of Canada. This system will host synthetic aperture radars on multiple satellites. Capabilities such as ship detection, classification, and monitoring that are provided through space-based synthetic aperture radar are extremely important to the Department of National Defence's maritime domain awareness mission. Therefore, space-based synthetic aperture radar represents a strategic national capability that Canada depends upon now and will continue to depend upon in the future. The degradation of space-based synthetic aperture radar capabilities is possible through jamming, and research in this area is discussed in the open literature. Consequently, there is a need to make space-based synthetic aperture radar more resilient to such intentional interference. This research provides a tool for examining different approaches for mitigating the effects of jamming on space-based synthetic aperture radar.

Résumé

La simulation des signaux numériques produits par un récepteur radar à synthèse d'ouverture (RSO) spatial fournit une source de données brutes pouvant servir à évaluer sa vulnérabilité au brouillage et à explorer les mesures de protection qui lui permettraient de fonctionner dans un environnement électromagnétique contesté. Les principales caractéristiques d'une telle simulation sont la souplesse de l'approche utilisée dans le domaine temporel, la géométrie sphéroïdale de la Terre en rotation, le calcul de l'amplitude absolue des signaux et la capacité de générer des scènes radar de grandes dimensions. Ces caractéristiques facilitent l'intégration des signaux de brouillage aux propriétés quantitatives spécifiques (p. ex., la puissance d'émission) dans l'environnement de simulation des géométries à l'étude et permettent d'évaluer correctement les effets du brouillage sur le plan quantitatif. Durant la simulation, les géométries sont définies à partir des métadonnées fournies par un ensemble de RSO spatiaux réels. Les données d'image réelles permettent de définir le champ de réflectivité de la surface de la Terre qui est mesuré par le RSO spatial simulé. Les données sur la surface de la Terre, le bruit radar et les cibles d'essai sont alors générées, combinées de façon cohérente et converties en signaux numériques pouvant être traités au moyen d'algorithmes de formation d'images RSO. Une option permettant de décompresser les signaux à compression de portée bruts réels mesurés en mode MODEX de RADARSAT-2, de les mettre à l'échelle et de les combiner aux signaux des cibles d'essai est également en cours de conception. En effet, les données réelles doivent être mises à l'échelle pour que l'amplitude absolue mesurée dans le monde réel reflète celle qui serait mesurée dans l'environnement de simulation. Cette option permet donc d'évaluer la validité des signaux simulés en les comparant avec des données réelles. Pour évaluer la précision de la simulation, on compare les propriétés des signaux et des images simulés avec les attentes théoriques et les propriétés des signaux et des images réels. La concordance observée entre tous les aspects comparés confirme que les signaux simulés se rapprochent effectivement des signaux RSO bruts réellement reçus et que la simulation peut être utilisée aux fins prévues.

Importance pour la défense et la sécurité

Les systèmes canadiens de RSO spatiaux RADARSAT et RADARSAT-2 fournissent aux ministères fédéraux différents produits qui appuient la surveillance maritime, la surveillance des glaces, la gestion des catastrophes, la surveillance environnementale, la gestion des ressources et la cartographie. À l'heure actuelle, il est impossible de réaliser de manière fiable et abordable certaines de ces activités par d'autres moyens. En outre, le gouvernement du Canada travaille en ce moment à préparer la mission de la Constellation RADARSAT, qui regroupera plusieurs satellites dotés de RSO. Les capacités fournies par les RSO spatiaux, comme la détection, la classification et la surveillance des navires, sont essentielles à la mission de connaissance du domaine maritime du ministère de la Défense nationale. Les RSO spatiaux représentent donc un outil national stratégique dont le Canada a besoin aujourd'hui et dont il aura encore besoin demain. Mais comme les capacités des RSO spatiaux peuvent être altérées par le brouillage, il faudra améliorer leur résistance à de telles interférences intentionnelles. La recherche dans ce domaine fait d'ailleurs l'objet de publications non classifiées. Cette recherche fournit les outils nécessaires pour examiner les différentes méthodes d'atténuation des effets du brouillage sur les RSO spatiaux.

Table of contents

Abstract	i
Significance to defence and security	i
Résumé	ii
Importance pour la défense et la sécurité	ii
Table of contents	iii
List of figures	v
List of tables.	viii
Acknowledgements	ix
1 Introduction	1
2 Overview of general approach.	3
3 Earth surface	8
3.1 Coordinate systems and transformations	8
3.2 Signal sample calculation using a discrete reflectivity field	15
3.2.1 Point scatterer radar cross section	21
3.2.2 Resolution volume	22
3.3 Signal samples derived from real data.	25
4 Test targets.	32
4.1 Signal sample calculation	32
4.2 Statistical fluctuations	33
4.2.1 Swerling 1 model	35
4.2.2 Swerling 2 model	36
4.2.3 Swerling 3 model	38
4.2.4 Swerling 4 model	38
5 Receiver system noise.	39
6 Analogue to digital conversion	41
7 Evaluation of simulated signals	43
7.1 Test target	43
7.2 Earth surface	52
7.2.1 Case 1: MODEX 1 mode.	52
7.2.1.1 Comparison of unprocessed data	53
7.2.1.2 Comparison of range-compressed data	54
7.2.1.3 Comparison of range- and azimuth-compressed data	56
7.2.1.4 Image comparison.	57
7.2.1.5 Comparison of image statistics	63
7.2.2 Case 2: W2 mode	71
7.2.2.1 Unprocessed data	73

7.2.2.2	Image Comparison	73
7.2.2.3	Comparison of image statistics	77
8	Summary and conclusions	82
	References	83
Annex A	Earth intersection points	85
A.1	Earth intersection point calculation for known pointing direction.	86
A.2	Direction vector transformation	88
A.3	Algorithm initiation	89
A.4	Iteration.	94
Annex B	Implementation of Range-Doppler Algorithm	98
B.1	Range compression	98
B.2	Range cell migration correction	99
B.3	Azimuth compression.	102
B.4	Geolocation	105
	List of symbols/abbreviations/acronyms/initialisms	107

List of figures

Figure 1:	Overview of the computational approach used to generate the simulated SAR signals.	4
Figure 2:	Two different views of the SAR imaging geometry for an example case.	5
Figure 3:	Relationship between the coordinate systems corresponding to transmit (blue) and receive (red) phase centres.	8
Figure 4:	Radar-centred Cartesian coordinate systems. The two systems differ according to the yaw, roll, and pitch applied to the satellite.. . . .	9
Figure 5:	Earth-centred fixed coordinate system (red) and an earth-centred coordinate system aligned with the longitude of the satellite (green).	12
Figure 6:	Earth-centred coordinate system aligned with the longitude of the satellite (red) and earth-centred coordinate system aligned with the satellite longitude and latitude (green)..	13
Figure 7:	Earth-centred coordinate system aligned with the longitude and latitude of the satellite (red) and earth-centred coordinate system aligned with the x'' - y'' - z'' coordinate system (green)..	14
Figure 8:	Left: Image of in-phase signal samples corresponding to a single test target. A non-linear grey scale has been applied to the data to enhance contrast. Right: A blow-up of the portion of the left image in the region of peak magnitude (cyan box). A linear grey scale is used.	46
Figure 9:	Signal properties as a function of fast-time for pulse number 13884.	47
Figure 10:	Signal properties as a function of slow-time for range bin number 4520.. . . .	48
Figure 11:	SAR Image of the simulated test target data. A non-linear colour scale is used to enhance contrast. The cyan box shows the region containing the peak image pixel value and denotes the region displayed in Figure 12.. . . .	49
Figure 12:	Zoomed in view of SAR image in the region of the test target signature (cyan box of Figure 11).	50
Figure 13:	Image pixel (slant-range) and image line (cross-range) cuts through the test target image data. The upper two plots show all of the data. The lower two plots are zoomed regions corresponding to the cyan boxes in the upper plots.	51
Figure 14:	Zoomed in surface view of the test target image signature.	52
Figure 15:	Unprocessed in-phase data for pulse number 13884.. . . .	53
Figure 16:	Unprocessed received signal power for pulse number 13884.	54
Figure 17:	Range-compressed signal power for pulse number 13884.	55
Figure 18:	Range- and azimuth-compressed signal power for line number 12181.	56
Figure 19:	Range- and azimuth-compressed signal power for pixel number 4520.	57

Figure 20:	Range- and azimuth-compressed signal power in the region of the test target signature. The vertical cyan lines mark pixel number 4520 and line number 12181.	58
Figure 21:	SAR images corresponding to the real, scaled signals (left) and the simulated signals (right). Black regions correspond to no data.	59
Figure 22:	SAR images of the mountainous region north of Vancouver (cyan box in Figure 21) corresponding to the real, scaled signals (upper) and the simulated signals (lower).	60
Figure 23:	SAR images of Crown mountain (cyan box in Figure 22) corresponding to the real, scaled signals (upper) and the simulated signals (lower).	61
Figure 24:	SAR images of the Vancouver airport (yellow box in Figure 21) corresponding to the real, scaled signals (left) and the simulated signals (right).	62
Figure 25:	Simulated image power associated with the parking lot region in the yellow box of Figure 24.	63
Figure 26:	SAR images of a forest area (green box in Figure 21) corresponding to the real, scaled signals (left) and the simulated signals (right).	64
Figure 27:	Image amplitude probability density functions for the forest area shown in Figure 26.	65
Figure 28:	Normalized spatial autocorrelation functions corresponding to the real, scaled, image data (upper) and the simulated image data (lower) for the forest area (Figure 26).	66
Figure 29:	Normalized spatial autocorrelation functions at zero cross-range lag (left) and zero slant-range lag (right) for the forest area (Figure 26).	67
Figure 30:	SAR images of a uniform sea patch (orange box in Figure 21) corresponding to the real, scaled signals (upper) and the simulated signals (lower).	68
Figure 31:	Image amplitude probability density functions for the uniform sea patch shown in Figure 30.	69
Figure 32:	Normalized spatial autocorrelation functions corresponding to the real, scaled image data (upper) and the simulated image data (lower) for the uniform sea patch (Figure 30).	70
Figure 33:	Normalized spatial autocorrelation functions at zero cross-range lag (left) and zero slant-range lag (right) for the uniform sea patch (Figure 30).	71
Figure 34:	Transmit and receive azimuth and elevation antenna gain patterns used for the W2 mode with HH polarization.	73
Figure 35:	Simulated unprocessed in-phase and quadrature data for pulse number 5757.	74
Figure 36:	SAR images corresponding to the real, scaled $(\beta^o)^{1/2}$ data (left) and the simulated signals (right).	75
Figure 37:	SAR images of the mountainous region north of Vancouver (cyan box in Figure 37) corresponding to the real, scaled $(\beta^o)^{1/2}$ data (left) and the simulated signals (right).	76
Figure 38:	SAR images of the region extending from the Vancouver airport to Burrard Inlet (yellow box in Figure 37) corresponding to the real, scaled $(\beta^o)^{1/2}$ data (left) and the simulated signals (right).	77

Figure 39:	SAR images of a uniform sea patch (orange box in Figure 36) corresponding to the real, scaled $(\beta^o)^{1/2}$ data (upper) and the simulated signals (lower)..	78
Figure 40:	Image amplitude probability density functions for the uniform sea patch shown in Figure 39..	79
Figure 41:	Normalized spatial autocorrelation functions corresponding to the real, scaled $(\beta^o)^{1/2}$ data (upper) and the simulated image data (lower) for the uniform sea patch (Figure 39).	80
Figure 42:	Normalized spatial autocorrelation functions at zero cross-range lag (left) and zero slant-range lag (right) for the uniform sea patch (Figure 39).	81
Figure A.1:	Earth intersection geometry. The magenta line shows the satellite orbit. The yellow axes represent a Cartesian coordinate system centred at the radar antenna. The radar beam is shown in translucent blue. The green line extending upward from the surface of the earth represents the circle dictated by the range and azimuth constraints. . . .	86
Figure A.2:	Vectors associated with the solution to the earth intersection point problem.	87

List of tables

Table 1:	Test target parameters..	43
Table 2:	Control parameters for test target and MODEX 1 mode simulations.	43
Table 3:	SAR parameters for test target and MODEX 1 mode simulations.	44
Table 4:	Image formation processing parameters for test target and MODEX 1 mode simulations.	45
Table 5:	Control parameters for the W2 mode simulation	71
Table 6:	SAR parameters for the W2 mode simulation.	72
Table 7:	Image formation parameters for the W2 mode simulation.	72

Acknowledgements

The Range-Doppler image formation algorithm implemented in this work is based upon example code provided by Shen Chiu of the DRDC – Ottawa Research Centre Radar Sensing and Exploitation (RSE) Section. The pulse decompression processing is based upon example code developed by Ishuwa Sikaneta, formerly of the RSE Section. RADARSAT-2 MODEX data were provided by the RSE Space-Based Radar Group. Shen Chiu (RSE), Chuck Livingstone (RSE), Christoph Gierull (RSE), Marina Dragosevic (RSE Contractor), and Pete Beaulne (DRDC – Ottawa Research Centre Radar Electronic Warfare Section) provided valuable consultations on the MODEX data and its processing. Antenna gain pattern data for the RADARSAT-2 W2 mode were provided by MacDonald, Dettwiler, and Associates Ltd.

Original RADARSAT-2 Data and Products ©MacDonald, Dettwiler and Associates Ltd., 2008, 2010 – All Rights Reserved.

This page intentionally left blank.

1 Introduction

The simulation of the raw signals produced by a Synthetic Aperture Radar (SAR) receiver has been investigated by many researchers for many different applications. For example, simulations of raw SAR signals have been created to investigate the susceptibility of SAR to interference [1] [2], to aid the design of new SAR systems and operating modes [3] [4] [5], to aid the development of image formation algorithms [4] [6], to aid the development of pattern recognition and feature extraction techniques [6], to investigate noise and clutter rejection [6], to investigate estimation of moving target parameters [7] [8], to investigate ocean features and develop ocean-feature retrieval algorithms [9], to investigate the effects of oscillations of the mechanical structure of the SAR platform [10], etc.. Several different approaches for simulating raw SAR signals have been developed, with each of these methods having different strengths and weaknesses. New methods for simulating raw SAR signals continue to be presented in the literature. Both [7] and [9] are recent publications that provide good summaries of the literature in terms of the different approaches that have been implemented.

This report describes a simulation of raw SAR signals that is intended to be used for investigating the vulnerability of space-based SAR to jamming and for investigating potential protection measures that could enable space-based SAR to operate in a contested electromagnetic environment. A key requirement of the simulation is to produce signals with absolute scaling so that jamming effects can be studied quantitatively as a function of the parameters characterizing the jammer transmission. A flexible approach is also important to simplify the introduction of various types of jamming and the implementation of different protection measures. Consequently, a time-domain approach was chosen. As is widely pointed out in the literature, the disadvantage of a time-domain approach is the long times required to complete the necessary calculations, especially when attempting to simulate large SAR scenes. This drawback is mitigated somewhat with a combination of computing power and parallel processing, with the expectation that computing power will increase in the future. Patient requirements for simulation output also reduce the negative impact of the long calculation times. That is, the application of interest does not require a large amount of data to be simulated. Many different jamming techniques and protection measures can be investigated using a single simulated scene. If the demand for simulation output is more than expected, then further measures could be explored to speed up the calculations (e.g., [5]).

Other key features of the simulation include rotating spheroidal Earth geometry, multi-aperture configurations, simulated test targets, receiver noise, analogue-to-digital conversion, and range-Doppler image formation processing. The simulation uses a “pseudo-inversion” approach to generate the signals received from the surface of the earth. That is, an actual SAR image is used to define a surface reflectivity field that is “measured” by the simulated SAR. Use of an actual SAR image as the surface reflectivity field will incorporate any effects present in the image, such as shadowing and layover, into the simulated signals. Statistical fluctuations in the signals received from the surface are generated through a combination of the fluctuations inherent in the reflectivity field and summation of many simulated backscattered waves (typically on the order of 10^6). Signal fluctuations for the test targets are simulated using Swerling models [11]. The simulation also has the capability to decompress and appropriately scale real RADARSAT-2 MODEX range-compressed data [12] so that it can be combined with simulated test target and jammer signals. This mode is used to evaluate the validity of the simulation.

This simulation is currently limited to stripmap mode. In addition, no explicit consideration is given to signal polarization and elevated terrain at this time. If necessary, the simulation could be extended to include

such features using existing techniques described in the literature (e.g., [3] [4] [6] [8] [10]). Test targets are modelled as stationary point scatterers, but the use of the time-domain approach would allow target motion and aspect-dependent radar cross section to be added. The need to add any further features, however, will be dictated by the results of jamming studies.

This report provides a detailed description of the space-based SAR simulation. Due to classification this does not include a description of the jammer models and calculations. These will be documented in a separate publication. The simulation is evaluated by simulating data corresponding to a RADARSAT-2 MODEX collection and comparing it with the real data in terms of signal and image properties. Simulated data for an operational RADARSAT-2 mode is also generated and compared with the real data in terms of image properties.

2 Overview of general approach

The logic flow, modes, and options of the simulation are depicted in Figure 1, with execution beginning in the top left corner and proceeding to the bottom right corner. Program control and the majority of the calculations are performed with a set of procedures written in Interactive Data Language (IDL).

The simulation begins by reading a selected RADARSAT-2 data file and using its contents to define all of the parameters related to the simulated SAR. This ensures that realistic parameters are chosen for the simulation. In future, the simulation could be adapted to enable simulation of other SAR systems, such as RADARSAT Constellation Mission, when data become available. The RADARSAT-2 image data are used at a later point in the calculations indicated by a connection to the green diamond symbol.

After parameter definition, IDL program control interfaces with the Systems ToolKit (STK) software to replicate the actual RADARSAT-2 imaging geometry within the simulation environment. Figure 2 shows a view of the simulated SAR imaging geometry for an example case. The upper portion of the figure shows the geometry from a far vantage point and the lower portion of the figure shows the geometry from a vantage point that is close to the satellite. The short cyan line shows the RADARSAT-2 satellite orbit as determined by state vector data included in the chosen RADARSAT-2 data set. This line corresponds to the time frame over which the SAR data is collected. The green line shows an extrapolation of this orbit. White arrows depict the measurement coordinate system of the SAR sensor. The yellow translucent shading depicts the transmitted radar beam. The red quadrilateral shown on the surface of the earth depicts the imaging area as defined by the image tie point data included in the chosen RADARSAT-2 data set [13]. The orange dot shows the location of a simulated test target. STK is also used to provide geometrical data back to IDL, such as the satellite position and velocity, and the angular momentum of the satellite orbit. These calculations consider the rotation of the earth. The STK data are also used at several later points in the calculations, which are indicated by connections to the dark blue circle symbol.

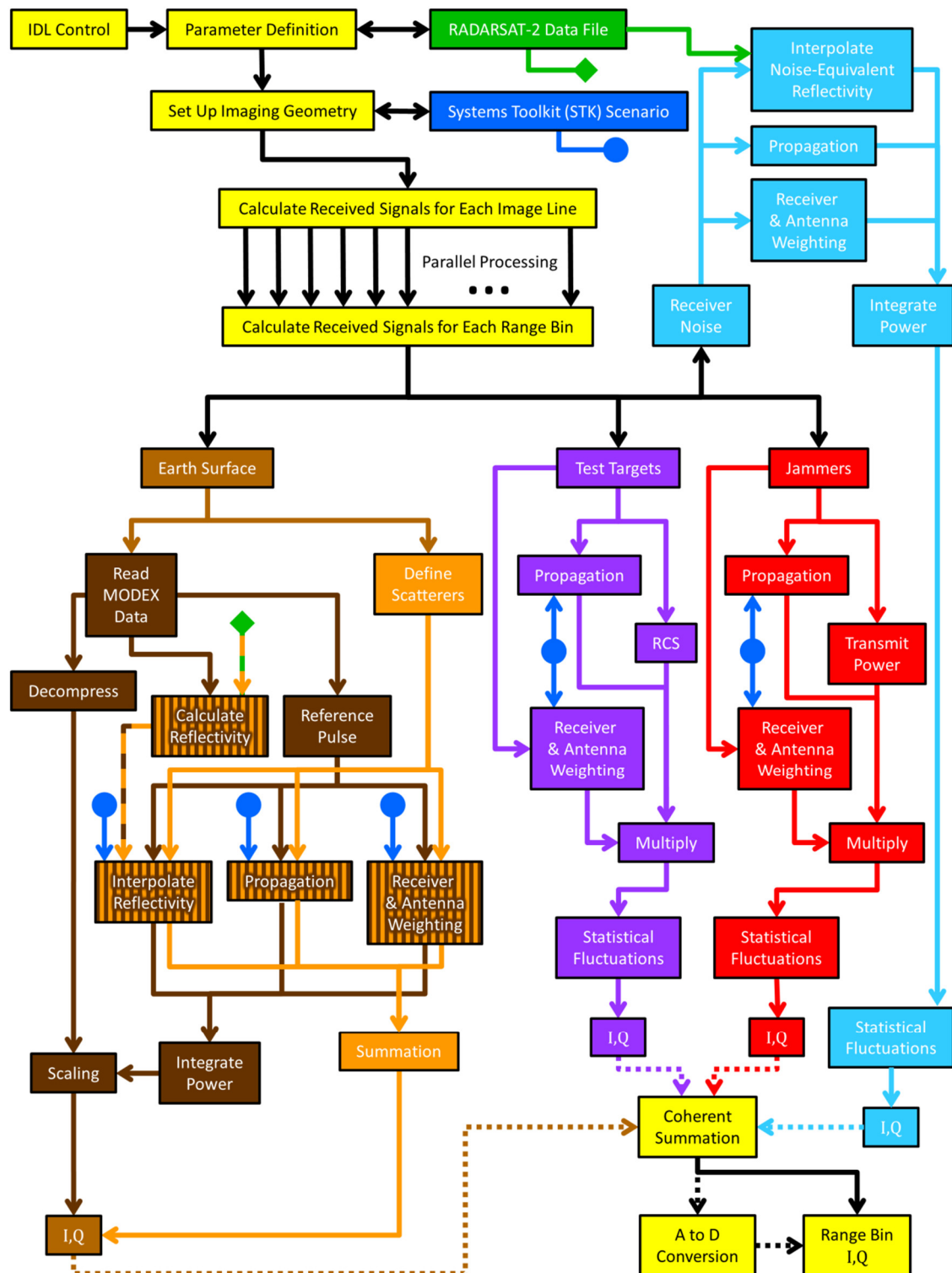


Figure 1: Overview of the computational approach used to generate the simulated SAR signals.

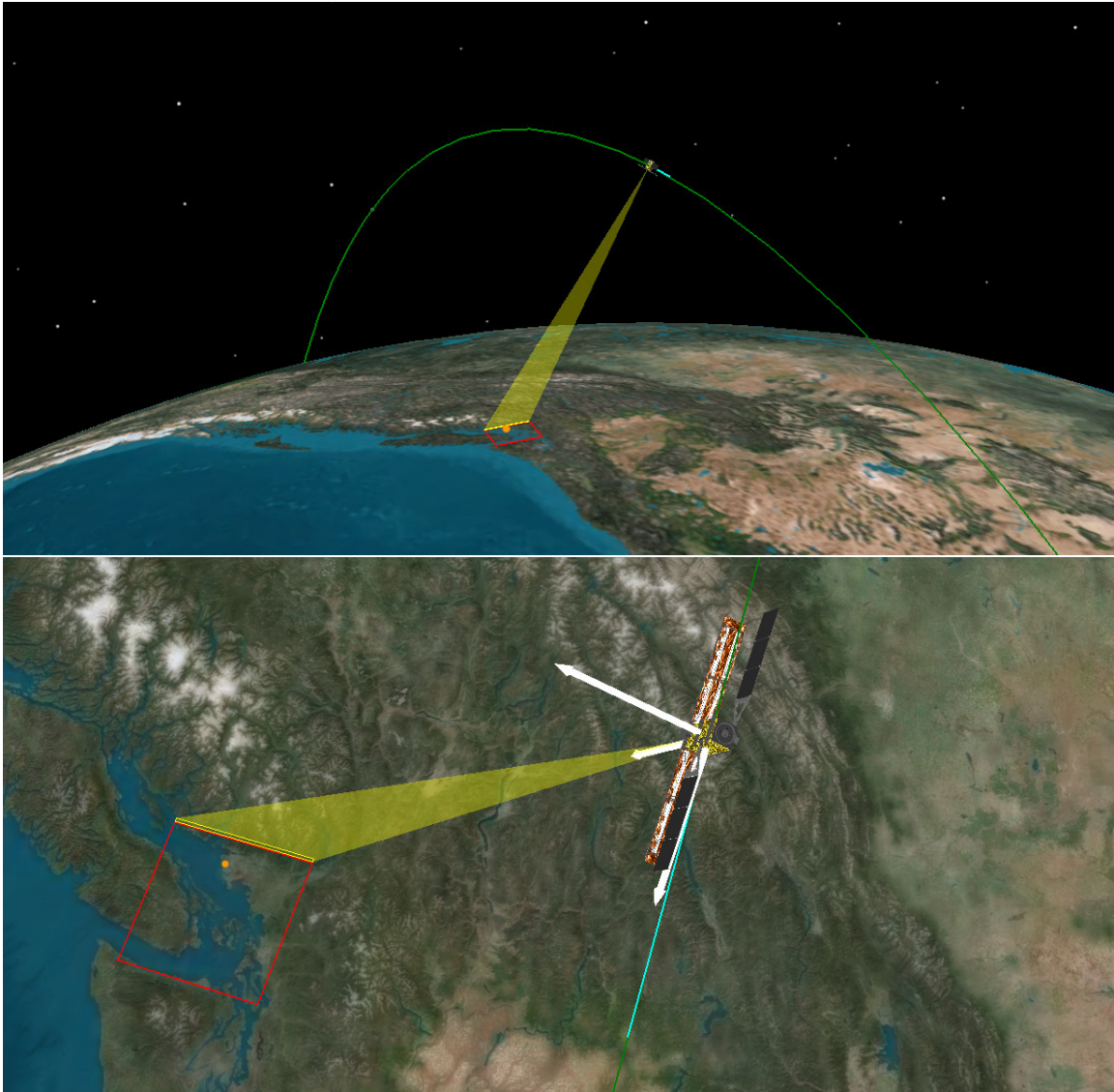


Figure 2: Two different views of the SAR imaging geometry for an example case.

The simulation steps in time, in increments equal to the pulse repetition interval, to calculate the received signals corresponding to each transmitted pulse. There are typically thousands of range bins corresponding to each pulse. Parallel processing is used to simultaneously calculate the received signals for multiple range bins. The calculations consider the contribution of four different signal sources to the final received signal. These are signals received from the surface of the earth, from test targets, from jammers, and from receiver system noise.

Two different modes are available for generating signals received from the surface of the earth. The first mode reads, decompresses, and scales real range-compressed data measured by RADARSAT-2 in the experimental MODEX mode [12]. This mode is depicted with the brown boxes and arrows and is used for evaluating the output of the simulation. The decompressed data must be appropriately scaled so that its magnitude is adjusted to the level that would be “measured” by the simulated SAR in the simulated

environment. The scaling constant is derived from the results of simulating the measurement of the signals received for a set of range bins corresponding to a reference pulse that is in the middle of the pulses transmitted by the SAR. That is, an observed reflectivity field is calculated by processing the raw MODEX data using the range-Doppler algorithm [14], scaling the resulting image according to the lookup table data associated with the chosen RADARSAT-2 data file [15], and then mapping the resulting observed reflectivity onto the surface of the earth. This reflectivity field is interpolated, weighted according to the receiver and antenna properties, propagated (only free-space propagation is considered), and integrated to provide a mean power level for each range bin corresponding to the reference pulse. The scaling constant is then determined as the ratio of the average magnitudes of the simulated and real data corresponding to the reference pulse.

The MODEX mode uses an antenna beam pattern that is not representative of the standard operational modes used by RADARSAT-2. For the standard operating modes, the side lobes of the elevation angle beam patterns are greatly reduced. Therefore, the real MODEX data does not help to satisfy the requirement to generate SAR signals for use in jamming studies. The second mode for simulating signals received from the surface of the earth is depicted with the orange boxes and arrows. This mode can consider any antenna beam pattern. In this mode, the reflectivity of the surface of the earth is represented with a large number of discrete scatterers. The reflectivity corresponding to each scatterer is interpolated from a reflectivity field that is calculated from the observed reflectivity derived from the image data associated with the chosen RADARSAT-2 data set [15]. The signal contribution corresponding to each scatterer has a phase that is determined by its location plus a random positional offset of magnitude less than or equal to a wavelength. The random offset is employed to ensure that the simulated signals exhibit fully developed speckle [16]. The contributions from each scatterer are weighted and propagated similarly to the Earth surface signal simulation mode summarized in the previous paragraph. The individual signals corresponding to all scatterers within the radar resolution volume are summed to create the signal samples for a given range bin. The statistics of the final signals are dictated by the speckle inherent in the input reflectivity field and the summation of the many signals corresponding to the scatterers within a resolution volume.

Test target signals are generated similarly to the Earth surface signals corresponding to the discrete scatterer mode. The main difference is that the test target signals are given statistics corresponding to one of the four Swerling models [11]. Any number of test targets can be simulated. Each target is defined at a specific longitude and latitude and with a specific Radar Cross Section (RCS). The RCS is a constant value for each test target. Aspect dependent RCS values could be incorporated into the simulation at a later time if necessary. The test target calculations are depicted in Figure 1 with the purple boxes and arrows.

RADARSAT-2 data files include reference noise level data in terms of a noise-equivalent observed reflectivity [13]. Similarly to the power calculations required for scaling the decompressed MODEX data, noise power levels are calculated by simulating the powers that would be received from the noise-equivalent observed reflectivity field. This portion of the simulation is depicted with the light blue boxes and arrows in Figure 1. The integrated power is used to generate noise signal samples having amplitudes that conform to a Rayleigh distributed probability density function and the correct signal magnitude.

Optional calculations are depicted in Figure 1 with dashed lines. The signal samples from each of the different sources can be coherently summed to form the final signal samples, i.e.,

$$I = I_S + I_T + I_N + I_J \quad (1)$$

$$Q = Q_S + Q_T + Q_N + Q_J$$

where the subscripts S , T , N , and J refer to the Earth's surface, test targets, radar system noise, and jammers, respectively. For simplicity, these subscripts will be omitted in the following sections (3, 4, 5) that describe the calculation of the first three terms on the right-hand side of Equation (1). Jamming calculations are described in a separate publication. The dashed lines are meant to show that any combination of the four source signals can be chosen so that the effects of the different sources can be examined. For example, SAR images processed with and without the inclusion of jamming signals can be generated to study the effects of the applied jamming technique. Quantization of the signals resulting from analogue-to-digital conversion is also modelled and can be optionally included. The options to not include analogue-to-digital conversion and receiver noise are made available since their effects may be inherently included in the reflectivity field derived from actual SAR image data. If an artificial reflectivity field was defined, for example, from an optical image, then the receiver noise and analogue-to-digital conversion would need to be included.

3 Earth surface

3.1 Coordinate systems and transformations

Several coordinate systems and transformations are required for the calculation of the in-phase and quadrature signal samples. The main purpose of the transformations is to determine the coordinates of points, at known longitudes and latitudes on the surface of the earth, in the coordinate systems associated with the SAR antenna, and vice versa. Coordinate systems having origins located on the SAR antenna are denoted with lowercase letters, whereas coordinate systems with origins at the centre of the earth are denoted with uppercase letters.

The current purpose of considering a multi-aperture configuration is to enable the simulation of signal samples that can be compared with the real data that are available from the RADARSAT-2 MODEX modes. In future, the ability to generate simulated signal samples for multi-aperture configurations may be useful for evaluating electronic protection measures. The real data chosen for comparison in this document was collected in the MODEX 1 mode. In this mode, the radar transmits each pulse using the full aperture and receives simultaneously on two half apertures that are formed by dividing the antenna in two in the along-track dimension.

Coordinate systems are defined in Figure 3 with origins located at both the transmit (blue) and receive (red) phase centres. The vector \vec{v}_p (black arrow) represents the velocity vector of the satellite. The Cartesian coordinate system centred at the receive phase centre (x - y - z) is defined relative to the transmit phase centre coordinate system (x_T - y_T - z_T) using the translation

$$\begin{aligned}x &= x_T \\y &= y_T - \Delta y \\z &= z_T\end{aligned}\tag{2}$$

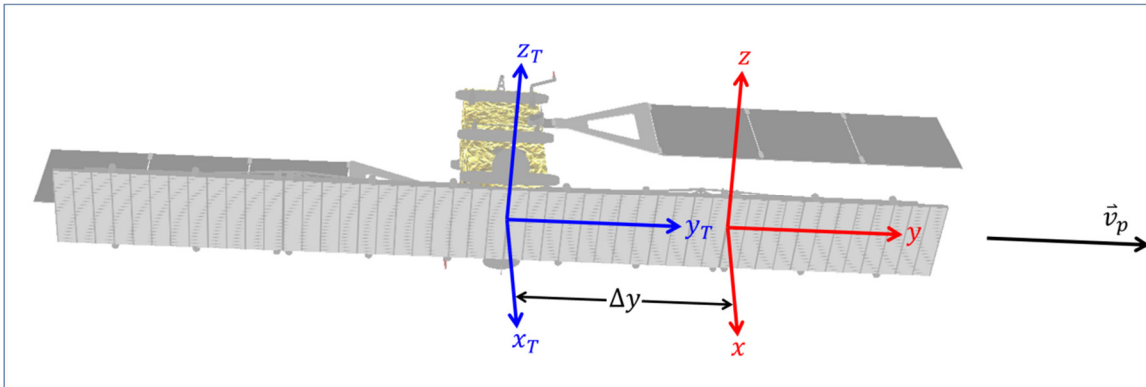


Figure 3: Relationship between the coordinate systems corresponding to transmit (blue) and receive (red) phase centres.

where Δy is the distance along the y -axes between the two coordinate systems. The y_T and y axes are parallel and each point in the same direction as the along-track motion of the satellite. The y_T , z_T , y , and z axes are all contained within the plane of the antenna. The x_T and x axes are normal to the antenna such that they form a right-handed coordinate system with the y_T and z_T , and the y and z axes, respectively. In the configuration of interest (MODEX 1) Δy is equal to one quarter of the antenna length. For the case of RADARSAT-2, Δy is 3.75 m when the receive phase centre corresponds to the fore half of the antenna and -3.75 m when the receive phase centre corresponds to the aft half of the antenna. Figure 3 shows the case where the receive antenna is the fore half of the full antenna ($\Delta y = 3.75$ m). When $\Delta y = 0$ all of the mathematics presented in this document revert to the monostatic case corresponding to the standard operating modes of RADARSAT-2.

The coordinate systems with origins located at the transmit phase centre will be referred to as radar-centred coordinate systems. The transmit phase centre is assumed to be at the centre of the satellite. The radar-centred coordinate system shown in Figure 4 with the red axes labelled with lowercase x_T , y_T , and z_T is the same as the blue system depicted in Figure 3. The green axes, labelled x' , y' , and z' , show a radar-centred coordinate system such that the yaw, roll, and pitch of the satellite have been removed, resulting in the x' -axis pointing in the nadir direction (toward the centre of the earth), the y' -axis pointing in the direction of satellite motion, and the z' -axis pointing in a direction that completes a right-handed coordinate set (perpendicular to the orbital plane).

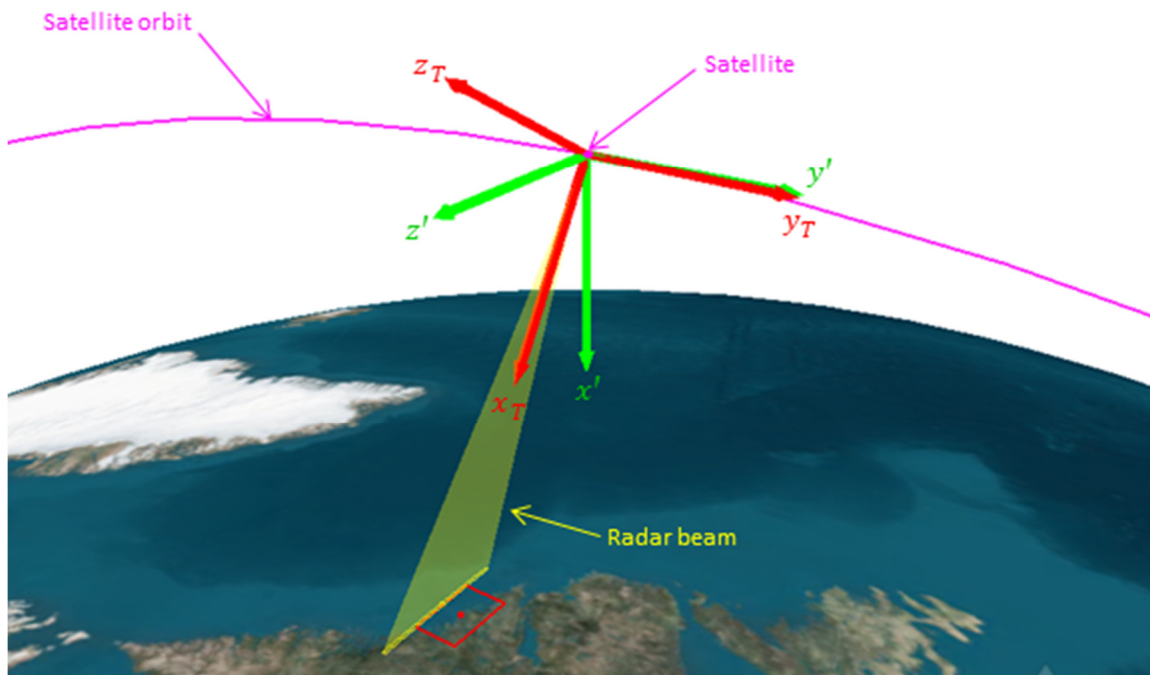


Figure 4: Radar-centred Cartesian coordinate systems. The two systems differ according to the yaw, roll, and pitch applied to the satellite.

An additional radar-centred coordinate system is also defined such that

$$\begin{aligned}x'' &= y' \\y'' &= z' \\z'' &= x'\end{aligned}\tag{3}$$

This definition has the z'' -axis pointing in the nadir direction, the x'' -axis pointing in the direction of satellite motion, and the y'' -axis pointing in a direction that completes a right-handed coordinate set (perpendicular to the orbital plane).

Yaw is defined as a rotation about the nadir axis (x' -axis in this case) such that a positive yaw moves the y' and z' axes clockwise when viewing the satellite from above. The transformation matrix for a yaw rotation by an angle α can be expressed as

$$\mathbf{R}_{x'}(\alpha) = \begin{bmatrix} \cos \alpha & \sin \alpha & 0 \\ -\sin \alpha & \cos \alpha & 0 \\ 0 & 0 & 1 \end{bmatrix}\tag{4}$$

Roll is defined as a rotation about the axis pointing in the direction of motion (y' -axis in this case) such that a positive roll moves the x' and z' axes counter-clockwise when viewing the satellite from the direction that it is travelling to. A roll rotation by an angle γ can be expressed as

$$\mathbf{R}_{y'}(\gamma) = \begin{bmatrix} 1 & 0 & 0 \\ 0 & \cos \gamma & \sin \gamma \\ 0 & -\sin \gamma & \cos \gamma \end{bmatrix}\tag{5}$$

Pitch is defined as a rotation about the axis that is perpendicular to the orbital plane (z' -axis in this case) such that a positive pitch moves the x' and y' axes counter-clockwise when viewing the satellite from the positive z' direction. A pitch rotation by an angle β can be expressed as

$$\mathbf{R}_{z'}(\beta) = \begin{bmatrix} \cos \beta & 0 & -\sin \beta \\ 0 & 1 & 0 \\ \sin \beta & 0 & \cos \beta \end{bmatrix}\tag{6}$$

The spacecraft of main interest to this document is RADARSAT-2. Consequently, the transformations defined here are designed to match those that would be applied to RADARSAT-2. The metadata associated with a RADARSAT-2 image file reports the satellite attitude in terms of yaw, roll, and pitch values that are applied extrinsically in the x'' - y'' - z'' coordinate system in the order yaw, roll, and pitch [13]. Therefore, if the rotations are to be implemented extrinsically in the x' - y' - z' system they must be applied in the order

roll, pitch, and yaw. Intrinsic calculation of the attitude would then be performed in the reverse order. That is, the attitude matrix that transforms a point in the $x'-y'-z'$ coordinate system to a point in the $x_T-y_T-z_T$ coordinate system can be calculated as

$$\begin{aligned} \mathbf{A}(\alpha, \beta, \gamma) &= \mathbf{R}_{x'}(\alpha)\mathbf{R}_{z'}(\beta)\mathbf{R}_{y'}(\gamma) \\ &= \begin{bmatrix} \cos \alpha & \sin \alpha & 0 \\ -\sin \alpha & \cos \alpha & 0 \\ 0 & 0 & 1 \end{bmatrix} \begin{bmatrix} \cos \beta & 0 & -\sin \beta \\ 0 & 1 & 0 \\ \sin \beta & 0 & \cos \beta \end{bmatrix} \begin{bmatrix} 1 & 0 & 0 \\ 0 & \cos \gamma & \sin \gamma \\ 0 & -\sin \gamma & \cos \gamma \end{bmatrix} \end{aligned} \quad (7)$$

$$\mathbf{A} = \begin{bmatrix} \cos \alpha \cos \beta & \sin \alpha \cos \gamma + \cos \alpha \sin \beta \sin \gamma & \sin \alpha \sin \gamma - \cos \alpha \sin \beta \cos \gamma \\ -\sin \alpha \cos \beta & \cos \alpha \cos \gamma - \sin \alpha \sin \beta \sin \gamma & \cos \alpha \sin \gamma + \sin \alpha \sin \beta \cos \gamma \\ \sin \beta & -\cos \beta \sin \gamma & \cos \beta \cos \gamma \end{bmatrix} \quad (8)$$

and the inverse transformation from the $x_T-y_T-z_T$ coordinate system to the $x'-y'-z'$ coordinate system can be calculated as

$$\begin{aligned} \mathbf{A}^{-1}(\gamma, \beta, \alpha) &= \mathbf{R}_y(\gamma)\mathbf{R}_z(\beta)\mathbf{R}_x(\alpha) \\ &= \begin{bmatrix} 1 & 0 & 0 \\ 0 & \cos \gamma & -\sin \gamma \\ 0 & \sin \gamma & \cos \gamma \end{bmatrix} \begin{bmatrix} \cos \beta & 0 & \sin \beta \\ 0 & 1 & 0 \\ -\sin \beta & 0 & \cos \beta \end{bmatrix} \begin{bmatrix} \cos \alpha & -\sin \alpha & 0 \\ \sin \alpha & \cos \alpha & 0 \\ 0 & 0 & 1 \end{bmatrix} \end{aligned} \quad (9)$$

$$\mathbf{A}^{-1} = \begin{bmatrix} \cos \alpha \cos \beta & -\sin \alpha \cos \beta & \sin \beta \\ \cos \alpha \sin \beta \sin \gamma + \sin \alpha \cos \gamma & -\sin \alpha \sin \beta \sin \gamma + \cos \alpha \cos \gamma & -\cos \beta \sin \gamma \\ -\cos \alpha \sin \beta \cos \gamma + \sin \alpha \sin \gamma & \sin \alpha \sin \beta \cos \gamma + \cos \alpha \sin \gamma & \cos \beta \cos \gamma \end{bmatrix} \quad (10)$$

An Earth-centred fixed coordinate system is defined to have its origin at the centre of the earth, its Z-axis aligned with the direction to the north pole, its X-axis pointing within the equatorial plane of the earth and aligned with 0° longitude, and its Y-axis pointing within the equatorial plane of the earth and aligned with 90° longitude. Three transformations are also defined to transform a point in the earth-centred fixed coordinate system ($X-Y-Z$) to an Earth-centred coordinate system ($X'''-Y'''-Z'''$) that is aligned with the $x''-y''-z''$ coordinate system. Figure 5 shows the earth-centred fixed coordinate system (red) and another earth-centred coordinate system (green) that has its X' -axis aligned with the longitude of the satellite and its Z' -axis coincident with the Z-axis. The longitude of the satellite, Φ_s , is provided by STK as a function of slow-time. The rotation matrix that describes the transformation of a point in the $X-Y-Z$ system to the $X'-Y'-Z'$ system can be written as

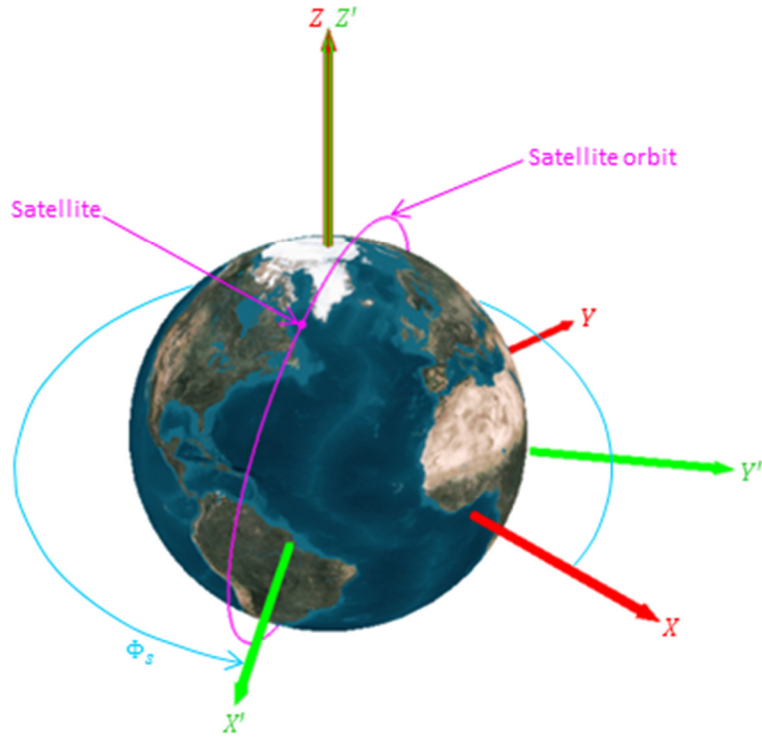


Figure 5: Earth-centred fixed coordinate system (red) and an earth-centred coordinate system aligned with the longitude of the satellite (green).

$$\mathbf{E}_Z = \begin{bmatrix} \cos \Phi_s & \sin \Phi_s & 0 \\ -\sin \Phi_s & \cos \Phi_s & 0 \\ 0 & 0 & 1 \end{bmatrix} \quad (11)$$

and the inverse rotation matrix can be written as

$$\mathbf{E}_{Z'}^{-1} = \begin{bmatrix} \cos \Phi_s & -\sin \Phi_s & 0 \\ \sin \Phi_s & \cos \Phi_s & 0 \\ 0 & 0 & 1 \end{bmatrix} \quad (12)$$

Figure 6 shows the $X'-Y'-Z'$ coordinate system (red) and another earth-centred coordinate system (green) that has its X'' -axis aligned with the longitude of the satellite, its Z'' -axis aligned with the latitude of the satellite, and its Y'' -axis coincident with the Y' -axis. The rotation matrix that describes the transformation of a point in the $X'-Y'-Z'$ system to the $X''-Y''-Z''$ system can be written as

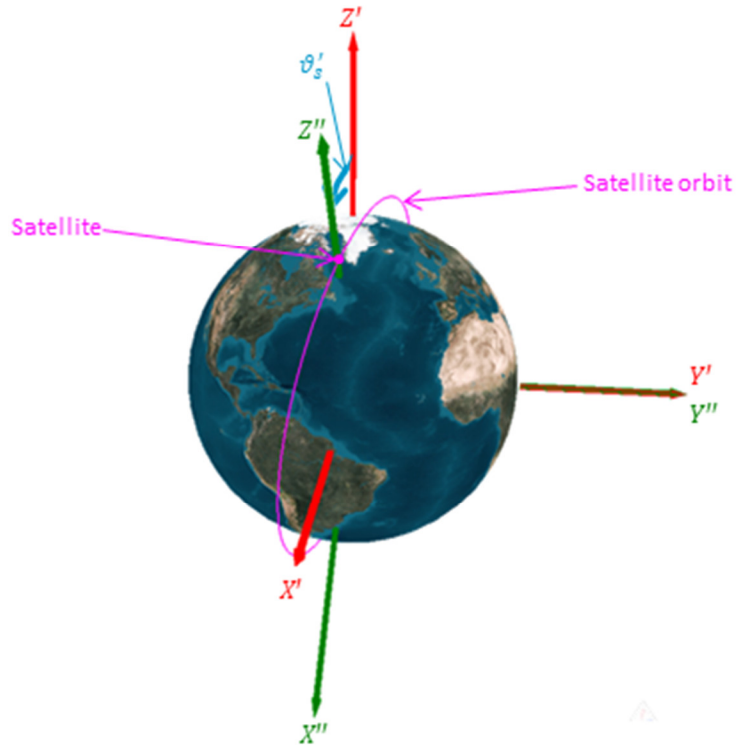


Figure 6: Earth-centred coordinate system aligned with the longitude of the satellite (red) and earth-centred coordinate system aligned with the satellite longitude and latitude (green).

$$\mathbf{E}_{Y'} = \begin{bmatrix} \cos \vartheta'_s & 0 & -\sin \vartheta'_s \\ 0 & 1 & 0 \\ \sin \vartheta'_s & 0 & \cos \vartheta'_s \end{bmatrix} \quad (13)$$

and the inverse rotation matrix can be written as

$$\mathbf{E}_{Y''}^{-1} = \begin{bmatrix} \cos \vartheta'_s & 0 & \sin \vartheta'_s \\ 0 & 1 & 0 \\ -\sin \vartheta'_s & 0 & \cos \vartheta'_s \end{bmatrix} \quad (14)$$

where ϑ'_s is the polar angle to the satellite in the X' - Y' - Z' system and is given by

$$\vartheta'_s = \cos^{-1} \left(\frac{S_z}{\sqrt{S_x^2 + S_y^2 + S_z^2}} \right)$$

and $\vec{S} = (S_X, S_Y, S_Z)$ is the vector from the centre of the earth to the satellite in the earth-centred fixed coordinate system (X - Y - Z), which is provided by STK as a function of slow-time.

The third transformation rotates the X'' - Y'' - Z'' coordinate system about the Z'' -axis to create a coordinate system (X''' - Y''' - Z''') that has its Y''' -axis aligned with the y'' -axis, and its X''' -axis aligned with the x'' -axis, but pointing in the opposite direction (see Figure 7). Therefore, the required angle of rotation, δ , can be calculated using the scalar product of a unit vector along the y'' -axis (\hat{j}'') with a unit vector along the Y''' -axis (\hat{J}'''), i.e.,

$$\delta = \cos^{-1}(\hat{j}'' \cdot \hat{J}''') \quad (15)$$

To perform the scalar product, both of these unit vectors must be known in the same coordinate system. The earth-centred fixed system (X - Y - Z) is chosen as the coordinate system in which to calculate δ . Since the Y'' -axis is identical to the Y' -axis.

$$\hat{J}''' = \hat{j}'' = \begin{bmatrix} 0 \\ 1 \\ 0 \end{bmatrix} \quad (16)$$

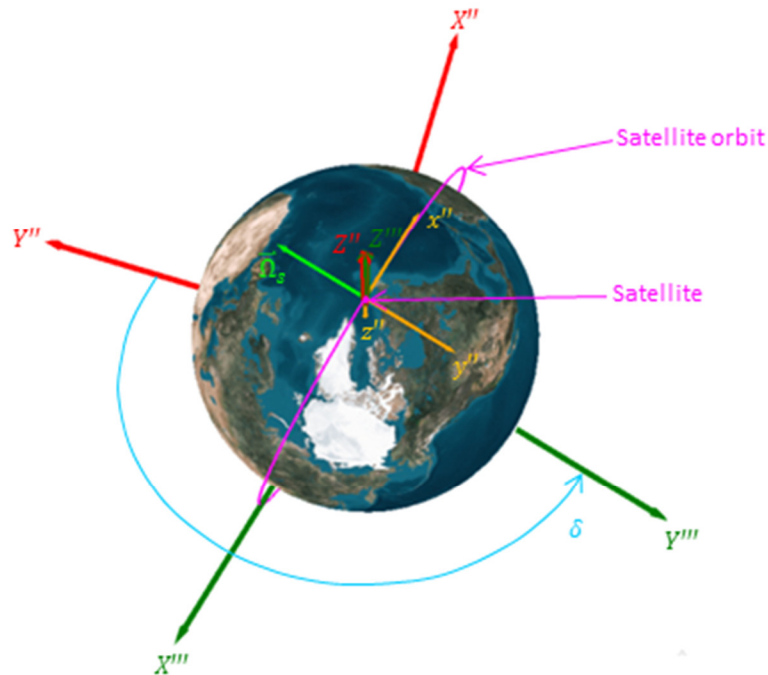


Figure 7: Earth-centred coordinate system aligned with the longitude and latitude of the satellite (red) and earth-centred coordinate system aligned with the x'' - y'' - z'' coordinate system (green).

This unit vector can be transformed into the X - Y - Z coordinate system as

$$\mathbf{E}_{Z'}^{-1} \hat{j}' = \begin{bmatrix} \cos \Phi_s & -\sin \Phi_s & 0 \\ \sin \Phi_s & \cos \Phi_s & 0 \\ 0 & 0 & 1 \end{bmatrix} \begin{bmatrix} 0 \\ 1 \\ 0 \end{bmatrix} \quad (17)$$

The unit vector along the y'' -axis (\hat{j}'') will always be aligned with the direction opposite to the orbital angular momentum vector, i.e.,

$$\hat{j}'' = \frac{-\vec{\Omega}_s}{|\vec{\Omega}_s|} \quad (18)$$

where $\vec{\Omega}_s$ is the angular momentum vector in the earth-centred fixed system (X - Y - Z) and is provided by STK as a function of slow-time. Therefore, δ can be calculated as

$$\delta = \cos^{-1} \left(\frac{-\vec{\Omega}_s \cdot \mathbf{E}_{Z'}^{-1} \hat{j}'}{|\vec{\Omega}_s|} \right) \quad (19)$$

The matrix that transforms a point in the X'' - Y'' - Z'' coordinate system to a point in the X''' - Y''' - Z''' coordinate system can then be calculated as

$$\mathbf{E}_{Z''} = \begin{bmatrix} \cos \delta & \sin \delta & 0 \\ -\sin \delta & \cos \delta & 0 \\ 0 & 0 & 1 \end{bmatrix} \quad (20)$$

and the inverse rotation matrix can be written as

$$\mathbf{E}_{Z'''}^{-1} = \begin{bmatrix} \cos \delta & -\sin \delta & 0 \\ \sin \delta & \cos \delta & 0 \\ 0 & 0 & 1 \end{bmatrix} \quad (21)$$

3.2 Signal sample calculation using a discrete reflectivity field

This section describes the mathematics of the approach used for simulating the unprocessed (raw) in-phase and quadrature signal samples recorded by a synthetic aperture radar when illuminating a reflectivity field that is approximated by a set of discrete scatterers. These quantities are digital, meaning that these are the components of the digital voltage that is the output of the analogue-to-digital converters associated with quadrature demodulation (see [14], page 144), i.e.,

$$V_{mn} = I_{mn} + jQ_{mn} \quad (22)$$

where $j = \sqrt{-1}$, and

$$\begin{aligned} m &= 0, 1, 2, \dots, M - 1 \\ n &= 0, 1, 2, \dots, N_c - 1 \end{aligned} \quad (23)$$

The number of range bins of interest (fast-time samples) is denoted with M , and N_c is the number of coherent pulses used to form the synthetic aperture (slow-time samples).

The radar transmits a Linear Frequency Modulated (LFM) pulse described by

$$p(\tau) = A_t w_r(\tau) \cos \left[2\pi f_c \left(\tau - \frac{T_p}{2} \right) + \pi K_p \left(\tau - \frac{T_p}{2} \right)^2 + \psi_t \right] \quad (24)$$

where f_c is the centre frequency of the transmitted waveform, τ is fast-time, K_p is the frequency modulation rate of the pulse, and ψ_t is a constant transmitter phase angle. It will be assumed, without loss of generality, that $\psi_t = 0$. The rectangular window function w_r is given by

$$w_r(\tau) = \text{rect} \left(\frac{\tau}{T_p} \right) = \begin{cases} 1 & \text{for } 0 \leq \tau \leq T_p \\ 0 & \text{otherwise} \end{cases} \quad (25)$$

where T_p is the pulse length. Here it has been assumed that the receiver bandwidth is much larger than the bandwidth of the transmitted pulse ($K_p T_p$). The $-T_p/2$ term is included in the phase function in Equation (24) so that the point of stationary phase occurs in the middle of the pulse. The amplitude of the transmitted waveform, A_t , is a function of the peak power, P_t , transmitted by the radar.

If the transmitted signal is backscattered by a single point scatterer at position \vec{r}_T with respect to the transmit antenna and at position \vec{r} with respect to the receive antenna, then the signal received by the radar will be

$$V(\tau) = A_r(\vec{r}_T, \vec{r}, \tau_d) w_r(\tau - \tau_d) \cos \left[2\pi f_c \left(\tau - \tau_d - \frac{T_p}{2} \right) + \pi K_p \left(\tau - \tau_d - \frac{T_p}{2} \right)^2 \right] \quad (26)$$

where time delay, τ_d , is the time required for the transmitted pulse to travel the distance to the scatterer and back, i.e.,

$$\tau_d = \frac{r_T + r}{c} \quad (27)$$

where r_T is the distance between the transmit antenna and the scatterer, r is the distance between the receive antenna and the scatterer, and c is the speed of light in the propagation medium. That is, the point scatterer will create a voltage in the receiver during the time interval $\tau_d \leq \tau \leq \tau_d + T_p$. The instantaneous amplitude of the received voltage, A_r , is proportional to the peak power received at the antenna port, P_r (see [17] page 20; [18] page 6; [19] page 52), i.e.,

$$P_r = \alpha_p \frac{1}{2Z} |A_r|^2 \quad (28)$$

where Z is the input impedance at the antenna port. The peak power received at the antenna port, and corresponding to the m^{th} fast-time range bin defined in the x - y - z coordinate system, is given by the radar equation [19], i.e.,

$$P_r(\vec{r}_m) = \frac{P_t G_s G_t G_r \lambda_c^2 \sigma_b F_T^2(r_T, \theta_T, \theta_b, \phi_T, \phi_b) F_R^2(r, \theta, \theta_b, \phi, \phi_b)}{(4\pi)^3 L_s L_a(\vec{r}_T, \vec{r}) r_T^2(r, \theta, \phi) r^2} \quad (29)$$

where P_t is the peak transmitted power, G_s is the receiver system gain, G_t is the transmit antenna gain on the beam axis of the transmit antenna, G_r is the receive antenna gain on the beam axis of the receive antenna, $\lambda_c = c/f_c$ is the transmitted radar wavelength, σ_b is the backscatter cross section of the point scatterer, F_T^2 and F_R^2 are the one-way pattern propagation factors (see [20], page 8), including attenuation due to atmospheric gases, corresponding to the path from the transmit antenna to the scatterer and from the scatterer to the receive antenna, respectively, L_s represents the system losses, L_a is the atmospheric attenuation due to precipitation, θ_b is the polar angle of both the transmit and receive beam axes, ϕ_b is the azimuth angle of both the transmit and receive beam axes, θ_T and ϕ_T specify the direction of the scatterer in the transmit antenna coordinate system, and θ and ϕ specify the direction of the scatterer in the receive antenna coordinate system. In the case of a point scatterer, the proportionality constant, α_p , is equal to one [19].

For the space-based SAR geometry, it is assumed that attenuation due to precipitation is negligible and that there is no significant anomalous propagation of the radar signal in the atmosphere. Therefore, $L_a = 1$ and the pattern propagation factors can be written as

$$\begin{aligned} F_T^2(r_T, \theta_T, \theta_b, \phi_T, \phi_b) &= f_{\theta T}^2(\theta_T, \theta_b) f_{\phi T}^2(\phi_T, \phi_b) \\ F_R^2(r, \theta, \theta_b, \phi, \phi_b) &= f_{\theta}^2(\theta, \theta_b) f_{\phi}^2(\phi, \phi_b) \end{aligned} \quad (30)$$

where $f_{\theta T}^2$, f_{θ}^2 , $f_{\phi T}^2$, and f_{ϕ}^2 are the one-way normalized transmit and receive, elevation (polar-angle) and azimuth antenna pattern factors, respectively. For MODEX modes and generic SAR systems, the antenna is modelled as a rectangular aperture. That is, the antenna pattern factors are defined as [21]

$$\begin{aligned}
f_T^2(\theta_T, \theta_b, \phi_T, \phi_b) &= f_{\theta_T}^2(\theta_T, \theta_b) f_{\phi_T}^2(\phi_T, \phi_b) \\
&= \left[\frac{1 + \cos(\Delta\beta_T)}{2} \right]^2 \left\{ \frac{\sin[\pi k_{T\phi} \sin \tilde{\phi}_T \sin \tilde{\theta}_T]}{\pi k_{T\phi} \sin \tilde{\phi}_T \sin \tilde{\theta}_T} \right\}^2 \left\{ \frac{\sin[\pi k_\theta \cos \tilde{\theta}_T]}{\pi k_\theta \cos \tilde{\theta}_T} \right\}^2
\end{aligned} \tag{31}$$

and

$$\begin{aligned}
f^2(\theta, \theta_b, \phi, \phi_b) &= f_\theta^2(\theta, \theta_b) f_\phi^2(\phi, \phi_b) \\
&= \left[\frac{1 + \cos(\Delta\beta)}{2} \right]^2 \left\{ \frac{\sin[\pi k_\phi \sin \tilde{\phi} \sin \tilde{\theta}]}{\pi k_\phi \sin \tilde{\phi} \sin \tilde{\theta}} \right\}^2 \left\{ \frac{\sin[\pi k_\theta \cos \tilde{\theta}]}{\pi k_\theta \cos \tilde{\theta}} \right\}^2
\end{aligned} \tag{32}$$

These antenna patterns describe fields of radiation that flow out along a beam axis defined by $\tilde{\theta}_T = 90^\circ$, $\tilde{\phi}_T = 0^\circ$, and $\tilde{\theta} = 90^\circ$, $\tilde{\phi} = 0^\circ$, for the transmit and receive antennas, respectively. The directions θ_T , ϕ_T , θ , and ϕ are defined relative to antenna boresight. Therefore, if the SAR beam axis is defined in a direction (θ_b, ϕ_b) that is not along the boresight, then the following transformations are required to apply Equations (31) and (32).

$$\begin{aligned}
\tilde{\theta}_T &= \cos^{-1}(-\sin \theta_T \sin \phi_T \cos \theta_b \cos \phi_b + \sin \theta_T \sin \phi_T \cos \theta_b \sin \phi_b + \cos \theta_T \sin \theta_b) \\
\tilde{\phi}_T &= \tan^{-1} \left(\frac{-\sin \theta_T \cos \phi_T \sin \phi_b + \sin \theta_T \sin \phi_T \cos \phi_b}{\sin \theta_T \cos \phi_T \sin \theta_b \cos \phi_b + \sin \theta_T \sin \phi_T \cos \theta_b \sin \phi_b + \cos \theta_T \cos \theta_b} \right) \\
\tilde{\theta} &= \cos^{-1}(-\sin \theta \sin \phi \cos \theta_b \cos \phi_b + \sin \theta \sin \phi \cos \theta_b \sin \phi_b + \cos \theta \sin \theta_b) \\
\tilde{\phi} &= \tan^{-1} \left(\frac{-\sin \theta \cos \phi \sin \phi_b + \sin \theta \sin \phi \cos \phi_b}{\sin \theta \cos \phi \sin \theta_b \cos \phi_b + \sin \theta \sin \phi \cos \theta_b \sin \phi_b + \cos \theta \cos \theta_b} \right)
\end{aligned} \tag{33}$$

The angles between the direction to the scatterer and the transmit and receive beam axes are given by $\Delta\beta_T$ and $\Delta\beta$, respectively, i.e.,

$$\begin{aligned}
\Delta\beta_T &= \cos^{-1}(\hat{u}_T \cdot \hat{u}_b) \\
\Delta\beta &= \cos^{-1}(\hat{u} \cdot \hat{u}_b)
\end{aligned} \tag{34}$$

where the directions of the scatterer are given by

$$\hat{u}_T = \begin{bmatrix} \sin \theta_T \cos \phi_T \\ \sin \theta_T \sin \phi_T \\ \cos \theta_T \end{bmatrix} \quad \hat{u} = \begin{bmatrix} \sin \theta \cos \phi \\ \sin \theta \sin \phi \\ \cos \theta \end{bmatrix} \quad (35)$$

and the direction of the beam axis is given by

$$\hat{u}_b = \begin{bmatrix} \sin \theta_b \cos \phi_b \\ \sin \theta_b \sin \phi_b \\ \cos \theta_b \end{bmatrix} \quad (36)$$

The constants k_θ , $k_{T\phi}$, and k_ϕ are numerically determined constants that set the beamwidths of the gain patterns to the desired values of $\theta_{T3} = \theta_3$, ϕ_{T3} , and ϕ_3 , respectively. For the RADARSAT-2 standard operating modes, the gain pattern factors are interpolated from an appropriate data set (see Section 7.2.2). Equation (29) can then be written as

$$P_r(\vec{r}_m) = \frac{P_t G_s G_t G_r \lambda_c^2 \sigma_b f_T^2(\theta_T, \theta_b, \phi_T, \phi_b) f^2(\theta, \theta_b, \phi, \phi_b)}{(4\pi)^3 L_s r_T^2(r, \theta, \phi) r^2} \quad (37)$$

The quadrature demodulation process will shift the received voltage signal to baseband and create two signals that are in phase quadrature. For the case of a point scatterer, these two baseband signals can be represented as the complex voltage

$$V(\tau) = A_r(\vec{r}_T, \vec{r}, \tau_d) w_r(\tau - \tau_d) \exp \left\{ j \left[2\pi f_c \left(-\tau_d - \frac{T_p}{2} \right) + \pi K_p \left(\tau - \tau_d - \frac{T_p}{2} \right)^2 \right] \right\} \quad (38)$$

Note that the carrier signal present in Equation (26), $\exp(j 2\pi f_c \tau)$, has been removed by the low-pass filtering of the quadrature demodulation process. Consequently, the first term of the phase function in Equation (38) corresponds only to the echo phase.

If the received analogue voltage signal, V , is sampled at some time, $\tau_m = 2r_m/c$, that is between τ_d and $\tau_d + T_p$, then the analogue-to-digital converters of the quadrature demodulation process will produce I and Q values such that $\sqrt{I^2 + Q^2}$ is equal to the amplitude of $V(\tau_m)$ and $\tan^{-1}(Q/I)$ is equal to the phase of $V(\tau_m)$.

If there is more than one scatterer within the radar resolution volume, then the sampling process will sum all of the scattered signals that arrive at the antenna port at time τ_m . In this case, the signal samples will be given by

$$\begin{aligned}
V_m(\vec{r}_m) = & \sum_{\ell=0}^{N_s-1} A_{r\ell}(\vec{r}_{T\ell}, \vec{r}_\ell, \vec{r}_m) w_r(\tau_m - \tau_{d\ell}) \times \dots \\
& \dots \exp \left\{ j \left[2\pi f_c \left(-\tau_{d\ell} - \frac{T_p}{2} \right) + \pi K_p \left(\tau_m - \tau_{d\ell} - \frac{T_p}{2} \right)^2 \right] \right\}
\end{aligned} \tag{39}$$

where N_s is the number of scatterers that can reflect the transmitted pulse such that any portion of the reflected pulse will arrive at the antenna port at the sample time τ_m , the \times symbol represents multiplication, and the \dots symbol is used to show that the equation is one continuous expression that could not fit onto one line of text. The left hand side of Equation (39) is a complex number ($V_m = I_m + jQ_m$) corresponding to a particular range bin at range $r_m(\tau_m)$ (slow-time dependence is not considered yet). Use of Equations (28) and (37) to replace the received amplitude, A_r , and Equation (27) to replace the time delay, τ_d , gives

$$\begin{aligned}
V_m(\vec{r}_m) = & \sum_{\ell=0}^{N_s-1} \left[\frac{2 P_t G_s G_t G_r \lambda_c^2 f_T^2(\theta_{T\ell}, \theta_b, \phi_{T\ell}, \phi_b) f^2(\theta_\ell, \theta_b, \phi_\ell, \phi_b) Z \sigma_{b\ell}}{(4\pi)^3 L_s r_{T\ell}^2(r, \theta, \phi) r_\ell^2} \right]^{\frac{1}{2}} \times \dots \\
& \dots w_r \left(\tau_m - \frac{r_{T\ell} + r_\ell}{c} \right) \exp \left\{ j \left[2\pi f_c \left(-\frac{r_{T\ell} + r_\ell}{c} - \frac{T_p}{2} \right) + \pi K_p \left(\tau_m - \frac{r_{T\ell} + r_\ell}{c} - \frac{T_p}{2} \right)^2 \right] \right\}
\end{aligned} \tag{40}$$

To form the synthetic aperture, the radar transmits a set of N_c coherent pulses with pulse repetition interval T_s . These pulses are transmitted at slow-times, t_n , given by

$$t_n = n T_s \quad \text{where } n = 0, 1, 2, \dots, N_c - 1 \tag{41}$$

Therefore, the complex signal samples can be written as a function of both fast-time and slow-time as

$$\begin{aligned}
V_{mn}(\vec{r}_m, t_n) = & \left[\frac{2 P_t G_s G_t G_r \lambda_c^2 Z}{(4\pi)^3 L_s} \right]^{\frac{1}{2}} \times \dots \\
& \dots \sum_{\ell=0}^{N_s-1} \left[\frac{f_T^2(\theta_{T\ell n}, \theta_b, \phi_{T\ell n}, \phi_b) f^2(\theta_{\ell n}, \theta_b, \phi_{\ell n}, \phi_b) \sigma_{b\ell}}{r_{T\ell n}^2(r, \theta, \phi) r_{\ell n}^2} \right]^{\frac{1}{2}} w_r \left(\tau_m - \frac{r_{T\ell n} + r_{\ell n}}{c} \right) \times \dots \\
& \dots \exp \left\{ j \left[2\pi f_c \left(-\frac{r_{T\ell n} + r_{\ell n}}{c} - \frac{T_p}{2} \right) + \pi K_p \left(\tau_m - \frac{r_{T\ell n} + r_{\ell n}}{c} - \frac{T_p}{2} \right)^2 \right] \right\}
\end{aligned} \tag{42}$$

Since the SAR platform moves a distance of $v_p T_s$ during the time of the pulse repetition interval, the locations of the fixed scatterers in the coordinate systems of the SAR antennas will change from pulse to

pulse. This slow-time dependence is exhibited in Equation (42) by including the subscript n on the scatterer coordinates.

In the current implementation of this model, all of the discrete scatterers defining the reflectivity field are assumed to be on the surface of the WGS 84 ellipsoid, which is defined as an oblate ellipsoid of revolution having an equatorial radius of 6.378137×10^6 m and a polar radius of $6.356752314245179 \times 10^6$ m. Consequently, terrain height is not explicitly considered in this document. Since the reflectivity field is based upon an actual SAR image, then terrain shadowing and other terrain-related effects are implicit in this reflectivity field. Explicit consideration of terrain height in the above calculations would then effectively include these effects twice. Regardless, a faithful representation of the real world signals corresponding to a specific SAR image is not the end objective of this research. The goal of the signal simulation is to generate realistic I and Q signal samples that can be used to test the effects of jamming and to investigate potential electronic protection measures.

3.2.1 Point scatterer radar cross section

Evaluation of Equation (42) first requires the reflectivity field to be defined in terms of a set of discrete scatterers. The scatterer locations are defined in terms of the RADARSAT-2 product image coordinate system (line, pixel) as follows:

$$\begin{aligned}\mathcal{L}_\ell &= \frac{(\ell \bmod N_{I\phi})}{N_{P\phi}} - \frac{1}{N_{P\phi}} \left\lfloor \frac{N_{P\phi}}{2} \right\rfloor + \frac{\mathbb{W}_\ell}{2} \cos(2\pi\mathbb{W}_\ell - \pi) + \frac{\lambda_c}{\delta_\phi \sin Y_N} \\ \wp_\ell &= \frac{1}{N_{Pr}} \left\lfloor \frac{\ell}{N_{I\phi}} \right\rfloor - \frac{1}{N_{Pr}} \left\lfloor \frac{N_{Pr}}{2} \right\rfloor + \frac{\mathbb{W}_{iq}}{2} \cos(2\pi\mathbb{W}_{iq} - \pi) + \frac{\lambda_c}{\delta_r \sin Y_N} \\ \ell &= 0, 1, 2, \dots, N_{Ir} N_{I\phi} - 1\end{aligned}\tag{43}$$

where \mathcal{L}_ℓ is the line value corresponding to the ℓ^{th} scatterer, $N_{I\phi}$ and N_{Ir} are the number of lines and pixels in the RADARSAT-2 product image data, respectively, $N_{P\phi}$ is a user supplied parameter specifying the number of scatterers per image pixel in the azimuth direction, \mathbb{W}_{iq} is a set of uniformly distributed random numbers between 0 and 1, δ_ϕ is the image azimuth pixel spacing, Y_N is the incidence angle at near range at mid-azimuth position of the image, and the operator $\lfloor \cdot \rfloor$ converts its argument to the nearest integer that is smaller than the argument. Similarly, \wp_ℓ is the pixel value corresponding to the ℓ^{th} scatterer, N_{Pr} is a user supplied parameter specifying the number of scatterers per image pixel in the range direction, and δ_r is the image range pixel spacing. The quantities $N_{I\phi}$, N_{Ir} , δ_ϕ , δ_r , and Y_N are supplied in the RADARSAT-2 metadata [13]. Equation (43) creates a regular grid of scatterer locations and then randomizes each position within a distance of less than or equal to one wavelength. The randomization mimics the random scatterer locations that would be observed by the SAR in the real world.

The RCS corresponding to each scatterer, $\sigma_{b\ell}$, is a function of the reflectivity observed by the radar system, η_ℓ , within the Earth's surface area that the scatterer represents, i.e.,

$$\sigma_{b\ell} = \eta_\ell \left(\frac{\delta_r}{N_{Pr}} \right) \left(\frac{\delta_\phi}{N_{P\phi}} \right) \quad (44)$$

The incidence angle of the measurement and the local terrain slope would need to be considered if η_ℓ is to be derived from the intrinsic reflectivity associated with the terrain type being illuminated. Establishing the relationship between η_ℓ and intrinsic reflectivity is not necessary if the observed reflectivity (radar brightness) of the surface is known. The radar brightness, β^o , has been recommended by the Committee for Earth Observation Satellites (CEOS) SAR Calibration Working Group [22] as the most appropriate radiometric attribute for SAR images when the local terrain slope and illumination angles are not exactly known. Therefore, if a SAR image is used to represent the surface reflectivity field and the β^o values corresponding to this image are available, then $\sigma_{b\ell}$ can be calculated as

$$\sigma_{b\ell} = \beta_\ell^o \left(\frac{\delta_r}{N_{Pr}} \right) \left(\frac{\delta_\phi}{N_{P\phi}} \right) \quad (45)$$

The radar brightness corresponding to each of the N_s scatterers, β_ℓ^o , is interpolated from a data field that is derived from the RADARSAT-2 product image data and look-up tables of scaling values as described in [13], and that is specified in terms of the line and pixel dimensions.

3.2.2 Resolution volume

At a sample time τ_m , for the case of a monostatic antenna, the front edge of the radar pulse will have travelled to and from a range of $c\tau_m/2$, and the back edge of the radar pulse will have travelled to and from a range of $c(\tau_m - T_p)/2$. Therefore, only the signals backscattered from scatterers within the spherical shell at ranges between $c(\tau_m - T_p)/2$ and $c\tau_m/2$ can contribute to the signal sample collected at time τ_m . If r_m is defined to be the range at the centre of this spherical shell, then the sample time is given by

$$\tau_m = \frac{2 r_m}{c} + \frac{T_p}{2} \quad (46)$$

The window function w_r is approximated in the coordinate system of the receive antenna assuming a monostatic antenna and a receiver bandwidth that is much larger than the bandwidth of the transmitted pulse. That is, only scatterers lying within the spherical range shell defined by $r_m - c T_p/4 \leq r \leq r_m + c T_p/4$ are included in the summation of Equation (42), and each scatterer will receive the same range weight regardless of where it is situated within the resolution volume. This “range weighting,” along with the weighting applied by the antenna gain patterns, requires the locations of the scatterers to be known in the coordinate systems of the transmit and receive antennas.

Equation (43) defines the scatterer locations in terms of RADARSAT-2 product image coordinates. These line and pixel values are transformed to longitudes (Φ_ℓ) and latitudes (Θ_ℓ) on the surface of the WGS 84 ellipsoid using the MacDonald, Dettwiler, and Associates Ltd. (MDA) forward geolocation algorithm [23], which uses the tie point data provided in the RADARSAT-2 metadata [13].

The coordinates of the discrete scatterers can be calculated in the radar-centred coordinate systems for each slow-time using the transformations defined in Section 3.1. The Cartesian coordinates of the scatterer locations are first calculated in the earth-centred fixed coordinate system as

$$Z_\ell = \sqrt{\frac{1}{\frac{\tan^2(90^\circ - \Theta_{c\ell})}{R_e^2} + \frac{1}{R_p^2}}} \quad (47)$$

$$X_\ell = \begin{cases} -\sqrt{Z_\ell^2 \cos^2 \Phi_\ell \tan^2(90^\circ - \Theta_{c\ell})} & \text{for } 90^\circ \leq \Phi_\ell < 270^\circ \\ +\sqrt{Z_\ell^2 \cos^2 \Phi_\ell \tan^2(90^\circ - \Theta_{c\ell})} & \text{for } \Phi_\ell < 90^\circ \text{ or } \Phi_\ell \geq 270^\circ \end{cases} \quad (48)$$

$$Y_\ell = X_\ell \tan \Phi_\ell \quad (49)$$

where R_e and R_p are the equatorial and polar radii of the WGS 84 ellipsoid, respectively, Φ_ℓ is the longitude of the ℓ^{th} scatterer, and $\Theta_{c\ell}$ is the geocentric latitude of the ℓ^{th} scatterer given by

$$\Theta_{c\ell} = \tan^{-1}[(1 - e_E^2) \tan \Theta_\ell] \quad (50)$$

where Θ_ℓ is the latitude of the ℓ^{th} scatterer, and e_E is the eccentricity of the earth defined by

$$e_E = \sqrt{\frac{2(R_e - R_p)}{R_e} - \frac{(R_e - R_p)^2}{R_e^2}} \quad (51)$$

The scatterer locations can be transformed from the earth-centred fixed system into the X''' - Y''' - Z''' coordinate system as

$$\vec{R}_{\ell n}''' = \mathbf{E}_{Z''n} [\mathbf{E}_{Y'n} (\mathbf{E}_{Zn} \vec{R}_\ell)] \quad (52)$$

where $\vec{R}_\ell = (X_\ell, Y_\ell, Z_\ell)$ and $\vec{R}_{\ell n}''' = (X_{\ell n}''', Y_{\ell n}''', Z_{\ell n}''')$. The matrix \mathbf{E}_{Zn} (see Equation (11)) is given a subscript n since it is a function of the longitude of the satellite, Φ_{sn} , which depends upon slow-time. Similarly, $\mathbf{E}_{Y'n}$ (see Equation (13)) is a function of $\vartheta'_{sn}(\vec{S}_n)$, and $\mathbf{E}_{Z''n}$ (see Equation (20)) is a function of $\delta_n(\vec{\Omega}_{sn}, \Phi_{sn})$. Consequently, the positions of the scatterers in the X''' - Y''' - Z''' coordinate system are also a function of slow-time. The scatterer locations can then be described in the transmit antenna coordinate system as

$$\vec{r}_{T\ell n} = \begin{bmatrix} x_{T\ell n} \\ y_{T\ell n} \\ z_{T\ell n} \end{bmatrix} = \mathbf{A} \begin{bmatrix} S_{Zn}''' - Z_{\ell n}''' \\ -X_{\ell n}''' \\ Y_{\ell n}''' \end{bmatrix} \quad (53)$$

where S_{Zn}''' is the Z-component of $\vec{S}_n''' = \mathbf{E}_{Z'n}[\mathbf{E}_{Y'n}(\mathbf{E}_{Zn} \vec{S}_n)]$, and the spherical polar coordinates corresponding to the transmit antenna coordinate system that are required to evaluate Equation (42) are given by

$$\begin{aligned} r_{T\ell n} &= \sqrt{x_{T\ell n}^2 + y_{T\ell n}^2 + z_{T\ell n}^2} \\ \theta_{T\ell n} &= \cos^{-1} \left(\frac{z_{T\ell n}}{\sqrt{x_{T\ell n}^2 + y_{T\ell n}^2 + z_{T\ell n}^2}} \right) \\ \phi_{T\ell n} &= \tan^{-1} \left(\frac{y_{T\ell n}}{x_{T\ell n}} \right) \end{aligned} \quad (54)$$

The Cartesian coordinates of the scatterers in the receive antenna coordinate system are given by

$$\begin{aligned} x_{\ell n} &= x_{T\ell n} \\ y_{\ell n} &= y_{T\ell n} - \Delta y \\ z_{\ell n} &= z_{T\ell n} \end{aligned} \quad (55)$$

and the corresponding spherical polar coordinates of the scatterers in the receive antenna coordinate system that are required to evaluate Equation (42) are

$$\begin{aligned} r_{\ell n} &= \sqrt{x_{\ell n}^2 + y_{\ell n}^2 + z_{\ell n}^2} \\ \theta_{\ell n} &= \cos^{-1} \left(\frac{z_{\ell n}}{\sqrt{x_{\ell n}^2 + y_{\ell n}^2 + z_{\ell n}^2}} \right) \\ \phi_{\ell n} &= \tan^{-1} \left(\frac{y_{\ell n}}{x_{\ell n}} \right) \end{aligned} \quad (56)$$

To reduce computer memory requirements, the scatterer coordinates for each radar resolution volume are calculated as required, instead of calculating N_c sets of $N_{I\phi} \times N_{P\phi} \times N_{Ir} \times N_{Pr}$ coordinates in advance. This means that the intersection of the radar resolution volume with the surface of the WGS 84 ellipsoid must be calculated for each range bin. The bounds of the radar resolution volume are defined in the receive antenna coordinate system, e.g., $r_m - c T_p/4 \leq r \leq r_m + c T_p/4$. Consequently, the coordinates of where these bounds intersect the surface of the earth must be transformed into longitude and latitude so that it can be compared with the longitudes and latitudes of the scatterers. This corresponds to the problem of calculating the polar angle, θ , at which a ray transmitted from the radar intersects the earth for a known range, r , and azimuth, ϕ . This is a complex calculation that requires an iterative solution. The details of an algorithm for performing the calculations of Earth intersection points are provided in Annex A.

3.3 Signal samples derived from real data

This section describes the decompression and scaling of RADARSAT-2 MODEX raw range-compressed data. The aim is to provide a data set of signal samples that can be used to evaluate the simulated signal samples discussed in Section 3.2.

The range-compressed signal samples are denoted with the prime symbol, i.e., the raw range-compressed signal samples read directly from the RADARSAT-2 MODEX data files are specified as

$$V'_{mn} = I'_{mn} + j Q'_{mn} \quad (57)$$

The decompression process requires a zero-padded replica of the transmitted pulse, i.e.,

$$\tilde{V}_{Rm} = \begin{cases} \exp \left[j \pi K_p \left(\tau_m - \frac{T_p}{2} \right)^2 \right] & \text{for } 0 \leq m \leq T_p f_s - 1 \\ 0 + j0 & \text{for } T_p f_s \leq m \leq N_p - 1 \end{cases} \quad (58)$$

where the subscript R is only used here to denote the pulse replica, and the \sim symbol is used to denote a padded signal. The radar sampling frequency, f_s , is such that $T_p f_s$ is an integer. The time variable τ_m is calculated as

$$\tau_m = \frac{m}{f_s} \quad \text{for } m = 0, 1, \dots, N_p - 1 \quad (59)$$

where the number of elements in the zero-padded pulse replica, N_p , is given by

$$N_p = 2^{\left\lceil \frac{\ln(M + T_p f_s - 1)}{\ln(2)} \right\rceil} \quad (60)$$

and the operator $\lceil \cdot \rceil$ returns the nearest larger integer of its argument.

The decompression is performed in the frequency domain. That is the padded decompressed signal is calculated as

$$\tilde{V}_{mn} = \frac{\mathbf{DFT}_m^{-1}\{ (\mathbf{DFT}_m\{\tilde{V}'_{mn}\} \sqrt{N_p}) (\mathbf{DFT}_m\{\tilde{V}_{Rm}\} \sqrt{N_p}) \}}{\sqrt{N_p}} \quad (61)$$

where the forward and inverse Discrete Fourier Transforms (DFT) are defined as

$$\begin{aligned} F(u) &= \mathbf{DFT}\{f(y)\} = \frac{1}{N_f} \sum_{y=0}^{N_f-1} f(y) \exp\left(\frac{-j 2\pi u y}{N_f}\right) \\ f(y) &= \mathbf{DFT}^{-1}\{F(u)\} = \sum_{u=0}^{N_f-1} F(u) \exp\left(\frac{j 2\pi u y}{N_f}\right) \end{aligned} \quad (62)$$

The subscript m on \mathbf{DFT} and \mathbf{DFT}^{-1} in Equation (61) indicates that the transforms are one-dimensional and performed along the fast-time dimension. The normalization factors, $\sqrt{N_p}$ and $1/\sqrt{N_p}$, are used to maintain the power of the complex signals constant before and after the forward or inverse DFT, respectively. The padded range-compressed signal is given by

$$\tilde{V}'_{mn} = \begin{cases} V'_{mn} & \text{for } 0 \leq i \leq M-1 \\ 0 + j0 & \text{for } M \leq i \leq N_p-1 \end{cases} \quad (63)$$

The signal padding of the decompressed MODEX data, \tilde{V}_{mn} , is maintained throughout the coherent signal combination represented by Equation (1) to ensure that no accuracy is lost when the signals are recompressed in the image formation process. The excess signal samples will be cast off in the range compression process (see Annex B.1). Similarly, range registration is not performed as part of the decompression process since the effect will be reversed during the range compression process. The decompressed signal samples must, however, be scaled to the levels that would have been measured by the simulated SAR in the simulated environment.

The required scaling factor is derived from the received power that would be measured by the simulated SAR for a reference pulse at $n = N_c/2$. The power received for a range bin \vec{r}_m will be the weighted integral of the continuous reflectivity field that is within the radar resolution volume, \mathcal{V} , [19], i.e.,

$$P_{m \frac{N_c}{2}}(\vec{r}_m) = \int_{\mathcal{V}} \frac{P_t G_s G_t G_r \lambda_c^2 |W_s|^2 f_T^2 f^2 \eta}{(4\pi)^3 L_s r_T^2 r^2} d\mathcal{V} \quad (64)$$

where η is reflectivity, and W_s is a range weighting function determined by the pulse length and the receiver bandwidth. The reflectivity, η , will have units of $\text{m}^2 \text{m}^{-3}$ and will vary continuously as a function of space.

Expanding the volume element into spherical polar coordinates, corresponding to the receive antenna coordinate system, allows Equation (64) to be written as

$$P_{m \frac{N_c}{2}}(\vec{r}_m) = \int_{r_m - \frac{c T_p}{4}}^{r_m + \frac{c T_p}{4}} \int_0^\pi \int_{\phi_b - \frac{\pi}{2}}^{\phi_b + \frac{\pi}{2}} \frac{P_t G_s G_t G_r \lambda_c^2}{(4\pi)^3 L_s} \times \dots \quad (65)$$

$$\dots \frac{f_T^2(\theta_T, \theta_b, \phi_T, \phi_b) f^2(\theta, \theta_b, \phi, \phi_b) \eta(r, \theta, \phi)}{r_T^2(r, \theta, \phi) r^2} r^2 \sin \theta \, d\phi \, d\theta \, dr$$

The limits of integration used in Equation (65) define the region of space, \mathcal{U} , that can reflect the transmitted pulse such that any portion of the reflected pulse will arrive at the antenna port at the sample time, τ_m . As in the case of discrete reflectivity (Section 3.2), the region of space to be integrated over is approximated as the radar resolution volume corresponding to a monostatic antenna and a receiver bandwidth that is much larger than the pulse bandwidth, and defined in the coordinate system of the receive antenna. The range integration limits incorporate the term $|W_s|^2$ in Equation (64) such that the receiver range weighting of each echo originating within the resolution volume is the same. The angular limits simply define the region of space that exists in front of the radar antenna.

Since the SAR is designed to only measure the signals backscattered from the surface of the earth, η is set to be non-zero only at the surface, i.e.,

$$\eta(r, \theta, \phi) = \begin{cases} \eta_e & \text{for } \theta = \theta_e(r, \phi) \\ 0 & \text{otherwise} \end{cases} \quad (66)$$

where η_e has units of $\text{m}^2 \text{m}^{-2}$. Since the surface of the earth is considered as an ellipsoid, the polar angle to the earth's surface, θ_e , is a function of both range and azimuth. The specific dependence of θ_e on r and ϕ is related to the earth intersection point calculation discussed in Annex A.

Applying the Dirac delta function [24], $\delta(\theta - \theta_e)/(r \sin \theta)$, to the polar angle integral of Equation (65) gives

$$P_{m \frac{N_c}{2}}(\vec{r}_m) = \int_{r_m - \frac{c T_p}{4}}^{r_m + \frac{c T_p}{4}} \int_{\phi_b - \frac{\pi}{2}}^{\phi_b + \frac{\pi}{2}} \frac{P_t G_s G_t G_r \lambda_c^2}{(4\pi)^3 L_s} \times \dots \quad (67)$$

$$\dots \frac{f_T^2(\theta_{Te}, \theta_b, \phi_T, \phi_b) f^2(\theta_e, \theta_b, \phi, \phi_b) \eta_e(r, \theta_e, \phi)}{r_T^2(r, \theta_e, \phi) r} d\phi \, dr$$

Equation (67) is evaluated by first breaking the integrals into the sum of many integrals spanning regions that are small enough such that quantities within the integrands do not vary significantly over the region of integration. For example, the azimuth integral of Equation (67) can be rewritten such that

$$\begin{aligned}
P_{m \frac{N_c}{2}}(\vec{r}_m) = & \int_{r_m - \frac{c T_p}{4}}^{r_m + \frac{c T_p}{4}} \sum_{q=0}^{Q-1} \int_{\phi_b - \frac{\pi}{2} + q \Delta \phi}^{\phi_b - \frac{\pi}{2} + (q+1) \Delta \phi} \frac{P_t G_s G_t G_r \lambda_c^2}{(4\pi)^3 L_s} \times \dots \\
& \dots \frac{f_T^2(\theta_{Te}, \theta_b, \phi_T, \phi_b) f^2(\theta_e, \theta_b, \phi, \phi_b) \eta_e(r, \theta_e, \phi)}{r_T^2(r, \theta_e, \phi) r} d\phi dr
\end{aligned} \tag{68}$$

For large Q , or equivalently, small $\Delta\phi = \pi/Q$, the quantities of the azimuth integrand can be removed from the integral, i.e.,

$$\begin{aligned}
P_{m \frac{N_c}{2}}(\vec{r}_m) = & \int_{r_m - \frac{c T_p}{4}}^{r_m + \frac{c T_p}{4}} \sum_{q=0}^{Q-1} \frac{P_t G_s G_t G_r \lambda_c^2}{(4\pi)^3 L_s} \times \dots \\
& \dots \frac{f_T^2(\theta_{Te}(r, \phi_q), \theta_b, \phi_{Tq}, \phi_b) f^2(\theta_e(r, \phi_q), \theta_b, \phi_q, \phi_b) \eta_e(r, \theta_e(r, \phi_q), \phi_q)}{r_T^2(r, \theta_e(r, \phi_q), \phi_q) r} \Delta\phi dr
\end{aligned} \tag{69}$$

where

$$\Delta\phi = \frac{\Delta a_\phi}{r} = \int_{\phi_b - \frac{\pi}{2} + q \Delta\phi}^{\phi_b - \frac{\pi}{2} + (q+1) \Delta\phi} d\phi \tag{70}$$

and

$$\phi_q = \phi_b - \frac{\pi}{2} + \Delta\phi \left(q + \frac{1}{2} \right) = \phi_b - \frac{\pi}{2} + \frac{\pi}{Q} \left(q + \frac{1}{2} \right) \tag{71}$$

The arc length, Δa_ϕ , is a constant value chosen to be small enough to resolve the variations in the reflectivity field. Consequently, the azimuth interval, $\Delta\phi$, will vary with range and this allows the spatial resolution of the summed samples representing the azimuth integral to be independent of range.

Repeating this process for the range integral gives

$$\begin{aligned}
P_{m \frac{N_c}{2}}(\vec{r}_m) = & \sum_{i=0}^{R-1} \int_{r_m - \frac{c T_p}{4} + i \Delta r}^{r_m - \frac{c T_p}{4} + (i+1) \Delta r} \sum_{q=0}^{Q-1} \frac{P_t G_s G_t G_r \lambda_c^2}{(4\pi)^3 L_s} \times \dots \\
& \dots \frac{f_T^2(\theta_{Te}(r, \phi_q), \theta_b, \phi_{Tq}, \phi_b) f^2(\theta_e(r, \phi_q), \theta_b, \phi_q, \phi_b) \eta_e(r, \theta_e(r, \phi_q), \phi_q)}{r_T^2(r, \theta_e(r, \phi_q), \phi_q) r} \frac{\Delta a_\phi}{r} dr
\end{aligned} \tag{72}$$

For large R , or equivalently, small $\Delta r = c T_p / 2R$, the quantities η_e , f_T^2 , and f^2 can be removed from the range integral. In addition, the ranges to the radar resolution volume, r_T and r will be much greater than the range interval, Δr , required to resolve the variations in the reflectivity field. Therefore, these range terms can also be removed from the range integral. This gives

$$P_{m \frac{N_c}{2}}(\vec{r}_m) = \sum_{i=0}^{R-1} \sum_{q=0}^{Q-1} \frac{P_t G_s G_t G_r \lambda_c^2 \Delta a_\phi \Delta r}{(4\pi)^3 L_s} \times \dots \quad (73)$$

$$\dots \frac{f_T^2(\theta_{Ti q}, \theta_b, \phi_{Ti q}, \phi_b) f^2(\theta_{i q}, \theta_b, \phi_{i q}, \phi_b) \eta_e(r_i, \theta_{i q}, \phi_{i q})}{r_T^2(r_i, \theta_{i q}, \phi_{i q}) r_i^2}$$

where

$$r_i = r_m - \frac{c T_p}{4} + \Delta r \left(i + \frac{1}{2} \right) = r_m - \frac{c T_p}{4} + \frac{c T_p}{2 R} \left(i + \frac{1}{2} \right) \quad (74)$$

and

$$\phi_{i q} = \phi_b - \frac{\pi}{2} + \frac{\Delta a_\phi}{r_i} \left(q + \frac{1}{2} \right) = \phi_b - \frac{\pi}{2} + \frac{\pi}{Q_i} \left(q + \frac{1}{2} \right) \quad (75)$$

$$Q_i = \frac{\pi r_i}{\Delta a_\phi}$$

For given values of r_i and $\phi_{i q}$, the polar angle to the surface, $\theta_{i q} = \theta_e(r_i, \phi_{i q})$, is calculated using the iterative algorithm in Annex A. Once $\theta_{i q}$ is determined, the spherical polar coordinates to the surface point in the transmit antenna coordinate system can be calculated as

$$r_{Ti} = \sqrt{r_i^2 + 2 \Delta y r_i \sin \theta_{i q} \sin \phi_{i q} + (\Delta y)^2}$$

$$\theta_{Ti q} = \theta_{Te}(r_i, \phi_{i q}) = \cos^{-1} \left[\frac{r_i \cos \theta_{i q}}{\sqrt{r_i^2 + 2 \Delta y r_i \sin \theta_{i q} \sin \phi_{i q} + (\Delta y)^2}} \right] \quad (76)$$

$$\phi_{Ti q} = \tan^{-1} \left(\frac{r_i \sin \theta_{i q} \sin \phi_{i q} + \Delta y}{r_i \sin \theta_{i q} \cos \phi_{i q}} \right)$$

The antenna pattern factors, f_T^2 and f^2 , are evaluated using Equations (31) and (32), respectively.

The reflectivity field denoted by η_e is derived from the MODEX data. That is, range cell migration correction (Annex B.2) and azimuth compression (Annex B.3) are applied to the raw range-compressed data, V'_{mn} , and the result is converted into radar brightness or observed reflectivity, β^o , using the approach described in [13] and the look-up table data provided with the RADARSAT-2 metadata. The resulting β^o array will have $N_{I\phi} \times N_{Ir}$ values with the associated array indices corresponding to line and pixel values. The η_e values required to evaluate Equation (73) are interpolated from this β^o array.

Interpolation of η_e from β^o requires the locations of the η_e values, $(r_i, \theta_{iq}, \phi_{iq})$, to be transformed into longitude and latitude values, and then into line and pixel values. Using the transformations defined in Section 3.1, the longitudes and latitudes can be written as

$$\begin{aligned}\Phi_{iq} &= \tan^{-1} \left(\frac{Y_{iq}}{X_{iq}} \right) \\ \Theta_{iq} &= \tan^{-1} \left(\frac{\tan \Theta_{iqc}}{1 - e_E^2} \right)\end{aligned}\tag{77}$$

where

$$\Theta_{iqc} = 90^\circ - \cos^{-1} \left(\frac{Z_{iq}}{\sqrt{X_{iq}^2 + Y_{iq}^2 + Z_{iq}^2}} \right)\tag{78}$$

$$\begin{bmatrix} X_{iq} \\ Y_{iq} \\ Z_{iq} \end{bmatrix} = \mathbf{E}_{Z'}^{-1} \left\{ \mathbf{E}_{Y''}^{-1} \left(\mathbf{E}_{Z'''}^{-1} \begin{bmatrix} -y' \\ z' \\ S_{Z'''} - x' \end{bmatrix} \right) \right\}\tag{79}$$

$$\begin{bmatrix} x' \\ y' \\ z' \end{bmatrix} = \mathbf{A}^{-1} \begin{bmatrix} r_i \sin \theta_{iq} \cos \phi_{iq} \\ r_i \sin \theta_{iq} \sin \phi_{iq} + \Delta y \\ r_i \cos \theta_{iq} \end{bmatrix}\tag{80}$$

The associated line and pixel values, \mathcal{L}_{iq} and \mathcal{P}_{iq} , are calculated using the MDA reverse geolocation algorithm based on rational functions [23] and the associated data provided with the RADARSAT-2 metadata.

The calculated received power is used to scale the decompressed signal samples, i.e.,

$$\tilde{V}_{mn} \rightarrow \tilde{V}_{mn} \left\{ \frac{\sum_{m=T_p f_s}^{M-T_p f_s} \sqrt{2 Z P_m \frac{N_c}{2}}}{\sum_{m=T_p f_s}^{M-T_p f_s} \left| \tilde{V}_{\left(m + \left\lfloor \frac{T_p f_s}{2} \right\rfloor\right)n} \right|} \right\} \quad (81)$$

The indexing used in the summation accounts for range registration associated with the decompression process, and excludes $T_p f_s$ samples at either end of the range interval to avoid regions where the radar resolution volume has extended beyond the region where reflectivity is defined. The decompressed, padded, signal samples, \tilde{V}_{mn} , are now scaled such that they are consistent in terms of amplitude with the test target and jammer signal samples measured by the simulated SAR in the simulated environment.

4 Test targets

The signal samples corresponding to backscattering from multiple test targets are calculated similarly to those corresponding to the discrete scatterers used to represent the surface of the earth (Section 3.2, Equation (42)). The slow-time dependence of the signal samples will be mainly dictated by the change in the test target locations, as measured in the transmit and receive antenna coordinate systems, that are caused by the motion of the satellite. The antenna gain patterns, the rectangular window function, and the phase function will all depend upon the test target locations and hence depend upon slow-time.

The signal samples measured by a SAR will also fluctuate in a random manner as a function of slow-time. Each of the many scatterers that contribute backscattered power to a given signal sample will be randomly positioned with respect to each other and they may move relative to each other with different velocities according to their individual properties. The relative positions of even stationary scatterers will change as the SAR moves. Consequently, the amplitude and phase of the sum of the backscattered waves will vary in an effectively random manner as a function of slow-time. This variation was modelled explicitly for the signal samples received from the surface of the earth by summing millions of received signals for each range bin. The backscatter cross section of a complex target will also vary as a function of slow-time since the target will consist of multiple scattering centres whose relative locations will vary as a function of the aspect at which the target is viewed by the SAR. However, in this research, the test targets are not explicitly modelled as complex structures with multiple scattering centres. Instead, each test target is associated with a mean backscatter cross section, $\sigma_{b\kappa}$, which does not depend upon slow-time, and the signal fluctuations associated with the multiple scattering centres will be introduced statistically. Explicit modelling of complex structures could be attempted by defining a discrete Swerling 0 (see [11], p. 66) target for each of the scattering centres associated with a complex test target and positioning them close together. While this should be possible in this model, it will require more computer execution time than a statistical approach, and it will be limited to complex targets that can be accurately described by a finite set of discrete scattering centres.

Target dynamics (velocity and acceleration) are not included in the current version of the simulation. However, the time-domain approach should allow this to be easily included in future, if required.

4.1 Signal sample calculation

The signal samples corresponding to multiple test targets are calculated as

$$V_{mn}(r_m, t_n) = \sum_{\kappa=0}^{N_T-1} w_r \left(\tau_m - \frac{2 r_{\kappa n}}{c} \right) \check{V}_{mn\kappa}(r_m, t_n) \quad (82)$$

where N_T is the number of test targets defined, $\check{V}_{mn\kappa}$ represents the ungated fluctuating signal samples corresponding to the κ^{th} target, and the ungated non-fluctuating signal samples are given by

$$V_{mn\kappa}(r_m, t_n) = \left[\frac{2 P_t G_s G_t G_r \lambda_c^2 f_T^2 (\theta_{T\kappa n}, \theta_b, \phi_{T\kappa n}, \phi_b) f^2 (\theta_{\kappa n}, \theta_b, \phi_{\kappa n}, \phi_b) Z \sigma_{b\kappa}}{(4\pi)^3 L_s r_{T\kappa n}^2 (r, \theta, \phi) r_{\kappa n}^2} \right]^{\frac{1}{2}} \times \dots \quad (83)$$

$$\dots \exp \left\{ j \left[2\pi f_c \left(-\frac{r_{T\kappa n} + r_{\kappa n}}{c} - \frac{T_p}{2} \right) + \pi K_p \left(\tau_m - \frac{r_{T\kappa n} + r_{\kappa n}}{c} - \frac{T_p}{2} \right)^2 \right] \right\}$$

The relationship between $\check{V}_{mn\kappa}$ and $V_{mn\kappa}$ is discussed in Section 4.2.

The coordinates of the test targets in the transmit antenna coordinate system, $(r_{T\kappa n}, \theta_{T\kappa n}, \phi_{T\kappa n})$, and the receive antenna coordinate system, $(r_{\kappa n}, \theta_{\kappa n}, \phi_{\kappa n})$, are calculated exactly as in the case of the scatterers defined to represent the reflectivity of the earth's surface. That is, these coordinates are calculated using Equations (47) to (56). Each target is assumed to be at zero altitude above the WGS 84 ellipsoid, and the longitude and latitude values are inputs to be provided to the simulation.

4.2 Statistical fluctuations

Statistical fluctuations are introduced into the $V_{mn\kappa}$ signal samples prior to the gating and the summation over N_T applied in Equation (82). Each test target can be designated as either Swerling 0, 1, 2, 3, or 4. In the case of a Swerling 0 designation, no statistical fluctuations are added. For the other Swerling designations, the statistical fluctuations are introduced using a filtering process where the filters are calculated using overlapping short-time DFTs.

For a single complex (multiple scattering centres) discrete target, signal fluctuations will occur in slow-time, i.e., across the n index, since the positions of the scattering centres in the transmit and receive antenna coordinate systems will change from pulse to pulse. However, signal fluctuations will not occur in fast-time, i.e., not across the m index, since the speeds of any moving scattering centres are assumed to be much smaller than the propagation speed of the electromagnetic waves transmitted by the SAR. In other words, the scattering centres will remain stationary over the time it takes the radar pulse to illuminate the target (i.e., T_p). Therefore, the filters are calculated using the mean signal samples at a range bin chosen to correspond to the middle of the pulse backscattered by the test target, and at the azimuth position where the test target is closest to the radar. The index of this range bin is given by

$$m_{f\kappa} = \left\lfloor \frac{2 f_s [\min(r_{\kappa n}) - r_N]}{c} \right\rfloor \quad (84)$$

where the subscript f refers to “filter” and the subscript κ denotes a particular test target. The outer operator denoted by $\lfloor \cdot \rfloor$ takes the nearest smaller integer of its argument and the operator \min takes the minimum value of its argument. The range of the first range bin to be sampled by the receiver is denoted by r_N and is provided with the RADARSAT-2 metadata.

The statistical fluctuations must be introduced into the signals while preserving the slow-time correlation of the signals. That is, the change in received signal phase from pulse to pulse must retain information about

the position of the test target if the azimuth compression applied in the SAR image formation process is to provide a coherent sum of the signals backscattered by the test target. The signal samples represented by $V_{mn\kappa}$ will not be stationary for all n . Therefore, the filtering process used to introduce the statistical fluctuations will use a subrange of the signal samples in which the properties of the slow-time signals are considered to remain relatively constant. The length of the subrange is chosen to match the number of slow-time samples for which the test target remains within half of the 3 dB beamwidth, ϕ_3 , of the azimuth antenna gain pattern. This length is calculated as

$$N_f = 2 \left\lceil \frac{1}{\ln 2} \ln \left\{ \left| \frac{r_{m_{f\kappa}} \tan\left(\frac{\phi_3}{2}\right)}{\bar{v}_p T_s} \right| \right\} \right\rceil \quad (85)$$

where \bar{v}_p is the average along-track speed of the satellite platform during the time of transmission of the N_c slow-time pulses. Equation (85) also reduces the number of points in the subrange to the nearest power of 2 in an attempt to speed up the execution of the required DFTs.

The fluctuating signal at $m = m_{f\kappa}$ and for a slow-time region bounded by $n_1 + \frac{N_f}{4} \leq n \leq n_1 + N_f - \frac{N_f}{4} - 1$, where n_1 is some specific value of n , is calculated as

$$\begin{aligned} & \left(\check{V}_{m_{f\kappa}(n_1+N_f/4)\kappa}, \check{V}_{m_{f\kappa}(n_1+N_f/4+1)\kappa}, \dots, \check{V}_{m_{f\kappa}(n_1+N_f-N_f/4-1)\kappa} \right) \\ & = \left(\check{\mathfrak{V}}_{N_f/4}, \check{\mathfrak{V}}_{N_f/4+1}, \dots, \check{\mathfrak{V}}_{N_f-N_f/4-1} \right) \end{aligned} \quad (86)$$

where

$$\check{\mathfrak{V}} = \mathbf{DFT}^{-1} \{ \check{\vec{H}} \} \quad (87)$$

$$\check{H}_i = \sqrt{\check{\mathcal{S}}_i} \exp(j f_{\Phi i}) \quad i = 0, 1, \dots, N_f - 1 \quad (88)$$

$$\check{\mathcal{S}}_i = \mathcal{S}_i f_{Si} \quad (89)$$

$$\mathcal{S}_i = |\mathfrak{X}_i|^2 \quad (90)$$

$$\check{\vec{\mathfrak{X}}} = \mathbf{DFT} \left\{ \left(V_{m_{f\kappa}n_1\kappa}, V_{m_{f\kappa}(n_1+1)\kappa}, \dots, V_{m_{f\kappa}(n_1+N_f-1)\kappa} \right) \right\} \quad (91)$$

The statistical fluctuations are introduced into the signal using the vectors \vec{f}_S and \vec{f}_Φ , which each consist of N_f random numbers. The generation of these random numbers is discussed in Sections 4.2.1, 4.2.2, 4.2.3, and 4.2.4.

The above equations show that only the middle $N_f/2$ outputs of the filtering process are assigned as $V'_{m_{f\kappa}n\kappa}$. Statistical fluctuations for the next $N_f/2$ signal samples, i.e., in the subrange $n_2 + \frac{N_f}{4} \leq n \leq n_2 + N_f - \frac{N_f}{4} - 1$ where $n_2 = n_1 + \frac{N_f}{2}$, are generated using the same process (Equations (86) to (91) with n_1 replaced by n_2). Therefore, the filter used for the subrange defined by n_1 will overlap with the filter used for the subrange defined by n_2 . The region of overlap will be $N_f/4$ samples long. The overlap is used to maintain continuity in the slow-time correlation of the signal samples.

The fluctuating signals at the other relevant range bins (i.e., within the fast-time gate) are calculated as

$$\check{V}_{mn\kappa} = |\check{V}_{m_{f\kappa}n\kappa}| \exp \left[j \tan^{-1} \left(\frac{\text{Im}\{V_{mn\kappa}\}}{\text{Re}\{V_{mn\kappa}\}} \right) \right] \quad (92)$$

where **Re** and **Im** take the real and imaginary part of its complex argument, respectively. This extends the statistical fluctuation to the amplitude of the entire transmitted pulse while maintaining the phase of the transmitted waveform across fast-time.

4.2.1 Swerling 1 model

The Swerling 1 model describes a target whose received signal voltage fluctuates slowly according to a Rayleigh probability density function. This model can be used to describe a target with many scattering centres of equal radar cross section. The relative positions of these scattering centres with respect to the radar do not change significantly over the time period of the pulse repetition interval, but do change significantly over a longer slow-time period. To be easily compatible with the approach discussed in Section 4.2, the length of this slow-time period is chosen to be the time for which the target remains within an aspect defined by a quarter of the 3 dB beamwidth of the azimuth antenna gain pattern. The overlapping filtering process described in Section 4.2 dictates that the time scale of Swerling 1 fluctuation is chosen to be $(T_s N_f)/2$.

In the Swerling 1 case only one random number is required for each filter applied in Equation (89). That is, $f_{si} = f_s = \text{constant}$ for all $i = 0, 1, \dots, N_f - 1$. This value is calculated as

$$f_s = f_I^2 + f_Q^2 \quad (93)$$

where

$$\begin{aligned} f_I &= (f^2 + f'^2)^{\frac{1}{2}} \cos \left[\tan^{-1} \left(\frac{f'''}{f''} \right) \right] = f'' \left(\frac{f^2 + f'^2}{f''^2 + f'''^2} \right)^{\frac{1}{2}} \\ f_Q &= (f^2 + f'^2)^{\frac{1}{2}} \sin \left[\tan^{-1} \left(\frac{f'''}{f''} \right) \right] = f''' \left(\frac{f^2 + f'^2}{f''^2 + f'''^2} \right)^{\frac{1}{2}} \end{aligned} \quad (94)$$

and

$$\begin{aligned}
 f &= \frac{\mathbb{x}}{\sqrt{2}} \\
 f' &= \frac{\mathbb{x}'}{\sqrt{2}} \\
 f'' &= \frac{\mathbb{x}''}{\sqrt{2}} \\
 f''' &= \frac{\mathbb{x}'''}{\sqrt{2}}
 \end{aligned} \tag{95}$$

The \mathbb{x} , \mathbb{x}' , \mathbb{x}'' , \mathbb{x}''' are Gaussian distributed random numbers having a mean of zero and a standard deviation of one. Consequently, the f_I and f_Q calculated in Equation (94) will be zero-mean Gaussian random numbers having a standard deviation of $1/\sqrt{2}$. The approach used in Equation (94) ensures that f_I and f_Q are in phase quadrature. While this is not relevant for the Swerling 1 model, this form is used for all Swerling models and phase quadrature of the fluctuations is required for the Swerling 2 and 4 models. The resulting random number, f_S , will correspond to an exponential probability density function having a mean of one. A mean value of one ensures that the filtering applied in Equation (89) does not alter the magnitude of the signal.

In the Swerling 1 case, the phase spectrum values, $f_{\Phi i}$, required in Equation (88) are not random numbers. Instead, these values are dictated by the non-fluctuating signal, i.e.,

$$f_{\Phi i} = \tan^{-1} \left(\frac{\text{Im}\{\mathbb{x}_i\}}{\text{Re}\{\mathbb{x}_i\}} \right) \tag{96}$$

4.2.2 Swerling 2 model

The Swerling 2 model describes a target whose received signal voltage fluctuates from pulse to pulse (slow-time) according to a Rayleigh probability density function. This model is used to describe a target with many scattering centres of equal backscatter cross section. The relative positions of the scattering centres with respect to the radar antenna will change significantly over the time period of the pulse repetition interval. For the Swerling 2 case, these random numbers are generated as

$$f_{Si} = |f_{\mathbb{x}i}|^2 \quad f_{\Phi i} = \tan^{-1} \left(\frac{\text{Im}\{f_{\mathbb{x}i}\}}{\text{Re}\{f_{\mathbb{x}i}\}} \right) \tag{97}$$

where

$$\vec{f}_{\mathbb{x}} = \text{DFT}\{\vec{f}_I + j \vec{f}_Q\} \tag{98}$$

and

$$f_{Ii} = (f_i^2 + f_i'^2)^{\frac{1}{2}} \cos \left[\tan^{-1} \left(\frac{f_i'''}{f_i''} \right) \right] = f_i'' \left(\frac{f_i^2 + f_i'^2}{f_i''^2 + f_i'''^2} \right)^{\frac{1}{2}}$$

$$f_{Qi} = (f_i^2 + f_i'^2)^{\frac{1}{2}} \sin \left[\tan^{-1} \left(\frac{f_i'''}{f_i''} \right) \right] = f_i''' \left(\frac{f_i^2 + f_i'^2}{f_i''^2 + f_i'''^2} \right)^{\frac{1}{2}}$$
(99)

and

$$f_i = \mathbb{X}_i \sqrt{\frac{N_f}{2}}$$

$$f_i' = \mathbb{X}_i' \sqrt{\frac{N_f}{2}}$$

$$f_i'' = \mathbb{X}_i'' \sqrt{\frac{N_f}{2}}$$

$$f_i''' = \mathbb{X}_i''' \sqrt{\frac{N_f}{2}}$$
(100)

The $\mathbb{X}_i, \mathbb{X}_i', \mathbb{X}_i'', \mathbb{X}_i'''$ are Gaussian distributed random numbers having a mean of zero and a standard deviation of one. The f_{Ii} and f_{Qi} calculated in Equation (99) will be zero-mean Gaussian random numbers having a standard deviation of $\sqrt{N_f/2}$ and will be in phase quadrature. The power spectrum fluctuations, f_{Si} , will be exponentially distributed random numbers, and they will have a mean of one if the normalization of the DFT is defined as in Equation (62).

The phase spectrum fluctuations, $f_{\Phi i}$, will be random numbers uniformly distributed between $-\pi$ and π , i.e.,

$$f_{\Phi i} = 2\pi \mathbb{U}_i - \pi$$
(101)

where the \mathbb{U}_i are random numbers uniformly distributed between zero and one.

4.2.3 Swerling 3 model

The Swerling 3 model describes a target whose received signal voltage fluctuates slowly according to a “chi-square” distribution of degree 4 (see [18], p. 167). This model can be used to describe a target that consists of one dominant scattering centre and many other scattering centres of smaller radar cross section. The relative positions of these scattering centres with respect to the radar do not change significantly over the time period of the pulse repetition interval, but do change significantly over a longer slow-time period. The time period of Swerling 3 fluctuation is chosen to be the same as that chosen for Swerling 1 fluctuation, i.e., $(T_s N_f)/2$.

In this case, the power spectrum fluctuation required for each filter is calculated as

$$f_{Si} = f_S \forall i \quad \text{and} \quad f_S = \frac{1}{4}(\mathbb{x}^2 + \mathbb{x}'^2 + \mathbb{x}''^2 + \mathbb{x}'''^2) \quad (102)$$

where the \mathbb{x} , \mathbb{x}' , \mathbb{x}'' , \mathbb{x}''' are Gaussian distributed random numbers having a mean of zero and a standard deviation of one. The resulting f_S are degree 4 chi-square distributed random numbers having a mean of one.

Similar to the Swerling 1 case, the $f_{\Phi i}$ required in Equation (88) for the Swerling 3 case are calculated using Equation (96).

4.2.4 Swerling 4 model

The Swerling 4 model describes a target whose received signal voltage fluctuates rapidly from pulse to pulse according to a chi-square distribution of degree 4. As in the case of the Swerling 3 target, this model can be used to describe a target that consists of one dominant scattering centre and many other scattering centres of smaller radar cross section. However, in this case, the relative positions of the scattering centres with respect to the radar do change significantly over the time period of the pulse repetition interval.

The power spectrum fluctuations required for each filter are calculated as

$$f_{Si} = \frac{1}{4}(\mathbb{x}_i^2 + \mathbb{x}_i'^2 + \mathbb{x}_i''^2 + \mathbb{x}_i'''^2) \quad (103)$$

where the \mathbb{x}_i , \mathbb{x}_i' , \mathbb{x}_i'' , \mathbb{x}_i''' are Gaussian distributed random numbers having a mean of zero and a standard deviation of one. The resulting f_{Si} are degree 4 chi-square distributed random numbers having a mean of one.

The phase spectrum fluctuations are calculated using Equation (101).

5 Receiver system noise

In-phase and quadrature signal samples corresponding to receiver system noise are calculated for all range bins and all azimuth positions. These noise components will have Gaussian probability density functions. Therefore, the noise contributions to the I and Q signal samples can be calculated as [25]

$$\begin{aligned} I_{mn} &= \sigma_{Nm} \sqrt{\mathbb{x}_{mn}^2 + \mathbb{x}'_{mn}{}^2} \cos(2\pi \mathbb{u}_{mn} - \pi) \\ Q_{mn} &= \sigma_{Nm} \sqrt{\mathbb{x}_{mn}^2 + \mathbb{x}'_{mn}{}^2} \sin(2\pi \mathbb{u}_{mn} - \pi) \end{aligned} \quad (104)$$

where the subscripts m and n are the same as in previous sections, i.e., indexes for the M range bins and N_c transmitted pulses. The \mathbb{x}_{mn} and \mathbb{x}'_{mn} are Gaussian distributed random numbers with a mean of zero and a standard deviation of 1. The \mathbb{u}_{mn} are uniformly distributed random numbers between 0 and 1. Consequently, the I_{mn} and Q_{mn} have the statistical properties of thermal noise, i.e., they are Gaussian distributed random numbers having a mean of zero and a variance of σ_{Nm}^2 . The random numbers $I_{mn}^2 + Q_{mn}^2$ will conform to an exponential distribution and will have a mean of $2\sigma_{Nm}^2$.

RADARSAT-2 image products include noise-equivalent β^o values as a function of range (pixel value). These values can be used to calculate mean noise power values, \bar{P}_{Nm} , in exactly the same manner as the radar brightness (observed reflectivity) values corresponding to the RADARSAT-2 product image data are used to calculate the mean power level used to scale the MODEX data (see Section 3.3, Equation (73)). Using Equation (28), the mean noise power is related to the mean noise component values as

$$\bar{P}_{Nm} = \frac{\bar{I}_m^2 + \bar{Q}_m^2}{2Z} \quad (105)$$

Therefore, the standard deviation of the noise components can be calculated as

$$\sigma_{Nm} = \sqrt{\bar{P}_{Nm} Z} \quad (106)$$

The subscript m is retained on σ_{Nm} in Equation (104) since the \bar{P}_{Nm} values calculated using Equation (73) will not be the same for each range bin due to the range dependence of the noise-equivalent β^o values.

Alternatively, a single mean noise power value can be estimated from radar system parameters as (see [11], page 34)

$$\bar{P}_N = k_b T_o B_N F_N G_s \quad (107)$$

where k_b is the Boltzmann constant (1.38×10^{-23} J/K), T_o is a reference temperature (290 K), B_N is the noise bandwidth of the receiver, and F_N is the noise figure corresponding to the receiver. In this case the standard deviation used in Equation (104) is given by

$$\sigma_{Nm} = \sqrt{\bar{P}_N Z} \quad \forall \quad m \quad (108)$$

6 Analogue to digital conversion

The simulation implements the calculations of the I_{mn} and Q_{mn} described in Sections 3, 4, and 5 using double-precision floating-point numbers. These values can then be converted to binary numbers to simulate the process of analogue-to-digital conversion.

The first step of the analogue-to-digital conversion is to assign the range of the Analogue to Digital Converter (ADC) to a range of voltage values. This is done by matching a chosen ADC output value to the mean noise level. A vector of bits, \vec{b}_n , that will correspond to the mean noise level is defined as an input. For example, if $\vec{b}_n = [0,1]$, then an input signal having a power equivalent to the mean noise level will cause the output ADC value to have bits 0 and 1 set to 1. Given this definition, the voltage increment between ADC values is

$$\Delta V = \frac{\sqrt{2 \bar{P}_N Z}}{\left(\sum_{i=0}^{n_b-1} 2^{b_{ni}} \right)} \quad (109)$$

where n_b is the number of bits in the ADC, and \bar{P}_n is the mean noise power given by either Equation (105) or (107). Assuming a sign bit, the minimum and maximum voltage values corresponding to the ADC are then given by

$$\begin{aligned} V_{min} &= -2^{n_b-1} \Delta V \\ V_{max} &= 2^{n_b-1} \Delta V \end{aligned} \quad (110)$$

The output of the ADC can now be represented as

$$I_{mn} \rightarrow \begin{cases} 0 & \text{for } I_{mn} \leq V_{min} \\ \left\lfloor \frac{2^{n_b}(I_{mn} - V_{min})}{V_{max} - V_{min}} + 0.5 \right\rfloor & \text{for } V_{min} \leq I_{mn} < V_{max} \\ 2^{n_b} - 1 & \text{for } I_{mn} \geq V_{max} \end{cases} \quad (111)$$

$$Q_{mn} \rightarrow \begin{cases} 0 & \text{for } Q_{mn} \leq V_{min} \\ \left\lfloor \frac{2^{n_b}(Q_{mn} - V_{min})}{V_{max} - V_{min}} + 0.5 \right\rfloor & \text{for } V_{min} \leq Q_{mn} < V_{max} \\ 2^{n_b} - 1 & \text{for } Q_{mn} \geq V_{max} \end{cases} \quad (112)$$

where the operator $\lfloor \cdot \rfloor$ converts its argument to the nearest integer that is smaller than the argument.

7 Evaluation of simulated signals

The simulated signals are evaluated by comparing their properties with theoretical expectations and with the properties of real signal data (RADARSAT-2 MODEX 1 mode). In addition, the image data formed by processing the simulated signals with the Range-Doppler Algorithm (RDA) is compared with the image data created by processing the MODEX data, and with actual image data provided with the RADARSAT-2 data sets.

7.1 Test target

To examine the properties of the test target signals a simulation run was performed without clutter (signals reflected from the surface of the earth), receiver system noise, and analogue-to-digital conversion. For this test, the simulated SAR is operated in the MODEX 1 mode. That is, all parameters associated with the simulation run correspond to a particular MODEX 1 mode data collection that occurred over the Vancouver area starting at 14:21 Z on July 24, 2008. The overarching filename associated with this data set is “PDS_0018286_20080724.”

The test target parameters are shown in Table 1. The vast majority of the parameters used by the simulation are read from the RADARSAT-2 metadata, such as reference noise level, orbit, spacecraft attitude, image generation, image attribute, and radiometric parameters. The remaining parameters that are required by the simulation and that must be specified by the user are listed in Table 2, 3, and 4. For reference, Table 3 also contains some of the main SAR parameters that are supplied with the RADARSAT-2 metadata.

Table 1: Test target parameters.

Description	Value
Longitude	123.181344°W
Latitude	49.196714°N
RCS	200 m ²
Swerling number	0

Table 2: Control parameters for test target and MODEX 1 mode simulations.

Description	Value
Range resolution factor used in scaling calculations	23
Azimuth resolution factor used in scaling calculations	3
Range resolution factor for surface scatterer spacing (N_{Pr})	1
Azimuth resolution factor for surface scatterer spacing ($N_{P\phi}$)	1
Range tolerance for determining convergence of Earth intersection point algorithm	0.01 m

Table 3: SAR parameters for test target and MODEX 1 mode simulations.

Description	Symbol	Value
-------------	--------	-------

Sampling frequency	f_s	56.30 MHz
Transmitted frequency	f_c	5.405 GHz
Pulse length	T_p	20.80 μ s
Frequency modulation rate	K_p	2.405×10^{12} cycles s^{-2}
Pulse repetition interval	T_s	0.4045 ms
Transmit antenna gain on boresight	G_t	49.23 dB
Receive antenna gain on boresight	G_r	46.22 dB
1-way polar angle 3 dB beamwidth	θ_3	2.22°
1-way azimuth angle 3 dB transmit beamwidth	ϕ_{T3}	0.203°
1-way azimuth angle 3 dB receive beamwidth	ϕ_{r3}	0.405°
Azimuth beam axis angle	ϕ_b	0.0°
Transmit power [26]	P_t	5.12 kW
Input impedance of antenna port	Z	50 Ω
System Losses	L_s	3.4 dB
Number of bits used in analogue to digital conversion	n_b	8
Polarization		HH
Receiver system gain	G_s	0.0 dB
Bits associated with mean receiver noise level	\vec{b}_n	[0]
Antenna length [26]	L_A	15 m
Antenna width [26]	W_A	1.37 m
y_T -axis position of receive phase centre	Δy	3.75 m

The control parameters listed in Table 2 relate to resolution specifications for calculating signals from the surface of the earth. The range and azimuth resolution factors for scaling calculations are used to define the quantities Δr and Δa_ϕ , respectively, used in Section 3.3. That is, these quantities are determined as the range and azimuth image pixel size divided by the corresponding resolution factor. The range and azimuth resolution factors for surface scatterer spacing are used to define the number of scatterers used to represent the surface reflectivity field, again as a function of the image pixel sizes (see Section 3.2.1). For example, values of 1 and 1, as shown in Table 2 indicate that there is one scatterer per image pixel. This is the minimum amount allowed, but in this case would still result in 153,403,882 ($N_{I\phi} \times 1 \times N_{Ir} \times 1$) scatterers being used to represent the surface reflectivity field, if these calculations were included.

Table 4: Image formation processing parameters for test target and MODEX 1 mode simulations.

Description	Symbol	Value
-------------	--------	-------

Kaiser window shape parameter used in sinc interpolation	β_K	2.5
Number of interpolates used in sinc interpolation	N_i	16
Minimum acceptable azimuth oversampling ratio	$\alpha_{a\ell}$	1.3
Maximum acceptable azimuth oversampling ratio	α_{au}	1.4

The first five parameters listed in Table 3 are taken from the RADARSAT-2 metadata. As discussed in Section 3.2, the normalized antenna gain patterns are assumed to have $\sin x/x$ form for the MODEX 1 mode. The boresight transmit antenna gain is calculated as

$$G_t = \frac{4\pi L_A W_A}{\lambda_c^2} \quad (113)$$

where L_A and W_A are the length and width of the active aperture, respectively. In MODEX 1 mode only half of the full aperture is used for receive. Therefore, the boresight receive antenna gain is calculated as

$$G_r = \frac{4\pi L_A W_A}{2 \lambda_c^2} \quad (114)$$

The antenna beamwidths were derived from beam pattern data supplied with the MODEX data set. The system loss value used was provided by MDA as a sum of transmit power reduction losses (2.2 dB) and subarray losses (1.2 dB).

An image of the real part of the test target signal samples, i.e., I_T in Equation (1), is shown in Figure 8. The non-zero data have limited extent in slant range equal to the pulse length and exhibit curvature due to range walk, as expected.

The signal data along a fast-time cut through the region of peak amplitude, and corresponding to pulse number 13884, are shown in Figure 9. Here it can be seen that the in-phase and quadrature data are an echo of the transmitted pulse. The extent of non-zero data matches the pulse length and the location of stationary phase is in the centre of the received signal. The amplitude of the received signal is constant. The unwrapped phase exhibits a quadratic dependence on fast-time. The signal frequency is calculated as the derivative of the unwrapped signal phase, with respect to fast-time, divided by 2π . It can be seen that the signal frequency increases on a linear ramp throughout the received signal. The minimum signal frequency corresponds to $-K_p T_p/2$, which is half of the pulse bandwidth, and the maximum signal frequency corresponds to $+K_p T_p/2$. All of these properties agree with the theoretical expectations dictated by the equations in Section 4.1.

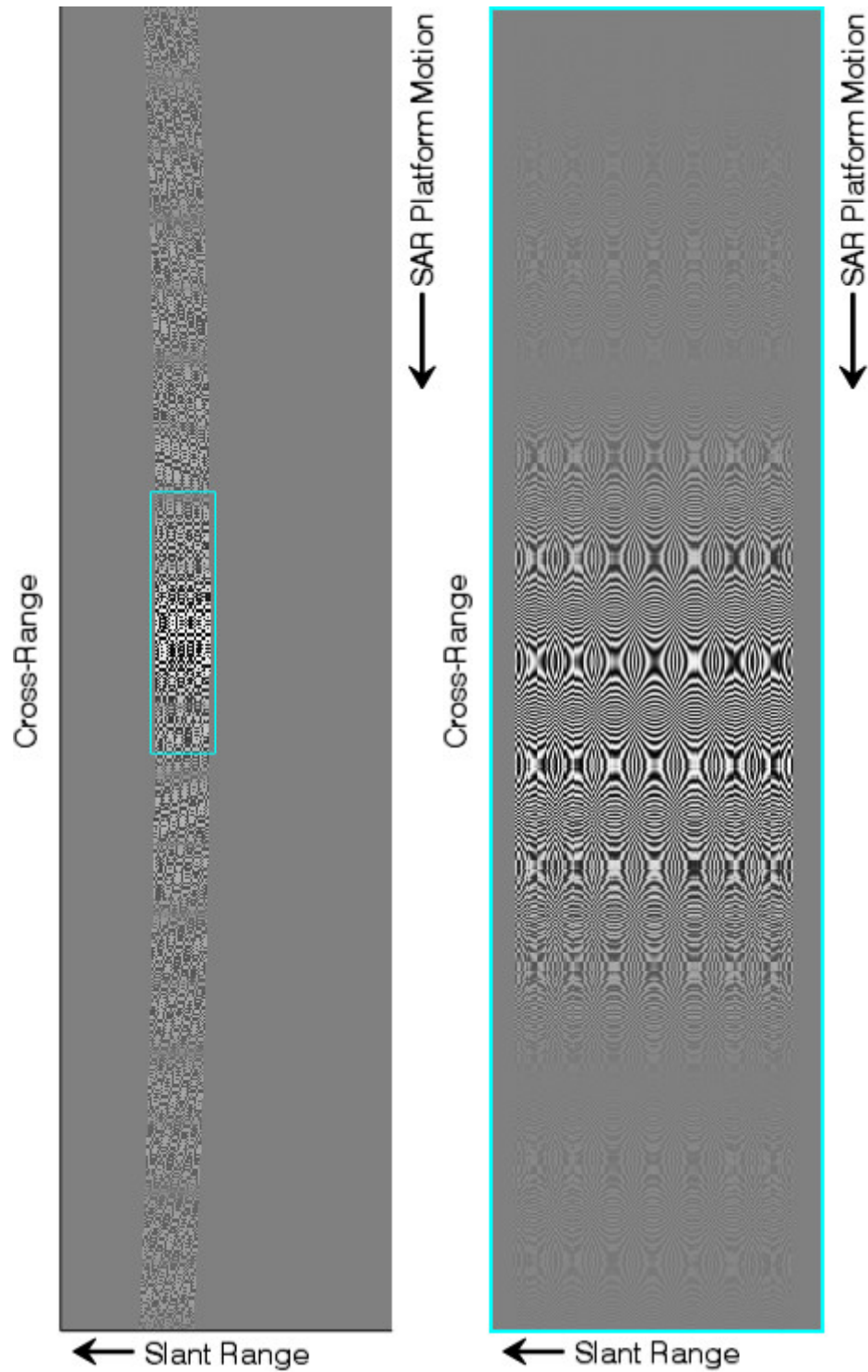


Figure 8: Left: Image of in-phase signal samples corresponding to a single test target. A non-linear grey scale has been applied to the data to enhance contrast. Right: A blow-up of the portion of the left image in the region of peak magnitude (cyan box). A linear grey scale is used.

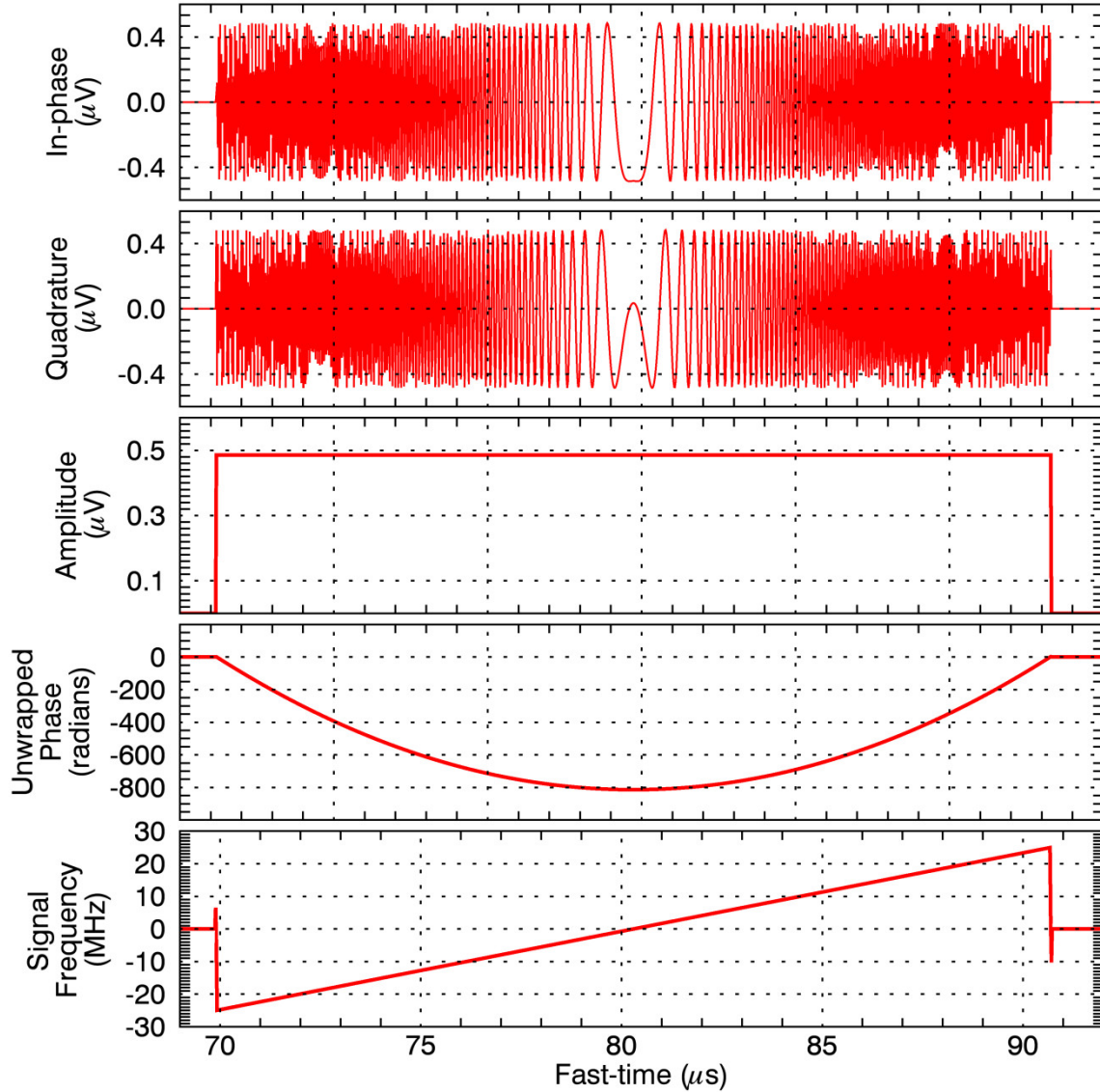


Figure 9: Signal properties as a function of fast-time for pulse number 13884.

Figure 10 shows the signal data along a slow-time cut corresponding to range bin number 4520. Here it can be seen that the magnitude of the in-phase and quadrature data, and the signal amplitude trace out the shape of the azimuth beam pattern. The unwrapped signal phase shows the approximately quadratic dependence caused by the range-walk associated with the stationary target as the SAR platform moves past. Aliasing occurs in this plot because the algorithm used to unwrap the signal phase can only interpret pulse-to-pulse phase differences between $-\pi$ and π . Since the SAR receiver also can only measure pulse-to-pulse phase differences between $-\pi$ and π this plot shows how aliasing affects the received signal data. The aliasing is also evident in the azimuth signal frequency data, which is calculated as the derivative of the unwrapped phase with respect to slow-time divided by 2π . The minimum azimuth signal frequency corresponds to $-1/(2 T_s)$, which is half of the Pulse Repetition Frequency (PRF), and the maximum azimuth signal frequency corresponds to $+1/(2 T_s)$. Again, the displayed properties agree with the theoretical expectations dictated by the equations in Section 4.1.

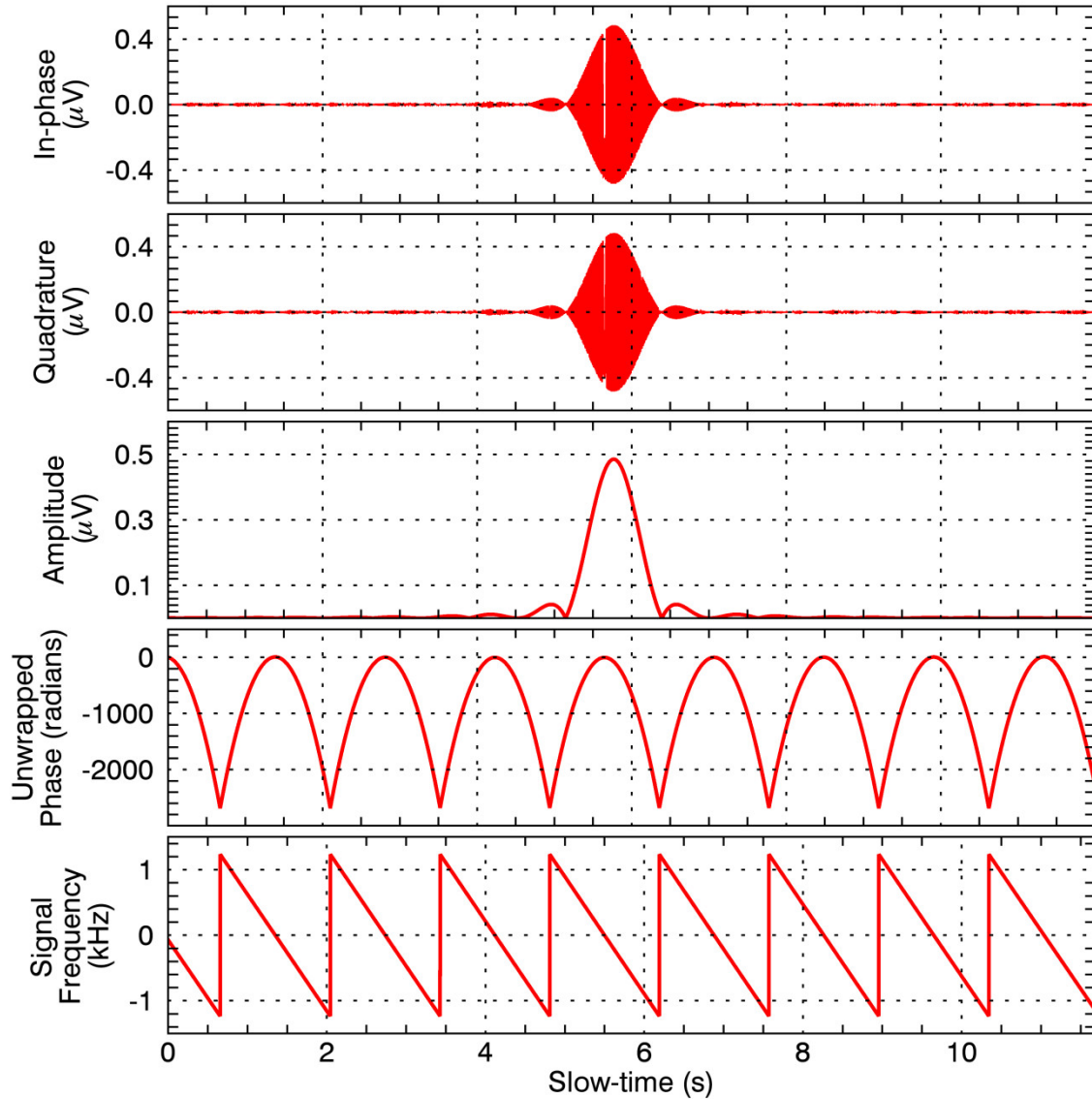


Figure 10: Signal properties as a function of slow-time for range bin number 4520.

The test target data shown above were processed into an image using the RDA (Annex B). The resulting image is shown in Figure 11. The curvature in the data, due to range walk, is again evident. The data also show seven additional weaker targets that are aliased versions of the actual target. The region within the cyan box is expanded in Figure 12 to show a better view of the target signature. The test targets used in this simulation are point targets or spatial impulses. Therefore, the SAR image corresponding to a test target displays the impulse response of the simulated SAR system.

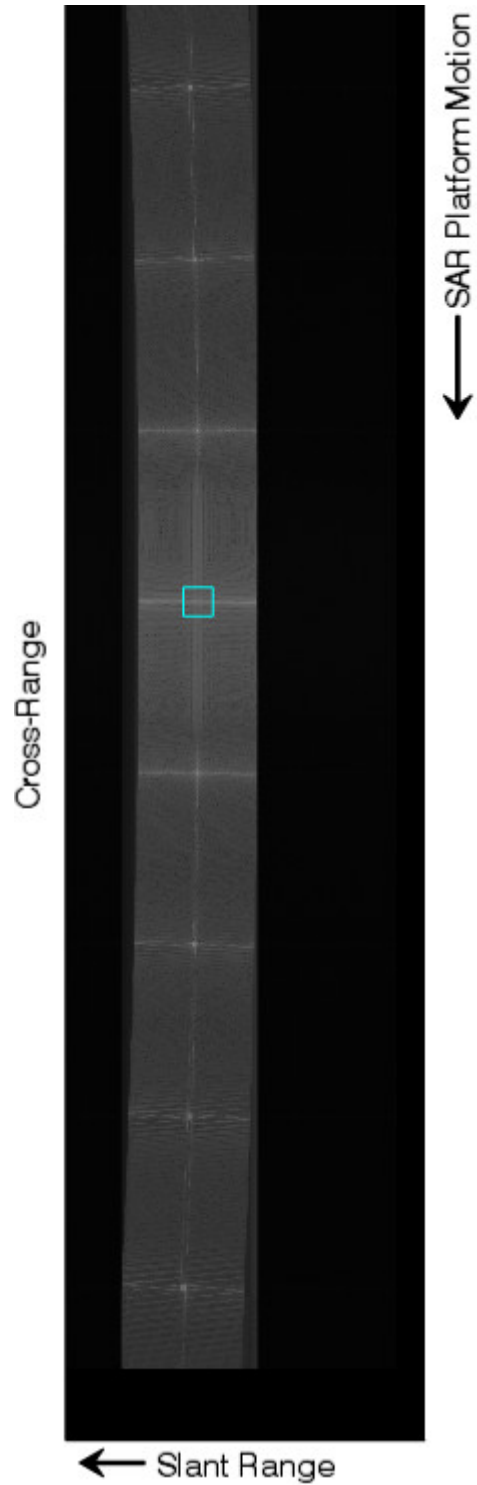


Figure 11: SAR Image of the simulated test target data. A non-linear colour scale is used to enhance contrast. The cyan box shows the region containing the peak image pixel value and denotes the region displayed in Figure 12.

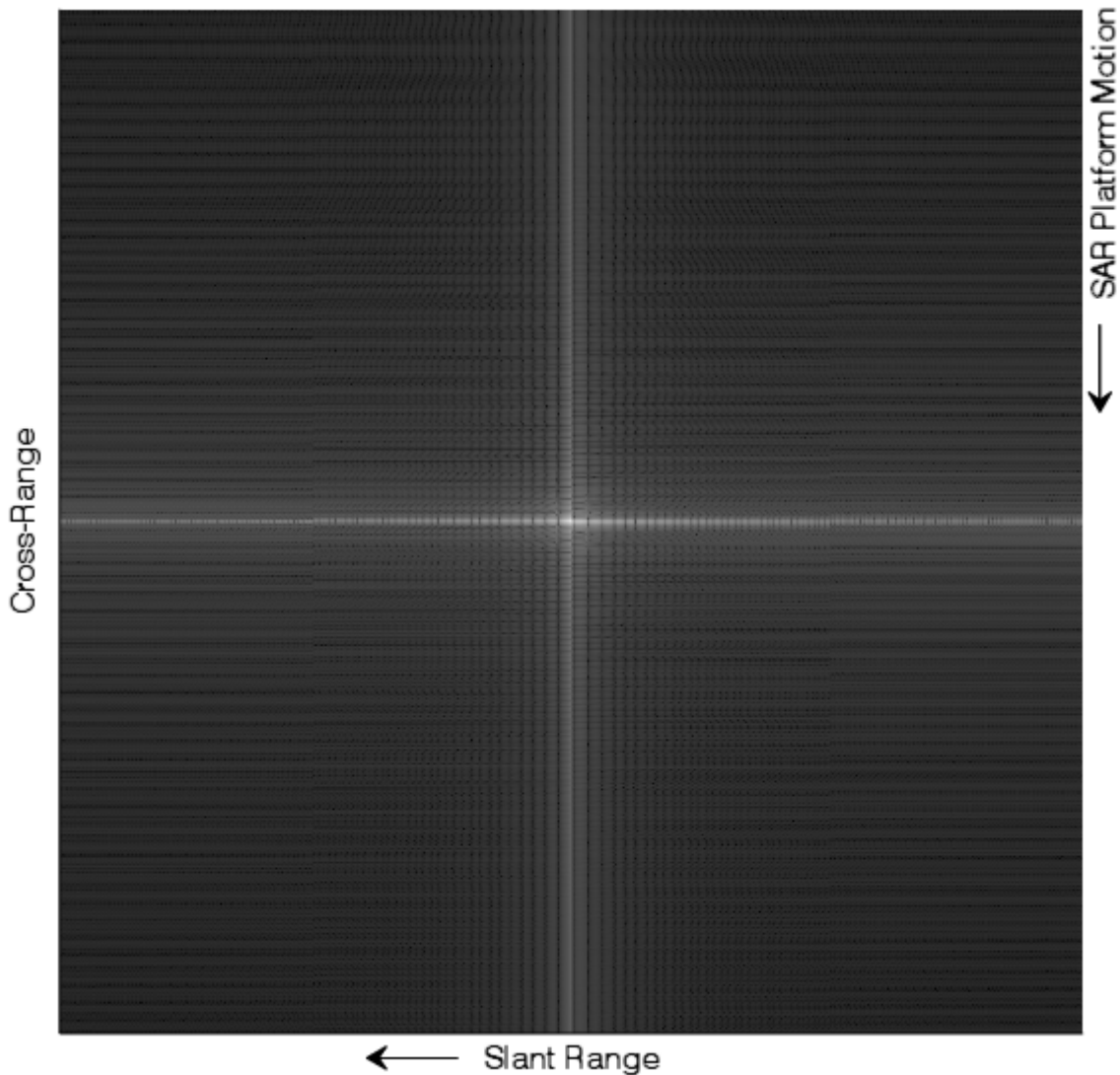


Figure 12: Zoomed in view of SAR image in the region of the test target signature (cyan box of Figure 11).

Slant-range (image pixel) and cross-range (image line) cuts through the image data at the pixel and line location of the peak image amplitude are shown in Figure 13. Note that while the peak received amplitude of the test target signal occurred for pulse 13884, the peak amplitude of the target signature occurs at line 12181 of the SAR image due to azimuth registration associated with the azimuth compression process, and image geolocation. The image pixel cut shows the output response function corresponding to the SAR pulse compression. The image line cut again shows the aliasing of the target in azimuth.

Finally, a zoomed in surface view of the image power is shown in Figure 14. Here the side lobes associated with the image processing can be seen.

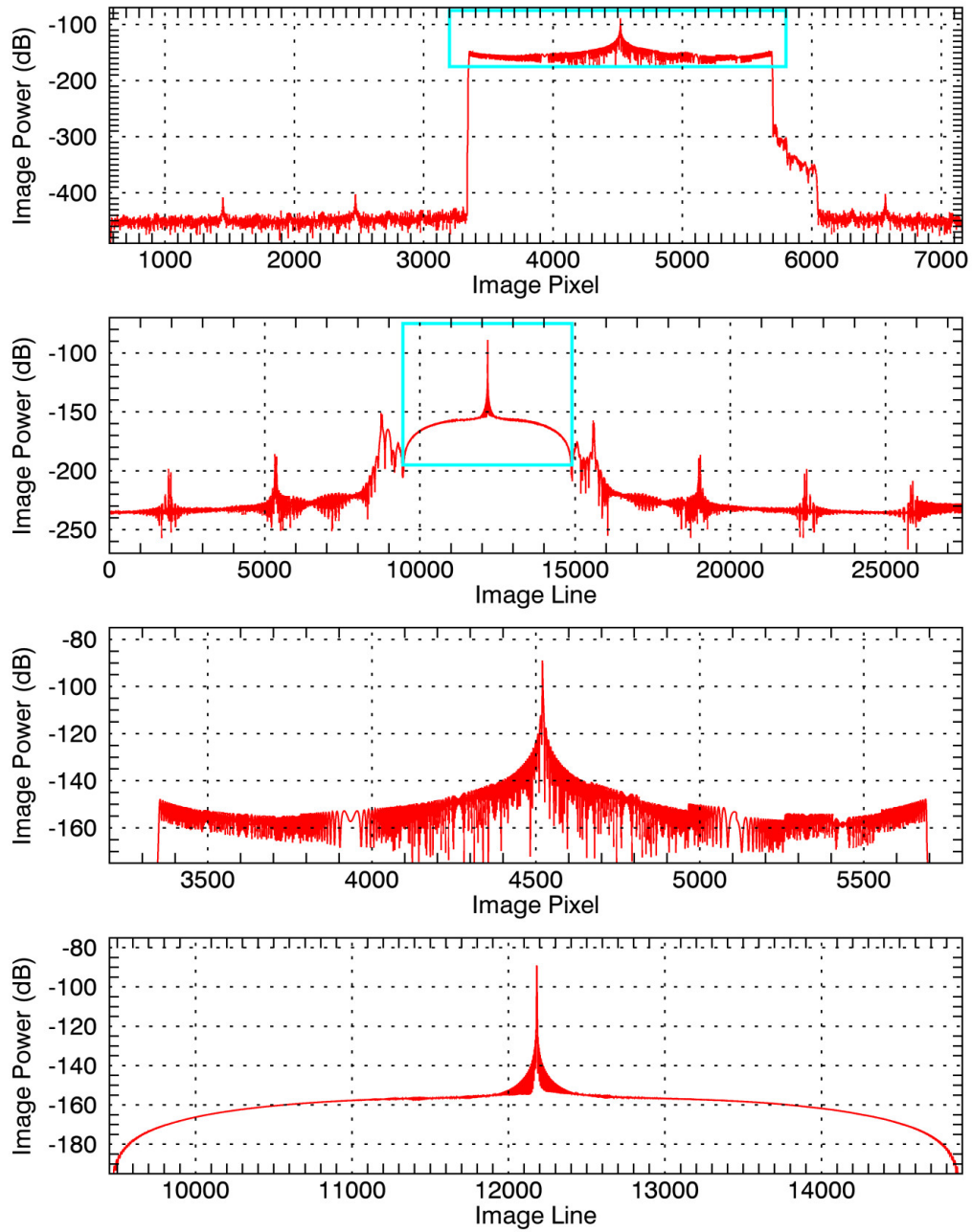


Figure 13: Image pixel (slant-range) and image line (cross-range) cuts through the test target image data. The upper two plots show all of the data. The lower two plots are zoomed regions corresponding to the cyan boxes in the upper plots.

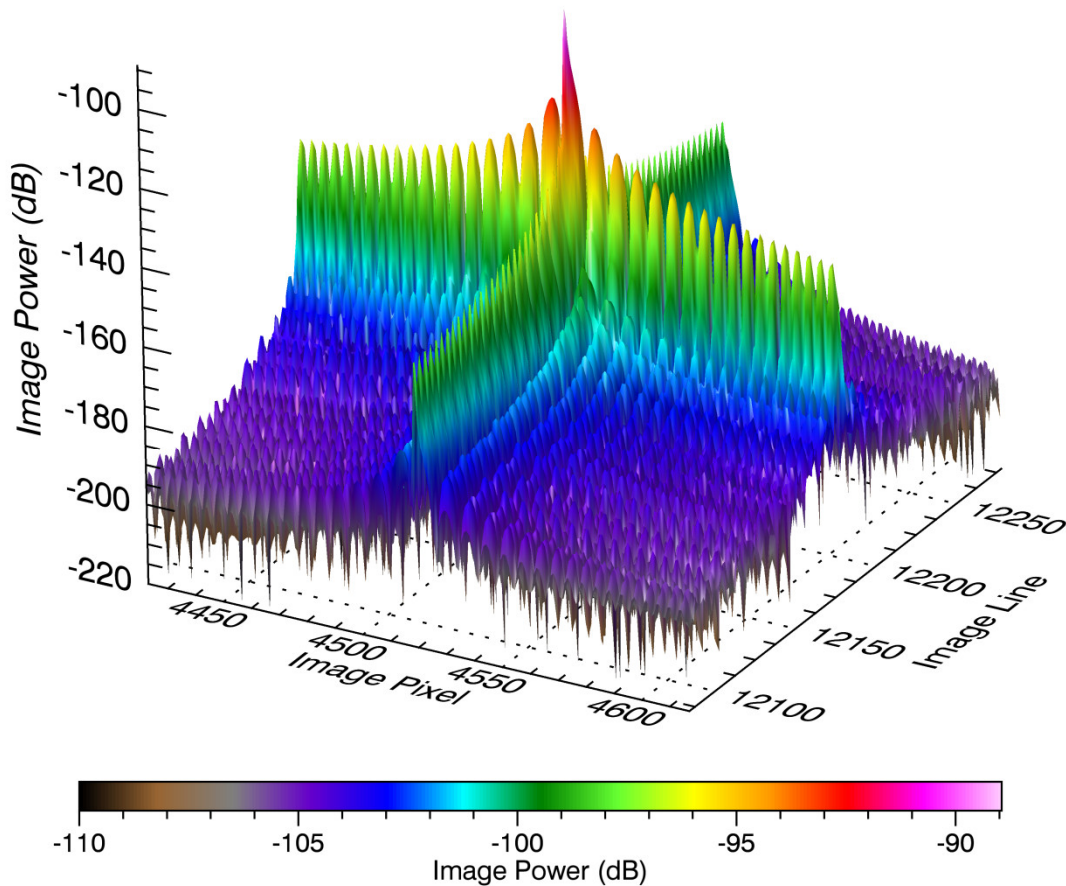


Figure 14: Zoomed in surface view of the test target image signature.

7.2 Earth surface

This section evaluates the properties of the simulated received signals corresponding to reflection from the surface of the earth, i.e., the clutter signals.

7.2.1 Case 1: MODEX 1 mode

The data generated for this case correspond to the same case discussed in Section 7.1. That is, the overarching filename is “PDS_0018286_20080724” and all of the associated parameters are listed in Tables 1, Table 2, 3, and 4. The test target specified in Table 1 is included in the simulation, but receiver system noise and analogue-to-digital conversion are not included. The signals that are compared are generated in two ways: (1) real MODEX 1 data are read from the RADARSAT-2 MODEX 1 data file, scaled (see Section 3.3 and the brown boxes of Figure 1), and processed into an image, and (2) the full simulation is used to generate simulated signals from an inputted reflectivity field defined by the real RADARSAT-2 image data (See Section 3.2 and the orange boxes of Figure 1), and then these simulated signals are processed into an image. The simulated test target data are only added to the fully simulated data, not to the real, MODEX 1, scaled, data.

7.2.1.1 Comparison of unprocessed data

The simulated in-phase signal samples at all range bins for an example pulse (13884) are compared against those derived from real MODEX 1 data in Figure 15. The real MODEX 1 data are provided in the form of range-compressed signal samples. These data are decompressed and scaled. In addition, for comparison purposes the decompressed data shown in Figure 15 (blue) are correctly registered in range. This registration is not performed in the actual simulation since it will be accounted for when the range-compression processing occurs. The real and simulated data are seen to have a similar magnitude and character. For pulse number 13884, the radar beam passes through the Vancouver airport. The greater reflectivity corresponding to the airport structures create the larger magnitudes seen at range bins 3600 to 5000. The two curves are not exactly the same, as is expected, since they are different realizations of a random process.

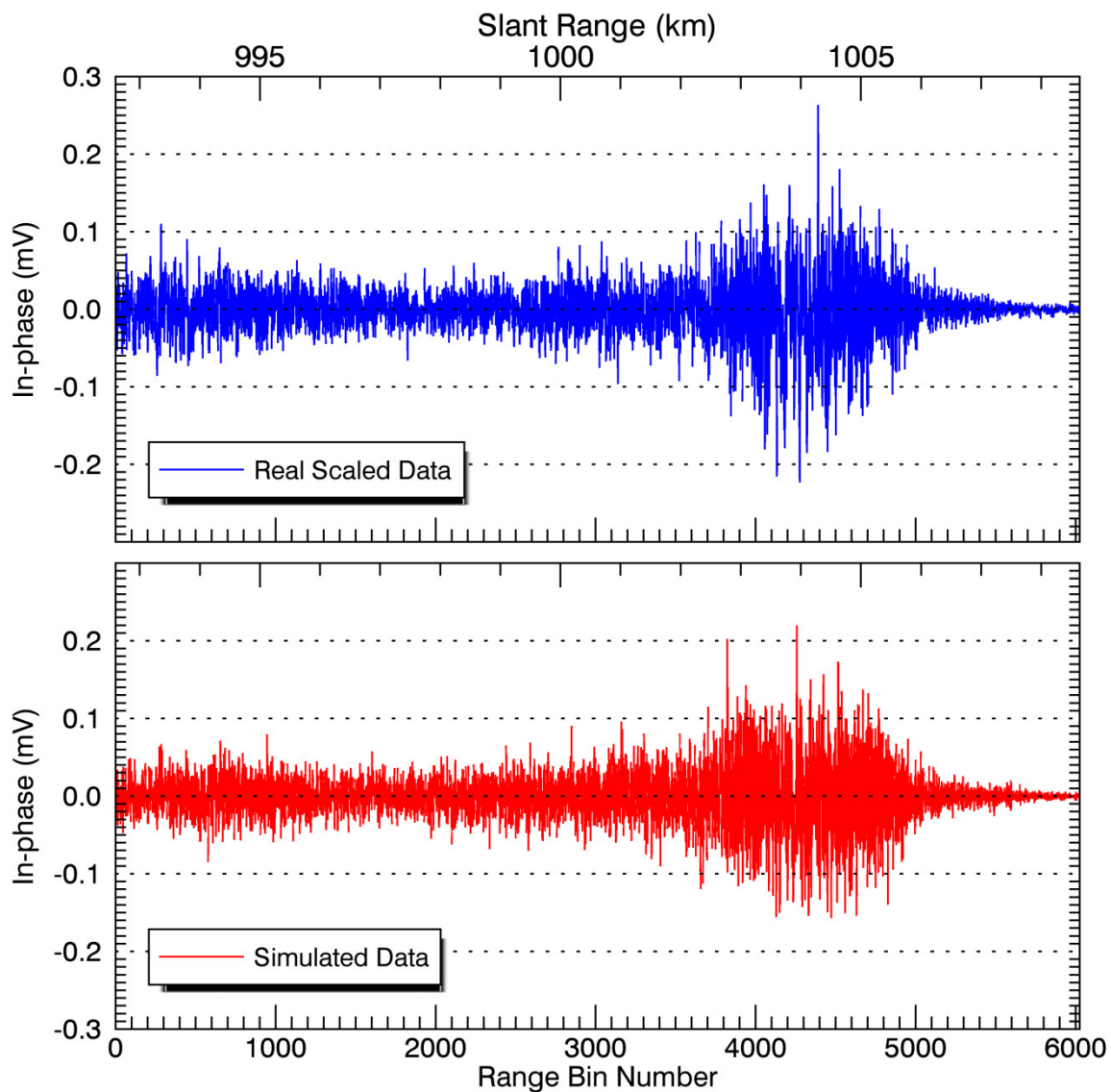


Figure 15: Unprocessed in-phase data for pulse number 13884.

The received powers (i.e., $I^2 + Q^2$) corresponding to the signals shown in Figure 15 are displayed in Figure 16. These data also show a similar magnitude and character.

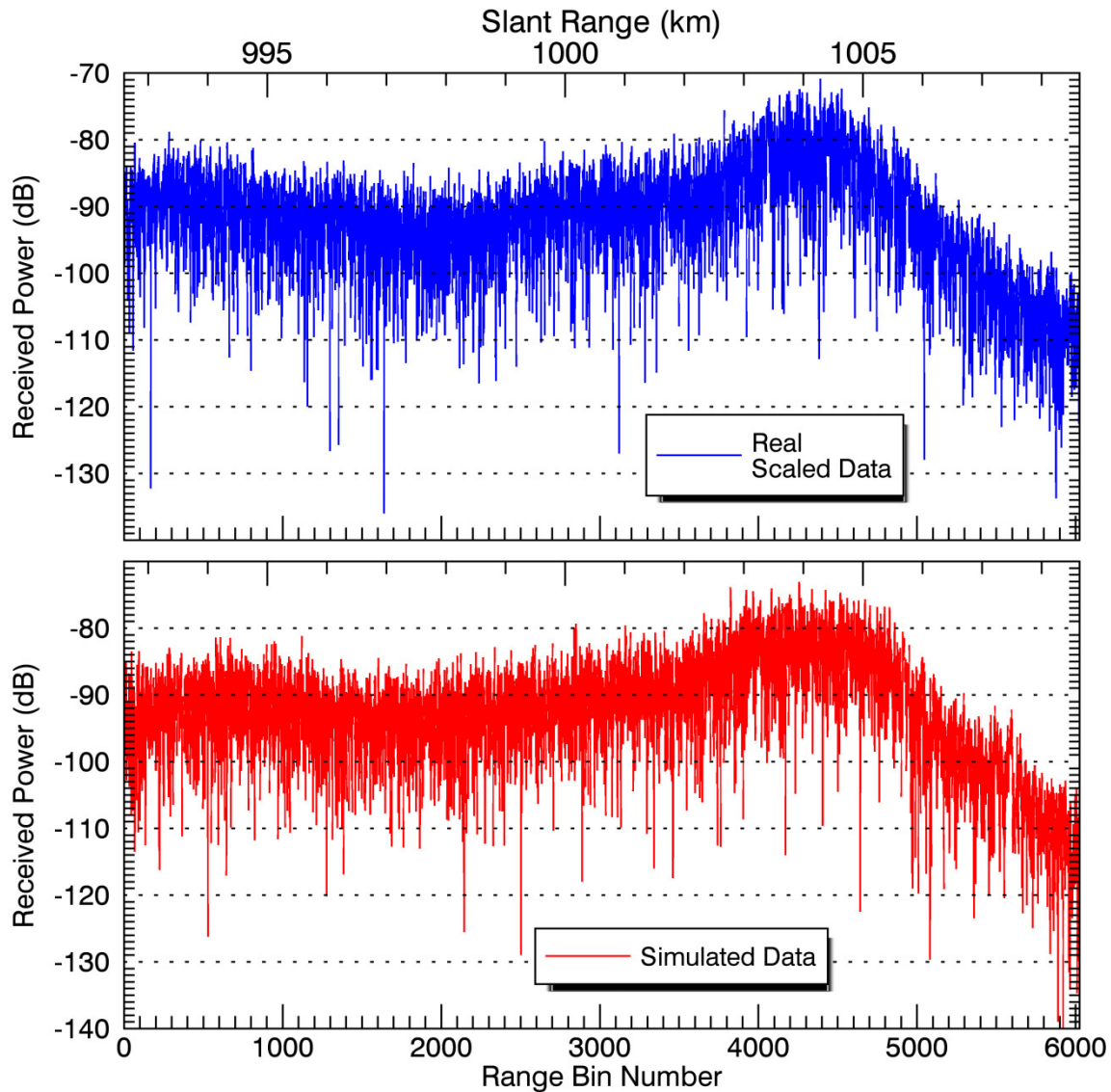


Figure 16: Unprocessed received signal power for pulse number 13884.

7.2.1.2 Comparison of range-compressed data

The signal power data after range-compression are compared for the example pulse number 13884 in Figure 17. The green curve shows the raw range-compressed data that are read directly from the MODEX 1 data file. These data have not been altered in any way, i.e., no range-decompression and no scaling. The blue curve shows the data after undergoing range-decompression, scaling, and range-compression. The red curve shows the simulated data, which includes the test target signals. There are no simulated data for the

first $\lceil T_p f_s/2 \rceil$ range bins as a result of the finite extent of the inputted reflectivity data and range registration.

The real and simulated data continue to display the same magnitude and character. Stronger signal power is again seen in the region of the Vancouver airport (range bins 4000 to 4600). The similarity of the green and blue curves indicates that the range-decompression, scaling, and range-compression processes do not alter the data in any meaningful way other than magnitude.

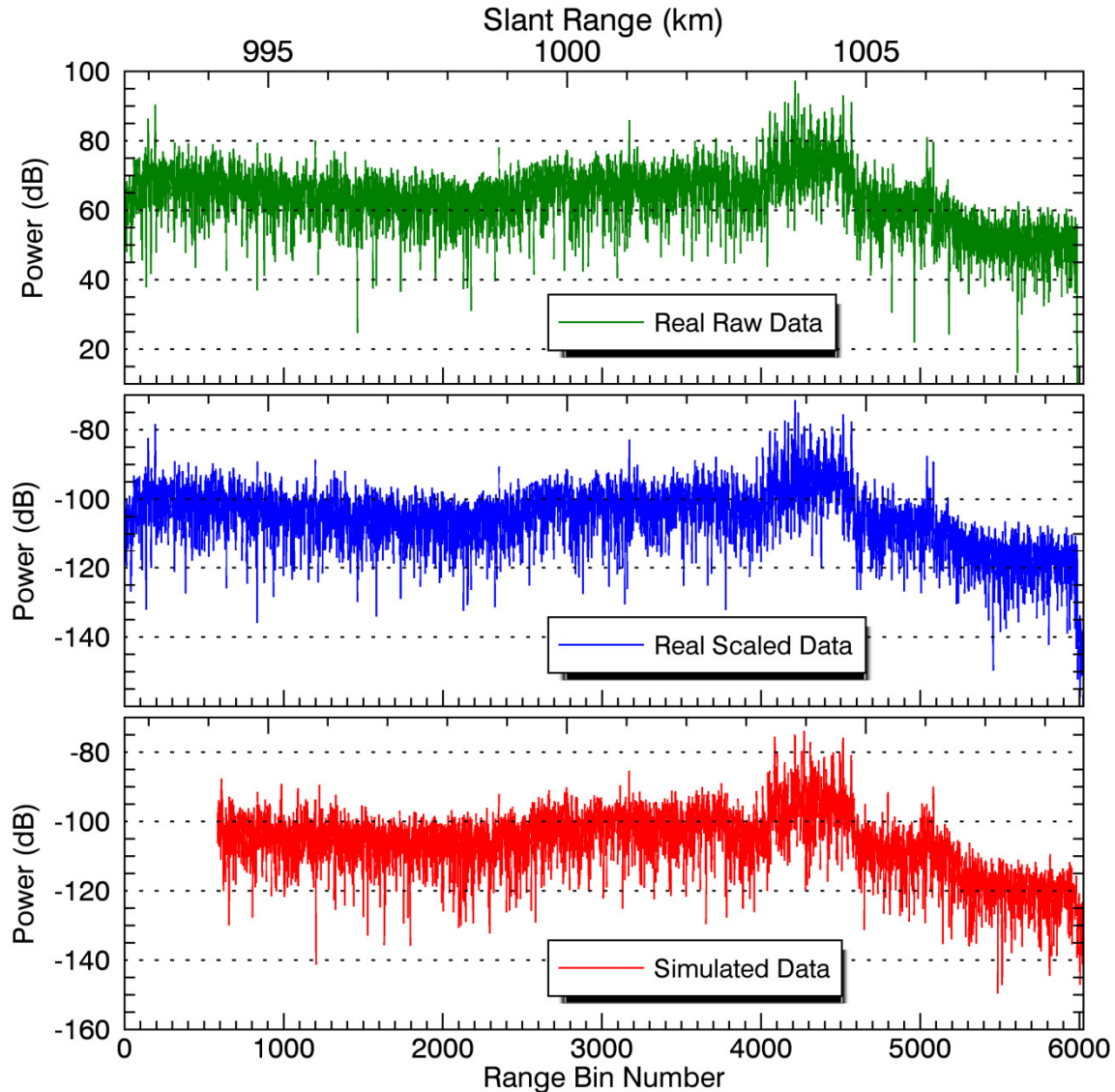


Figure 17: Range-compressed signal power for pulse number 13884.

The presence of the test target is not yet noticeable in the range-compressed data, i.e., a significant difference between the blue and red curves is not seen in the vicinity of range bin 4520, where the peak amplitude of the test target will be in the final SAR image.

7.2.1.3 Comparison of range- and azimuth-compressed data

The signal power data after range compression, range cell migration correction, and azimuth compression processing are compared for example line (12181) and pixel (4520) values in Figures 18 and 19, respectively. The image coordinate (4520, 12181) corresponds to the location of peak amplitude of the test target. The image data are now truncated at the largest line numbers due to the finite extent of the inputted reflectivity data and azimuth registration. The magnitude and character of the data continue to remain visually similar.

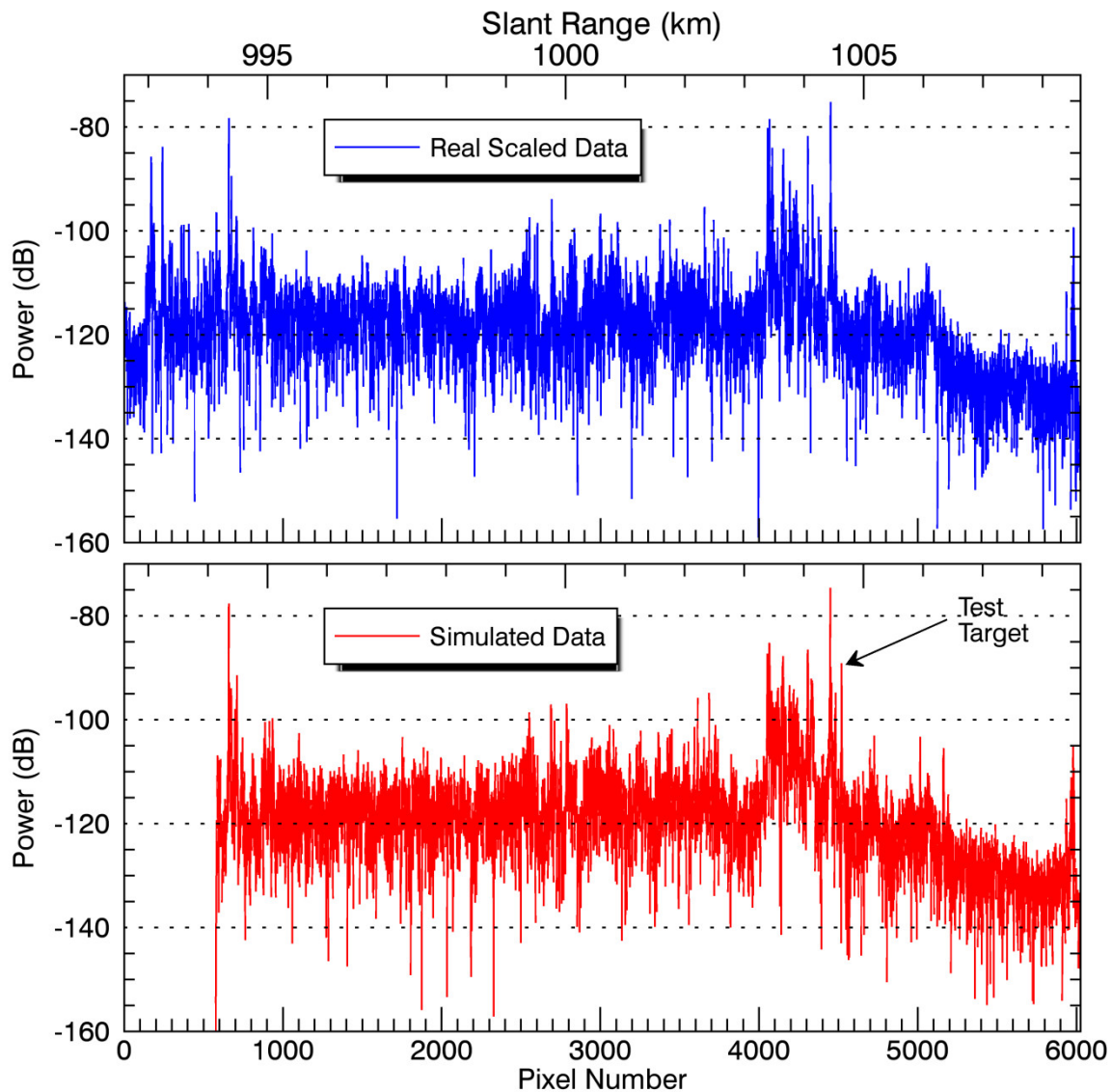


Figure 18: Range- and azimuth-compressed signal power for line number 12181.

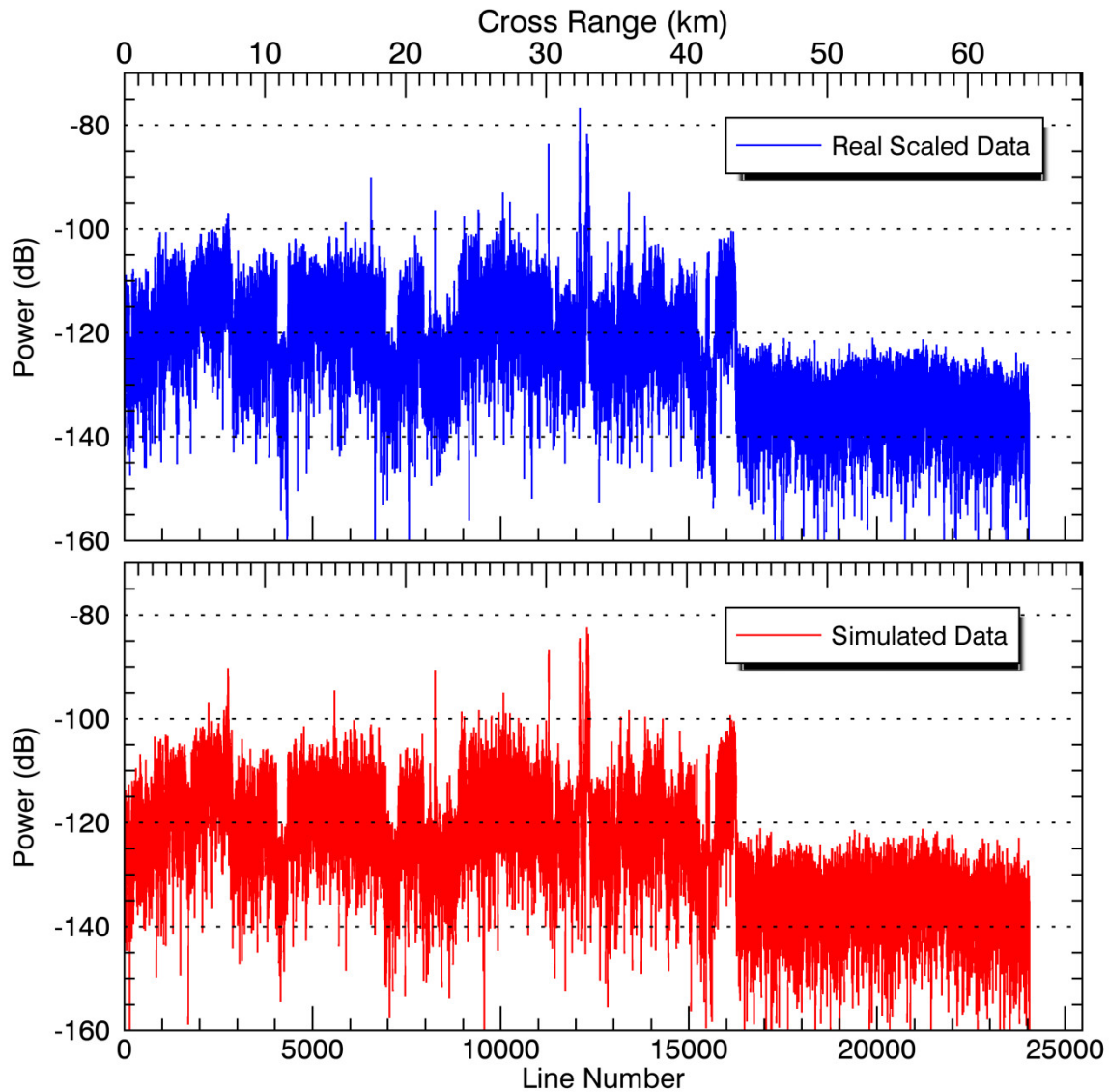


Figure 19: Range- and azimuth-compressed signal power for pixel number 4520.

A peak associated with the test target can now be seen in the bottom plot of Figure 18. A zoomed in view of the region of the test target signature is shown in Figure 20. Here the peak of the simulated test target is clearly visible extending to about 20 dB above the real, scaled, data.

7.2.1.4 Image comparison

The image data formed by fully processing (RDA) the real and simulated signals are compared in Figure 21. The results are visually similar. However, this entire image view cannot capture all of the details within the image data. Consequently, zoomed views of smaller areas are also displayed.

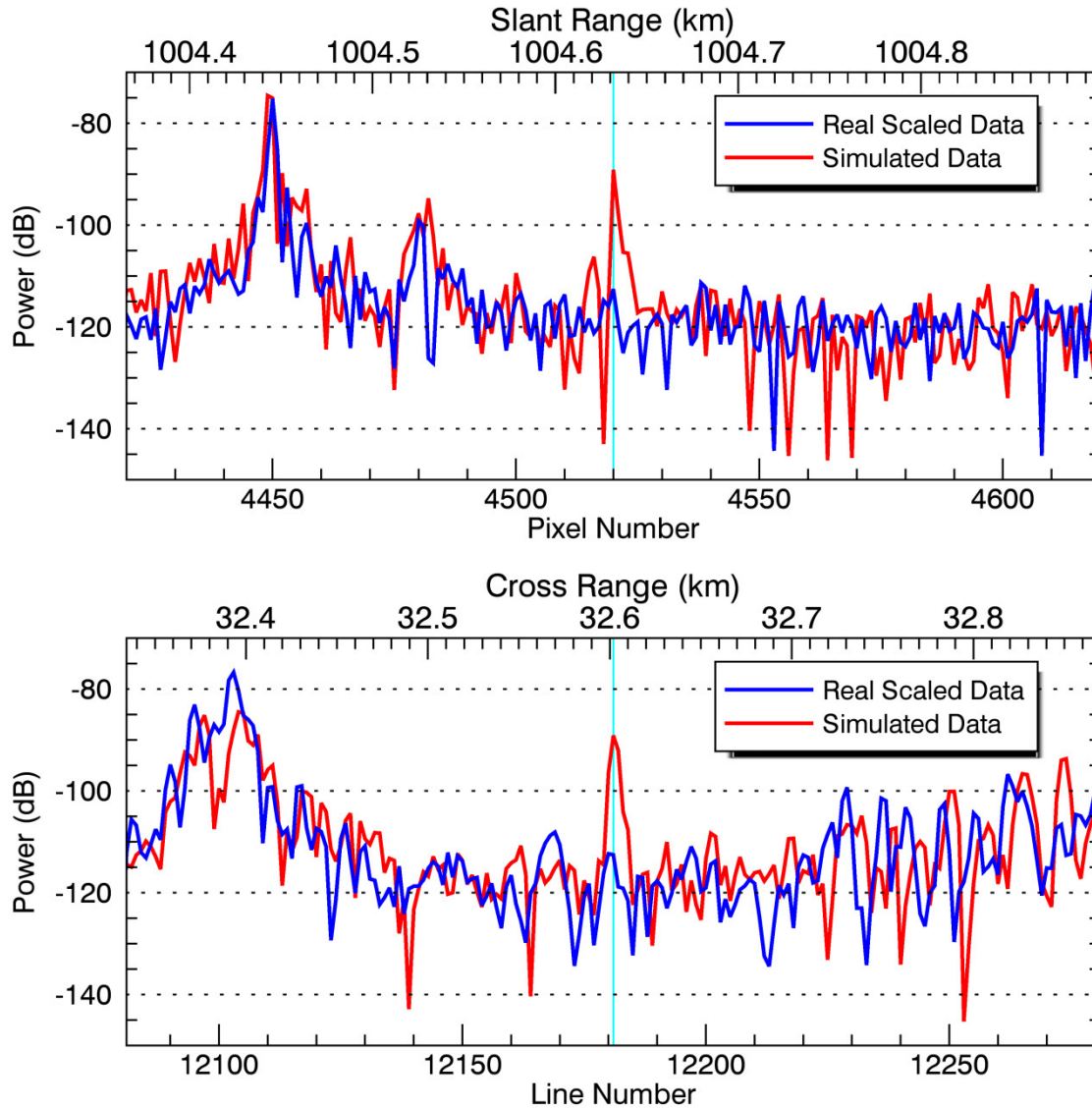


Figure 20: Range- and azimuth-compressed signal power in the region of the test target signature. The vertical cyan lines mark pixel number 4520 and line number 12181.

The mountainous region north of Vancouver that is highlighted with the cyan box is shown in Figure 22. This figure shows that terrain features such as mountains, valleys, lakes, and roads are effectively captured in the image corresponding to the fully simulated data. A zoomed view of the region defined by the cyan box in Figure 22 is shown in Figure 23. This figure highlights the western side of Crown Mountain with a cyan ellipse and shows that terrain shadowing effects have also been effectively captured.

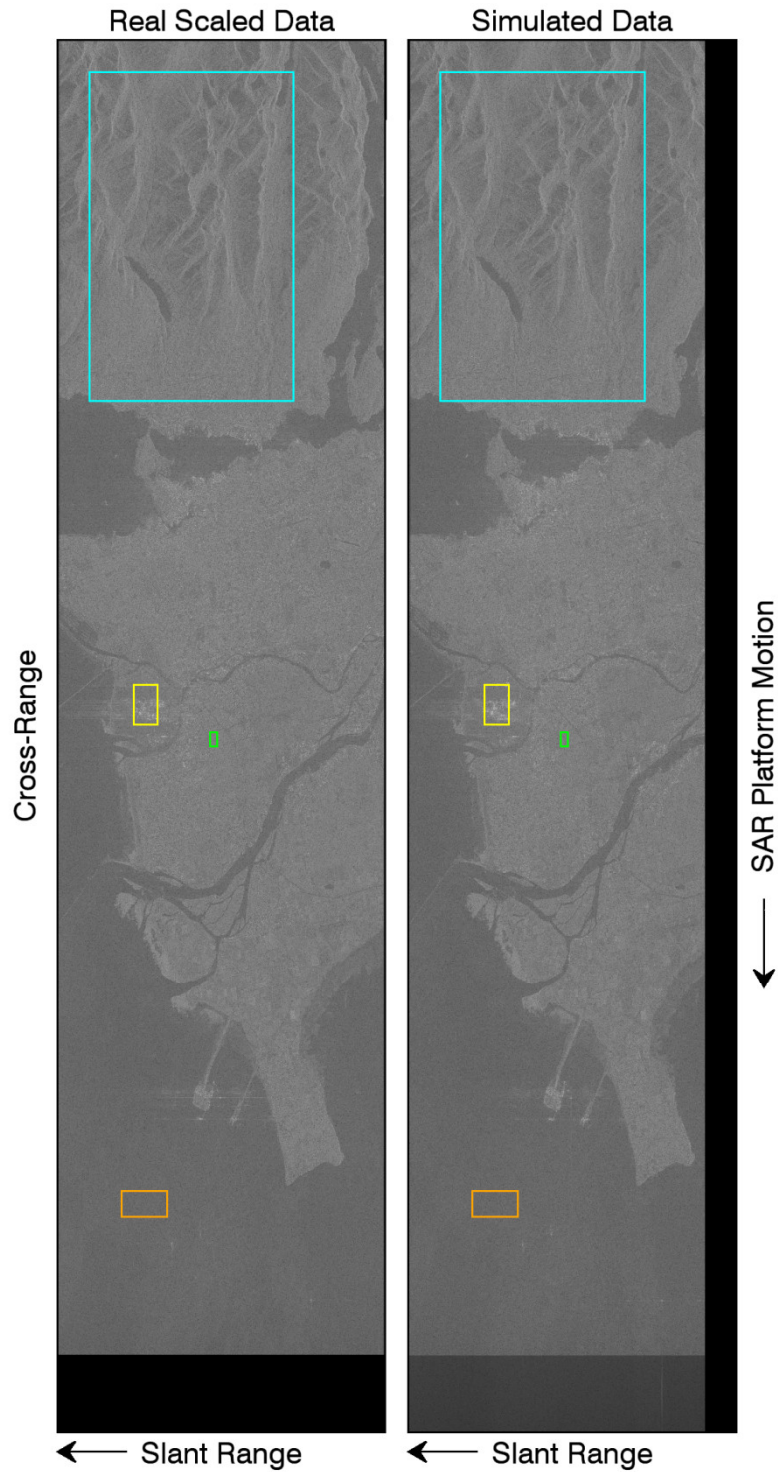


Figure 21: SAR images corresponding to the real, scaled signals (left) and the simulated signals (right). Black regions correspond to no data.

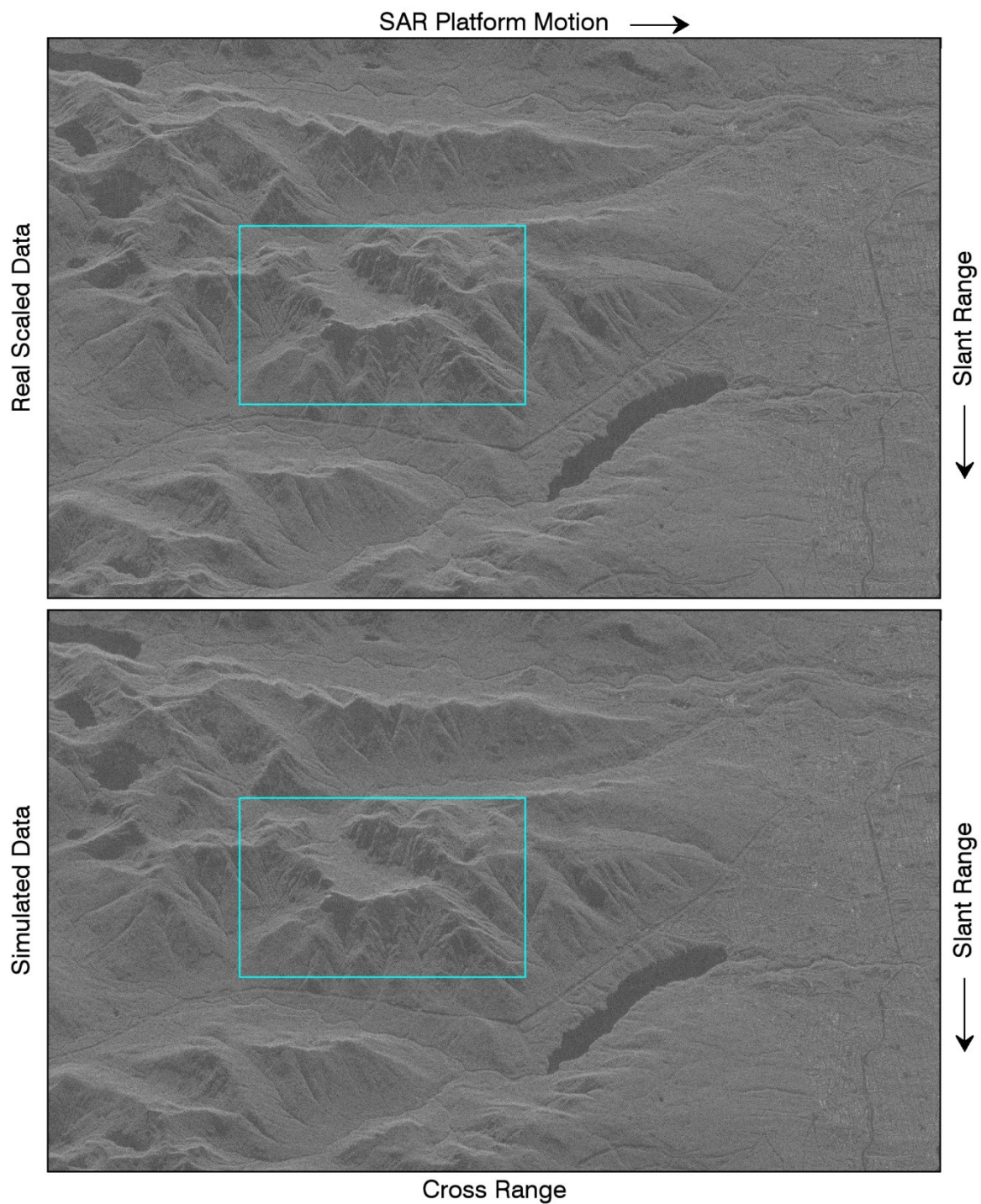


Figure 22: SAR images of the mountainous region north of Vancouver (cyan box in Figure 21) corresponding to the real, scaled signals (upper) and the simulated signals (lower).

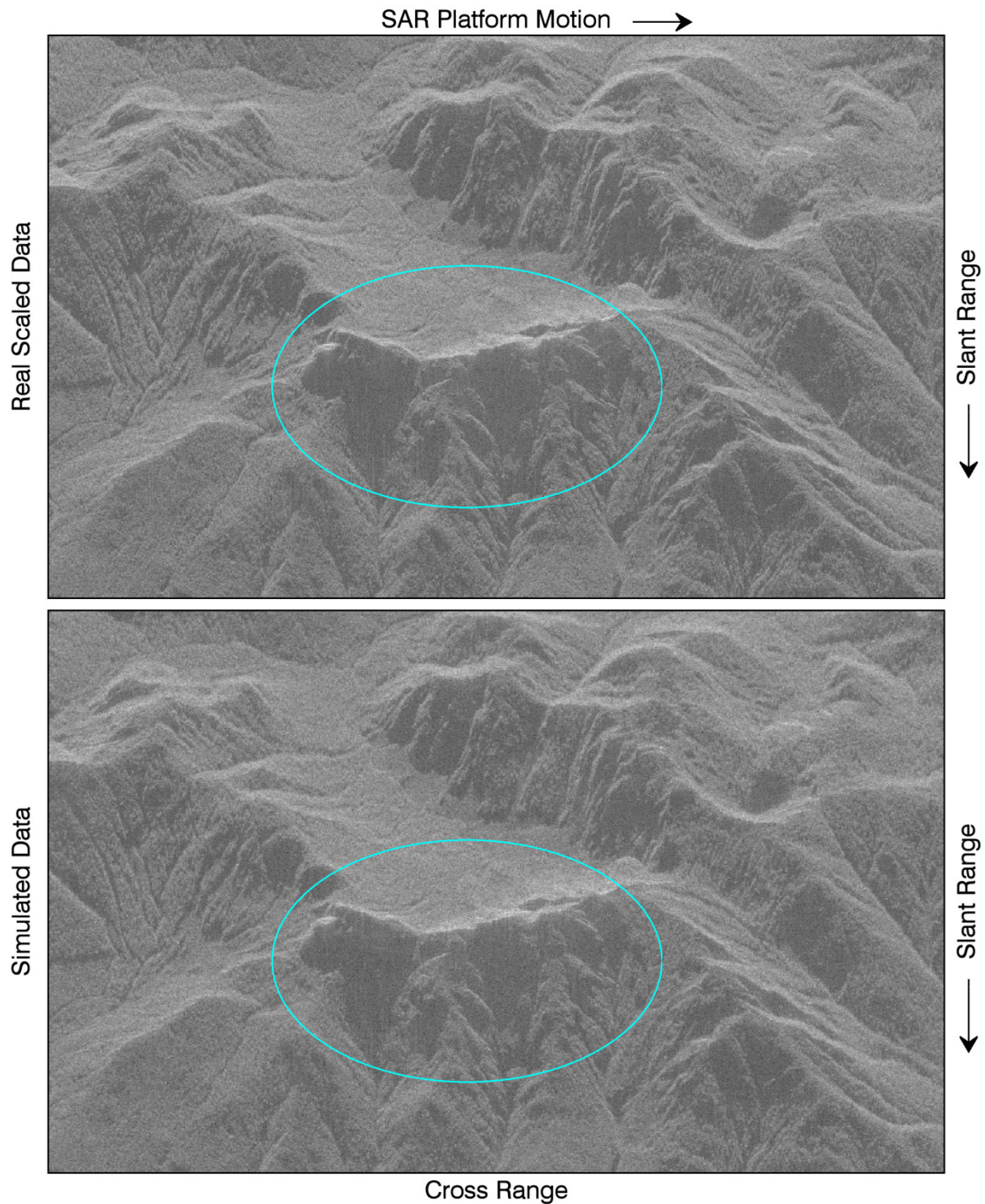


Figure 23: SAR images of Crown mountain (cyan box in Figure 22) corresponding to the real, scaled signals (upper) and the simulated signals (lower).

A zoomed view of the Vancouver airport (yellow box in Figure 21) is shown in Figure 24. The faint peak of the test target is identified in the simulated data with the yellow arrow. This peak is not in the real image,

as intended. The airport region contains a good contrast of bright pixels (strong scatterers) and dark pixels (weak scatterers). This contrast helps to demonstrate that the simulated image is not quite as sharp as the real image. This is expected since the impulse response of the simulated SAR system is not a perfect Dirac delta function. That is, the side lobes associated with the impulse response blur the simulated image relative to the inputted reflectivity field. The strong scatterers also reveal the main weakness of the simulation approach. That is, side lobes, associated with strong scatterers, that are visible in the inputted image that is used to represent the reflectivity field, will be carried through to the simulated image. But, also, these side lobes will themselves generate side lobes in the simulated image. Overall, the blurring associated with the SAR system impulse response is being applied twice to the real-world scene in the case of the simulated image. This is considered to be an acceptable limitation since the intended use of this simulation is to examine the effects of jamming. It is the relative change that occurs in the simulated image due to jamming effects that is of importance. If this weakness is found to be problematic during the jamming studies then future work may be performed to attempt to mitigate its effects. Or, key areas of the input image could perhaps be edited by hand to reduce unwanted effects caused by strong side lobes.

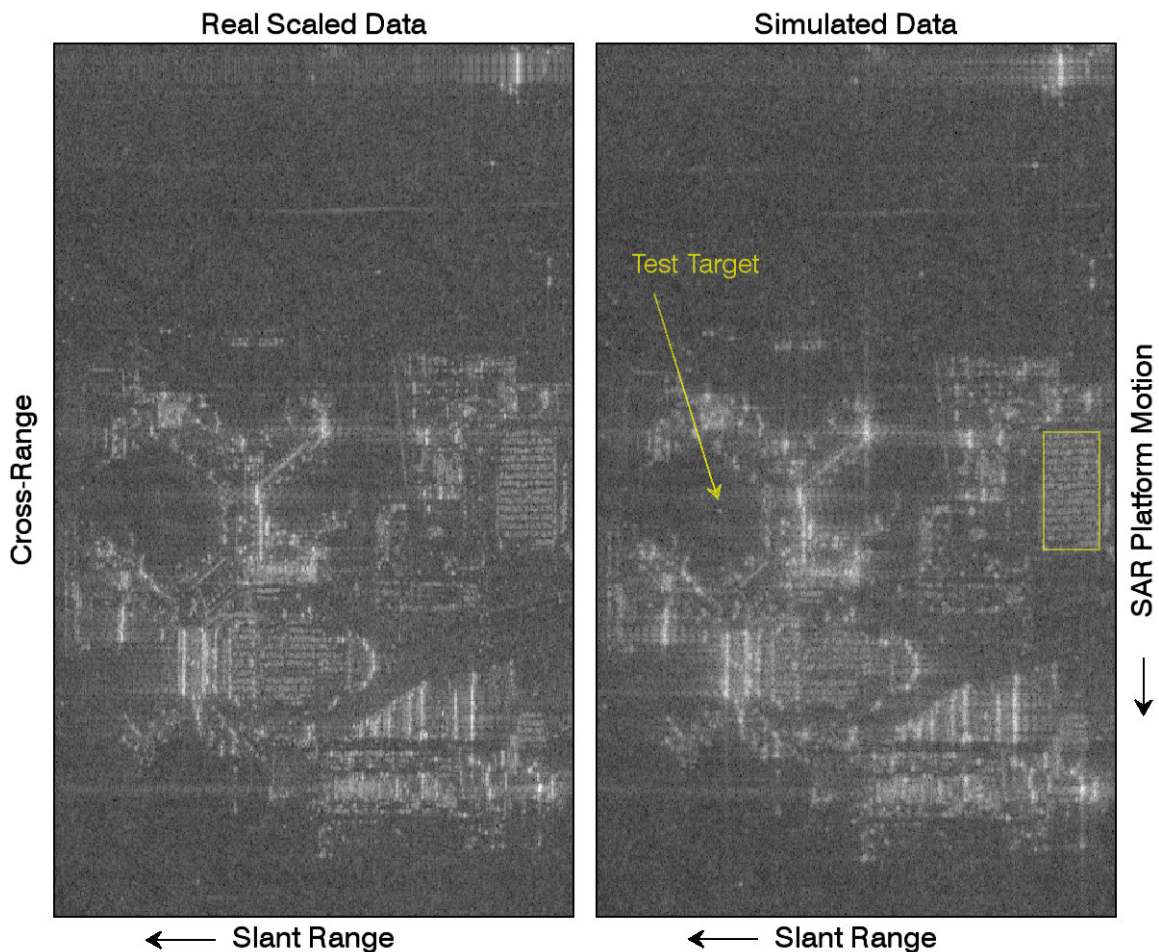


Figure 24: SAR images of the Vancouver airport (yellow box in Figure 21) corresponding to the real, scaled signals (left) and the simulated signals (right).

The RCS of the example test target was chosen to correspond to a pickup truck (200 m^2) [11] so that the magnitude of the test target peak in the simulated image could be compared with the magnitudes seen in a parking lot area of the Vancouver airport. The image power data corresponding to the yellow box of Figure 24 is plotted in Figure 25. The upper plot shows the image power for each image pixel within the yellow box. The cyan line shows the image power of the test target peak. The lower plot shows a histogram of the image power within the yellow box and the cyan line again represents the image power of the test target peak. It can be seen that the test target peak is at the upper end of the image power levels in the parking lot. This is as expected since the parking lot would contain mostly standard automobiles (RCS 100 m^2 [11]) and fewer larger scattering objects such as pickup trucks. This result provides confidence that the test target signal power has been correctly represented in the simulated environment and that the power level of jammer signals will also be correctly represented.

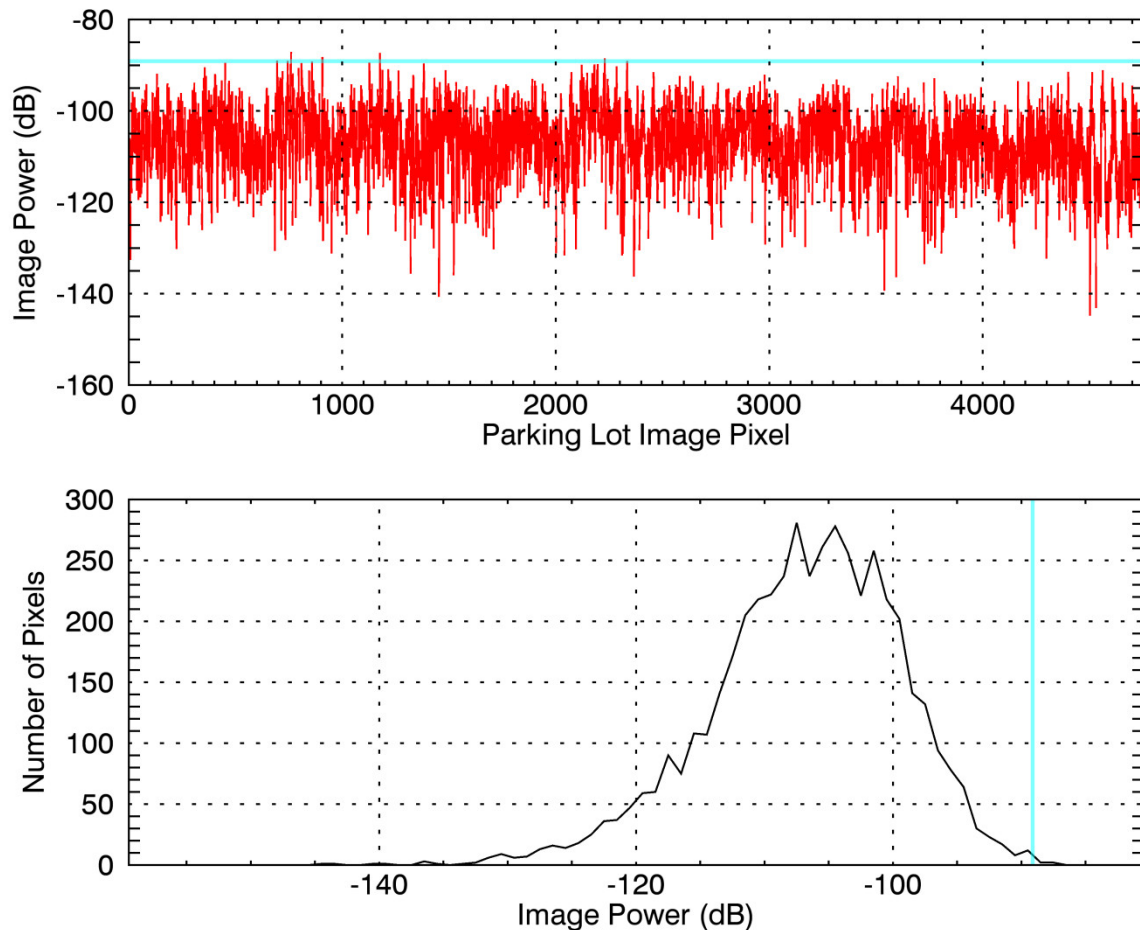


Figure 25: Simulated image power associated with the parking lot region in the yellow box of Figure 24.

7.2.1.5 Comparison of image statistics

It is difficult to compare the statistical properties of the raw signals since all of the scatterers within the entire beam footprint will contribute to an individual signal sample and the properties of these scatterers

will vary significantly over the large extent of the beam footprint. However, the statistics of the image data can be examined within areas of uniform scattering properties.

Figure 26 shows a zoomed view of the image data corresponding to the forest area adjacent to the Colonel Sherman Armoury, in Richmond, British Columbia, which is marked with the green box in Figure 21. The image data, corresponding to the real, scaled signals (left) and the simulated signals (right), show visually similar scenes. The Probability Density Functions (PDF) of the image amplitudes within this forest area are compared in Figure 27, along with the numerical values of the moments of the distributions. Rayleigh distributions corresponding to the listed mean values are shown as dashed lines. The PDFs and moment values are very similar indicating that the simulation has effectively captured the amplitude statistics of the surface scattering process.

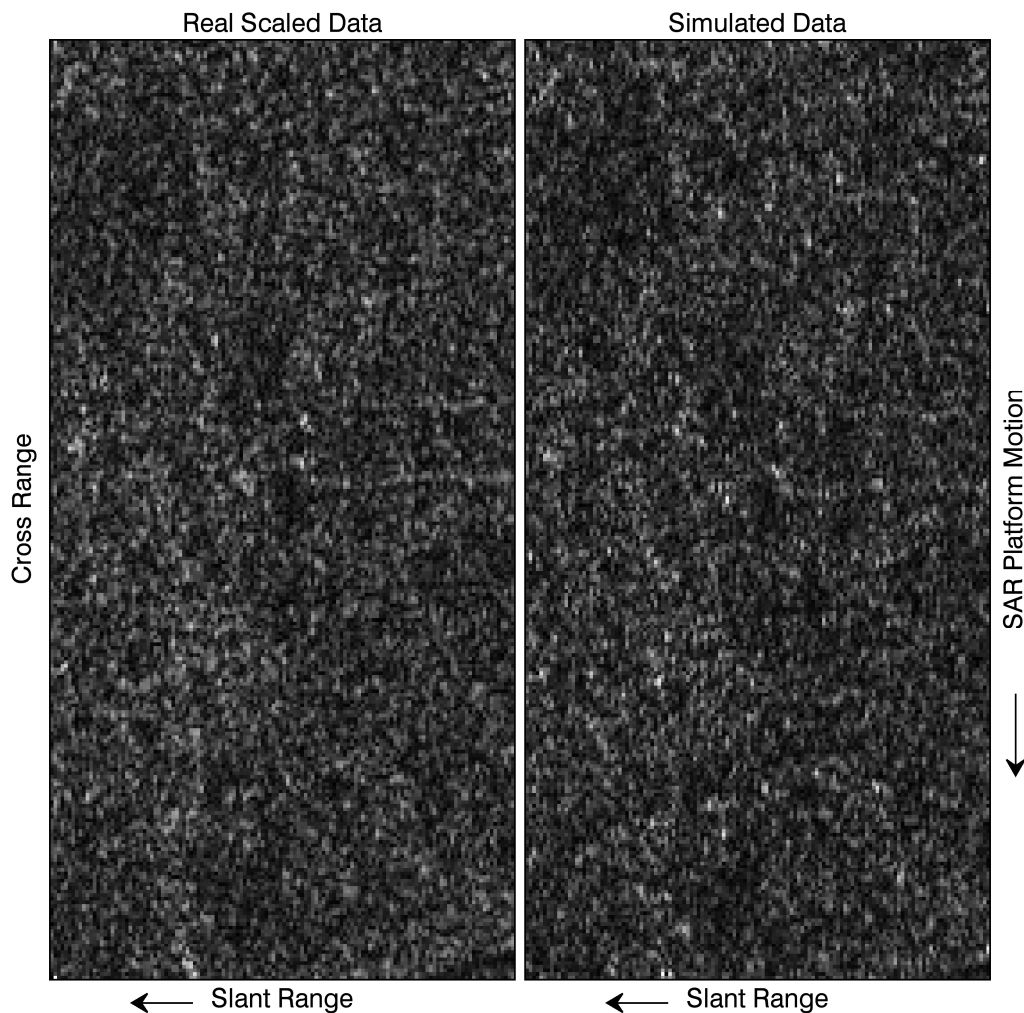


Figure 26: SAR images of a forest area (green box in Figure 21) corresponding to the real, scaled signals (left) and the simulated signals (right).

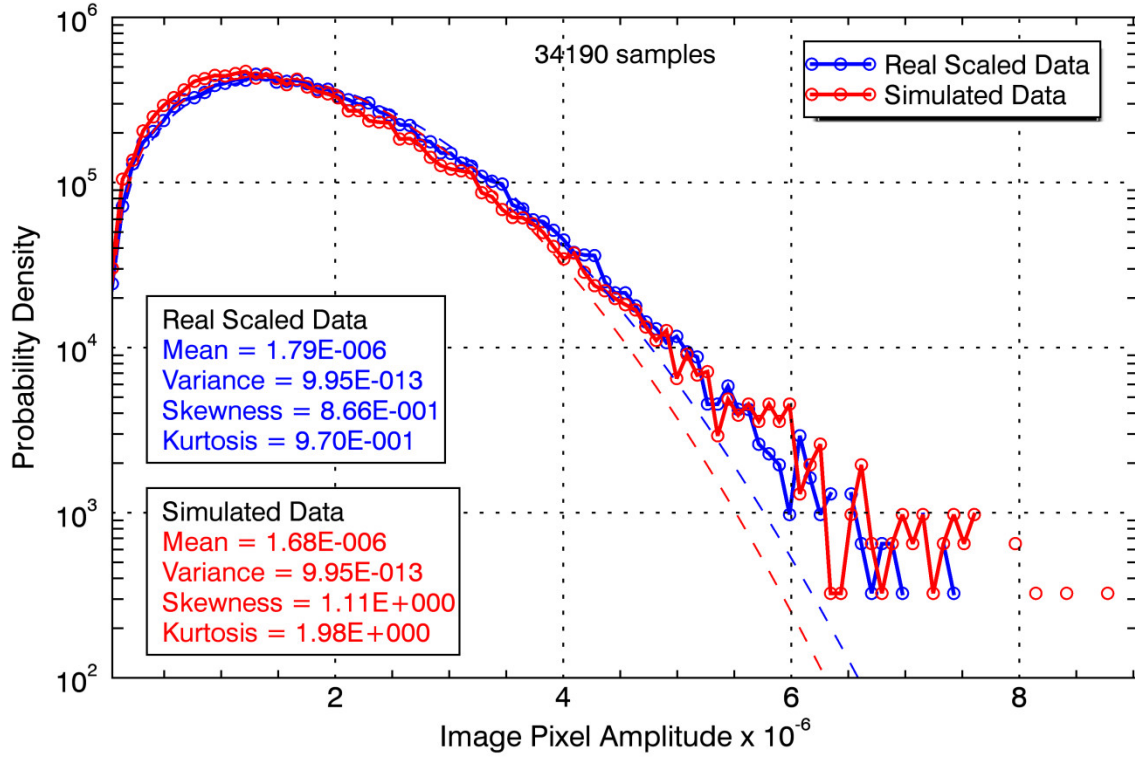


Figure 27: Image amplitude probability density functions for the forest area shown in Figure 26.

The spatial autocorrelation of the image amplitude data can be computed using the Wiener-Khinchin theorem [27]. That is, the normalized two-dimensional autocorrelation function can be computed as

$$\mathfrak{R}_{V'''}(m, n) = \frac{|\mathbf{DFT}_{mn}^{-1}\{(M_s N_s \mathbf{DFT}_{mn}\{V_{mn}'''\}) (M_s N_s \mathbf{DFT}_{mn}\{V_{mn}'''\})^*\}|}{(M_s N_s)^2} \quad (115)$$

where \mathbf{DFT}_{mn} computes the discrete Fourier transform across both the m (slant range) and n (cross range) dimensions, the $*$ operator represents complex conjugation, the m and n values are limited to the region corresponding to the forest area scene in Figure 26, and M_s and N_s are the number of slant-range and cross-range image pixels in the scene, respectively. The autocorrelation functions for the real, scaled data, and the simulated data, in the case of the forest area, are compared as surfaces in Figure 28. In this view the data have been arranged so that the point of zero slant-range lag and zero cross-range lag is in the middle of the surface. Cuts through the autocorrelation function along zero slant-range lag and zero cross-range lag in the region of peak autocorrelation are shown in Figure 29. Very similar autocorrelation is seen along both dimensions.

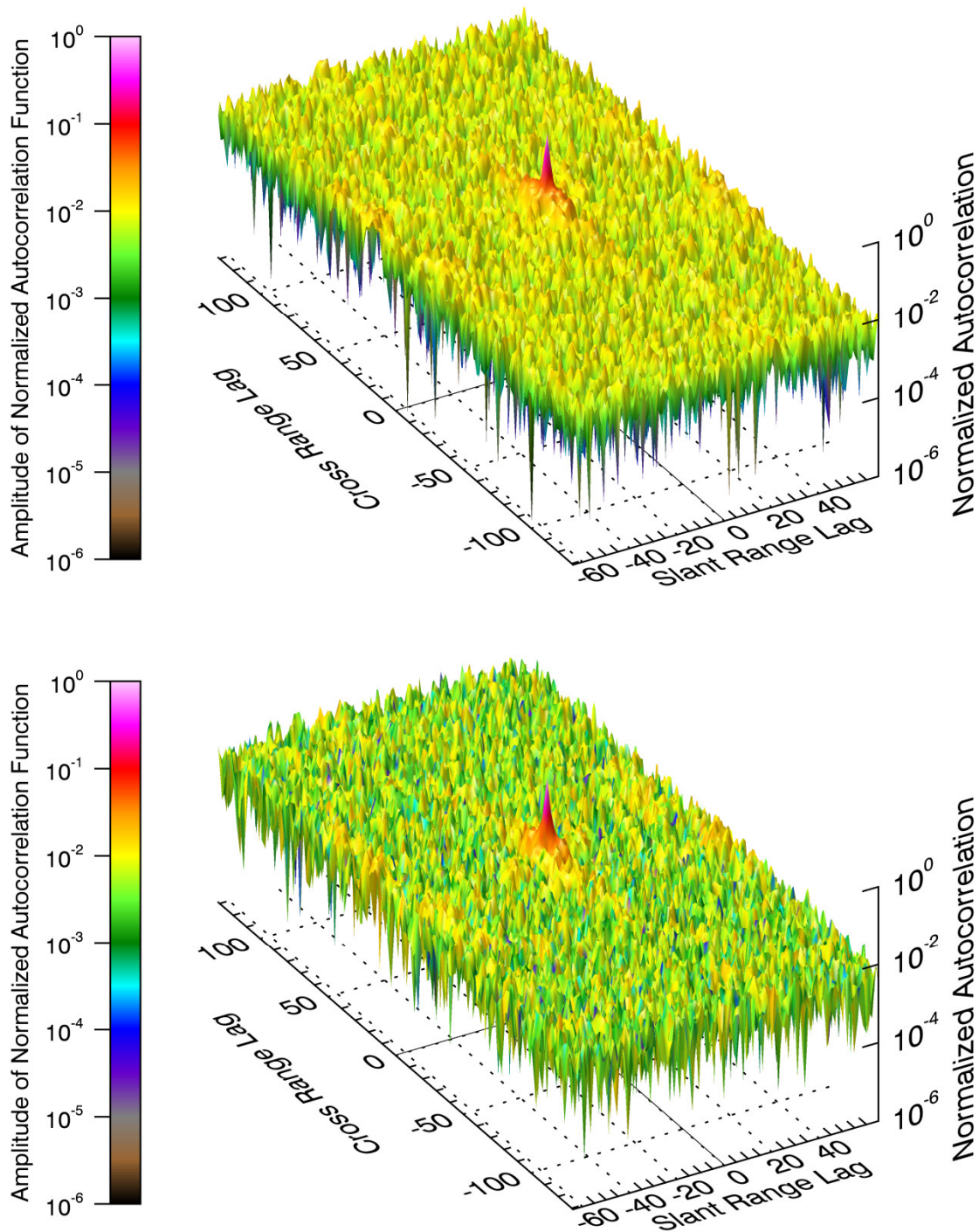


Figure 28: Normalized spatial autocorrelation functions corresponding to the real, scaled, image data (upper) and the simulated image data (lower) for the forest area (Figure 26).

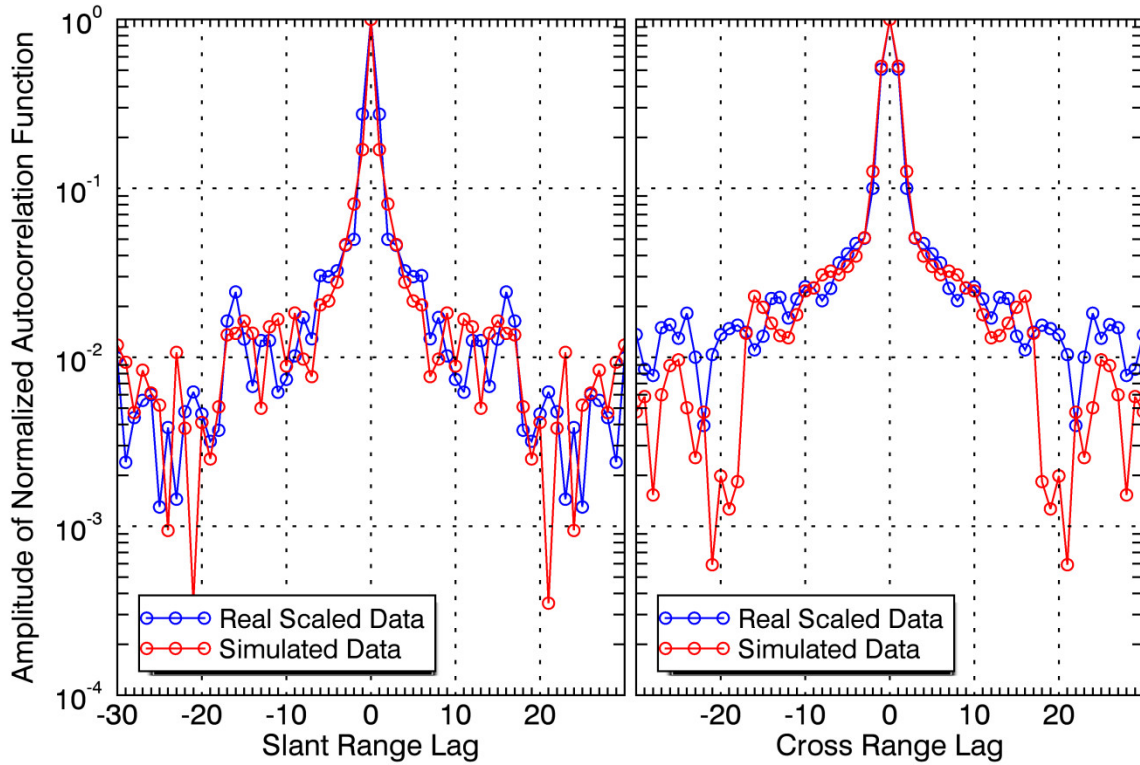


Figure 29: Normalized spatial autocorrelation functions at zero cross-range lag (left) and zero slant-range lag (right) for the forest area (Figure 26).

The statistical analysis performed on the image data in the forest area is repeated for a uniform patch of sea located south-west of the Tsawwassen Peninsula (orange box in Figure 21). An image of the sea patch is shown in Figure 30. The image amplitude PDFs and their corresponding moments are shown in Figure 31. A surface view of the normalized image amplitude spatial autocorrelation function is shown in Figure 32. Cuts along this surface for zero slant-range lag and zero cross-range lag in the region of the autocorrelation function peak are shown in Figure 33. As in the case of the forest area, these statistical comparisons show good agreement indicating that the statistical properties of the real RADARSAT-2 MODEX 1 data have been effectively captured in the simulated signals.

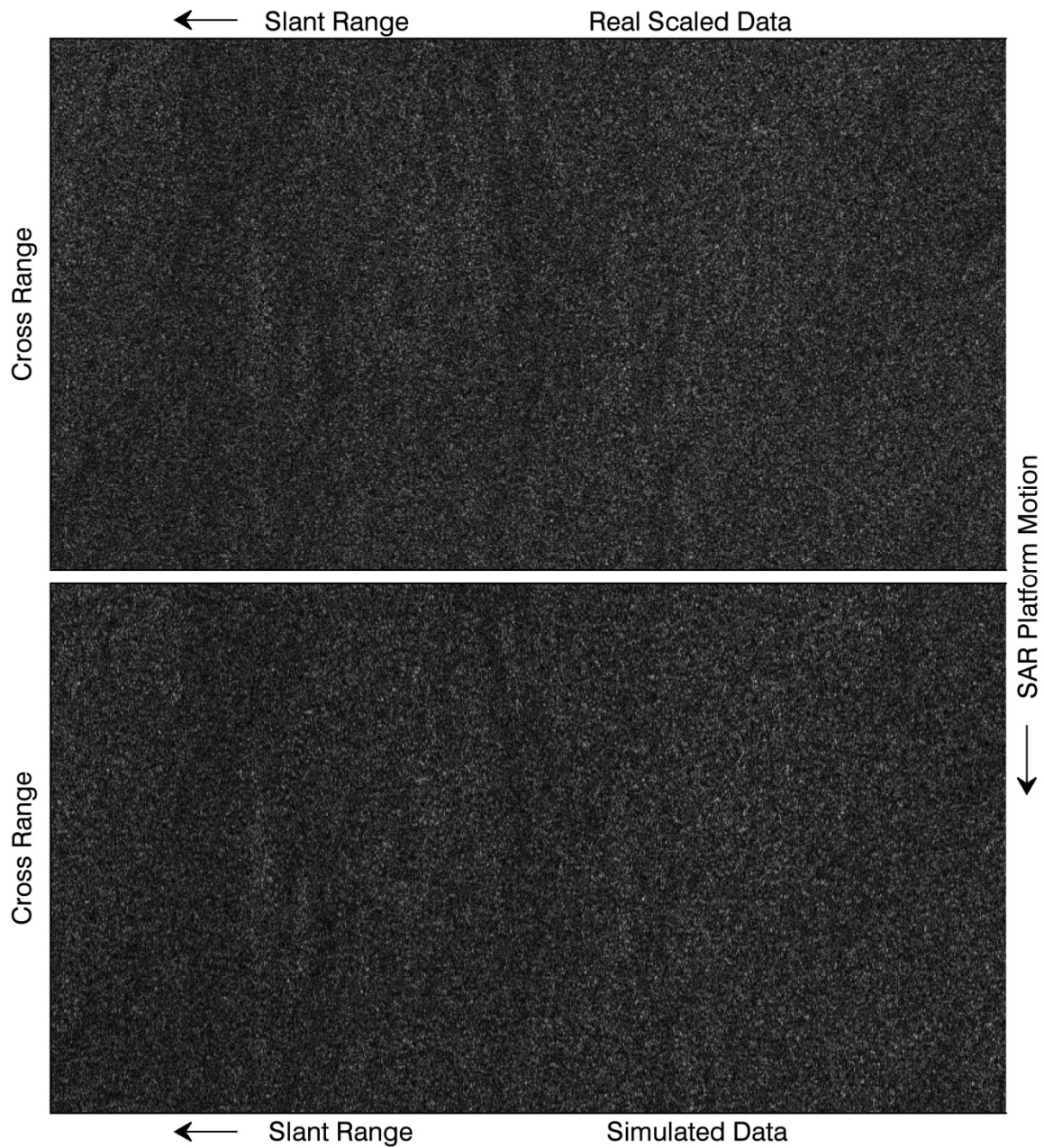


Figure 30: SAR images of a uniform sea patch (orange box in Figure 21) corresponding to the real, scaled signals (upper) and the simulated signals (lower).

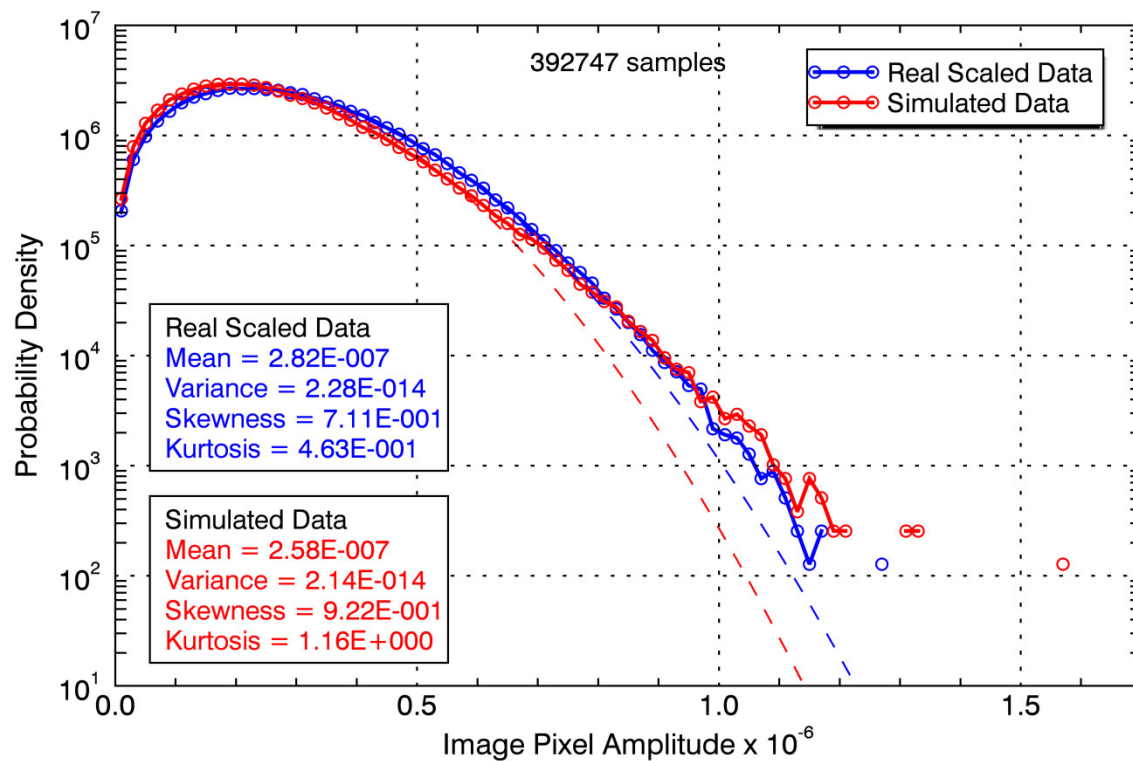


Figure 31: Image amplitude probability density functions for the uniform sea patch shown in Figure 30.

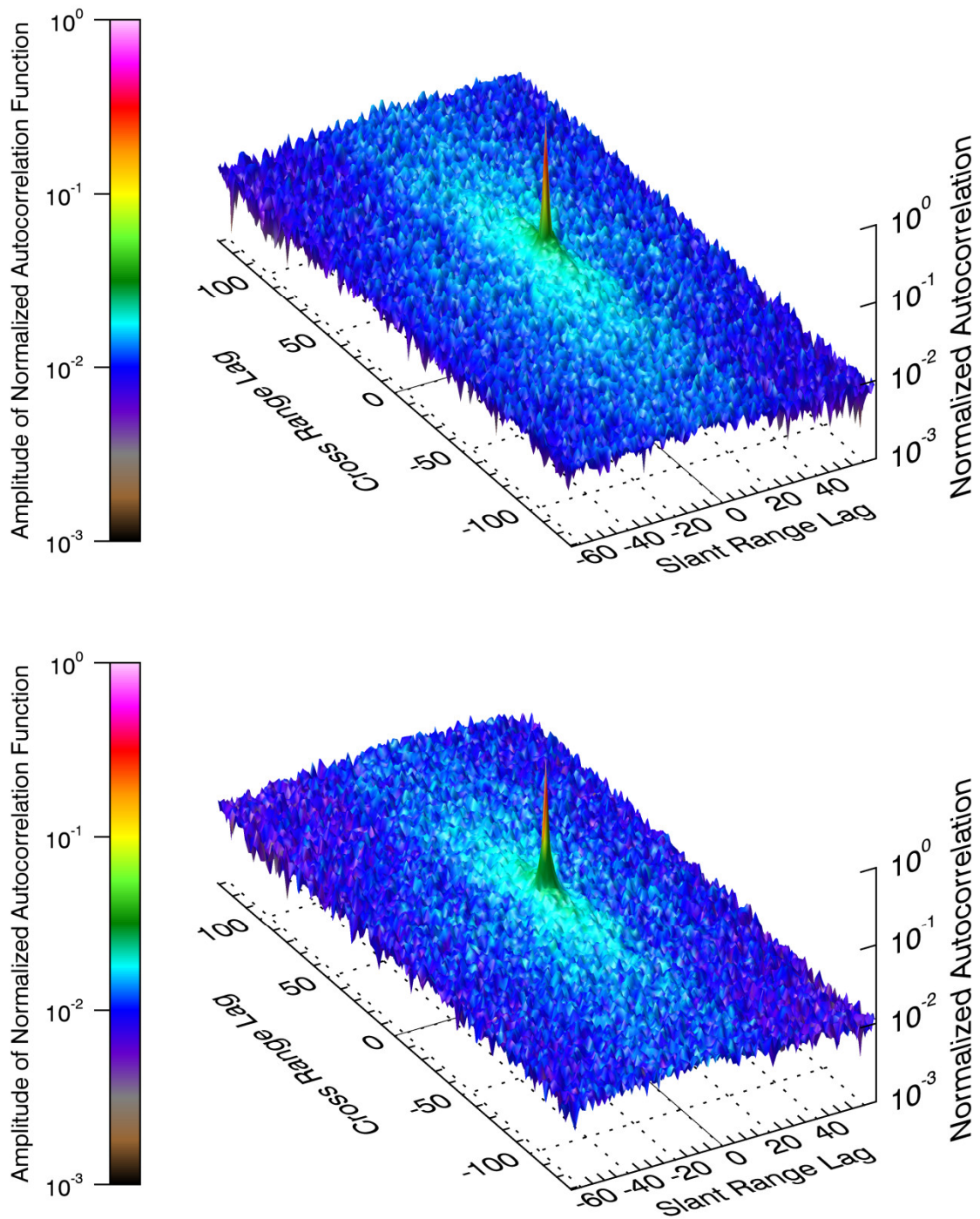


Figure 32: Normalized spatial autocorrelation functions corresponding to the real, scaled image data (upper) and the simulated image data (lower) for the uniform sea patch (Figure 30).

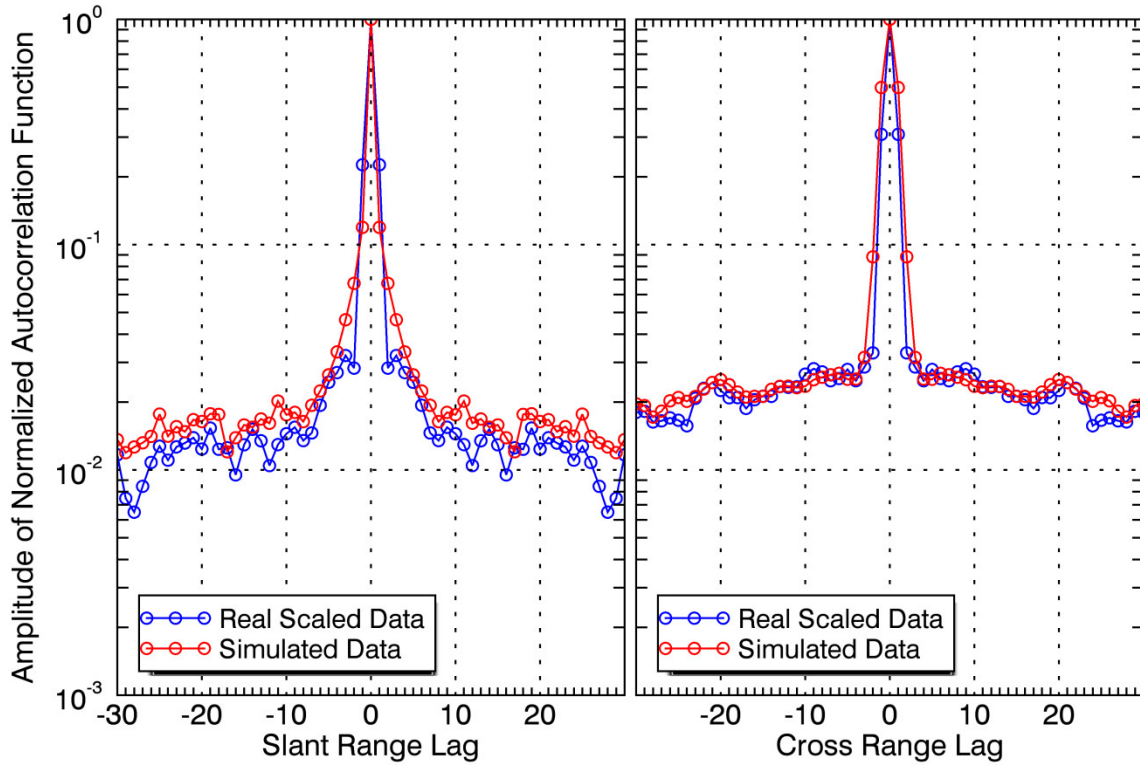


Figure 33: Normalized spatial autocorrelation functions at zero cross-range lag (left) and zero slant-range lag (right) for the uniform sea patch (Figure 30).

7.2.2 Case 2: W2 mode

The RADARSAT-2 data set used for the Case 2 evaluation was collected in the Vancouver area starting at 14:26 Z on December 22, 2010. The overarching filename associated with this data set is “Vancouver_20101222_0347901.” The associated simulation parameters are listed in Tables 5, Table 6, and Table 7. For the W2 mode, the simulation interpolates azimuth and elevation antenna gain pattern values as required from beam pattern data provided by MDA. The azimuth and elevation antenna gain patterns in the region of the main lobe are shown in Figure 34. The simulation considers the full gain pattern out to $\pm 90^\circ$ azimuth and elevation, relative to the beam axis. The position of the receive phase centre, Δy , is set to 0 m since the W2 mode uses the full aperture for both transmit and receive.

Table 5: Control parameters for the W2 mode simulation.

Description	Value
Range resolution factor for surface scatterer spacing	1
Azimuth resolution factor for surface scatterer spacing	1
Range tolerance for determining convergence of Earth intersection point algorithm	0.01 m

Table 6: SAR parameters for the W2 mode simulation.

Description	Symbol	Value
Sampling frequency	f_s	12.67 MHz
Transmitted frequency	f_c	5.405 GHz
Pulse length	T_p	41.52 μ s
Frequency modulation rate	K_p	2.793×10^{11} cycles s ⁻²
Pulse repetition interval	T_s	0.7493 ms
Azimuth beam axis angle	ϕ_b	0.0°
Transmit power [26]	P_t	5.12 kW
Input impedance of antenna port	Z	50 Ω
System Losses	L_s	3.4 dB
Number of bits used in analogue to digital conversion	n_b	8
Polarization		HH
Receiver system gain	G_s	0.0 dB
Bits associated with mean receiver noise level	\vec{b}_n	[0]
Antenna length [26]	L_A	15 m
Antenna width [26]	W_A	1.37 m
y_T -axis position of receive phase centre	Δy	0 m

Table 7: Image formation parameters for the W2 mode simulation.

Description	Symbol	Value
Kaiser window shape parameter used in sinc interpolation	β_K	2.5
Number of interpolates used in sinc interpolation	N_i	16
Minimum acceptable azimuth oversampling ratio	α_{al}	1.3
Maximum acceptable azimuth oversampling ratio	α_{au}	1.4

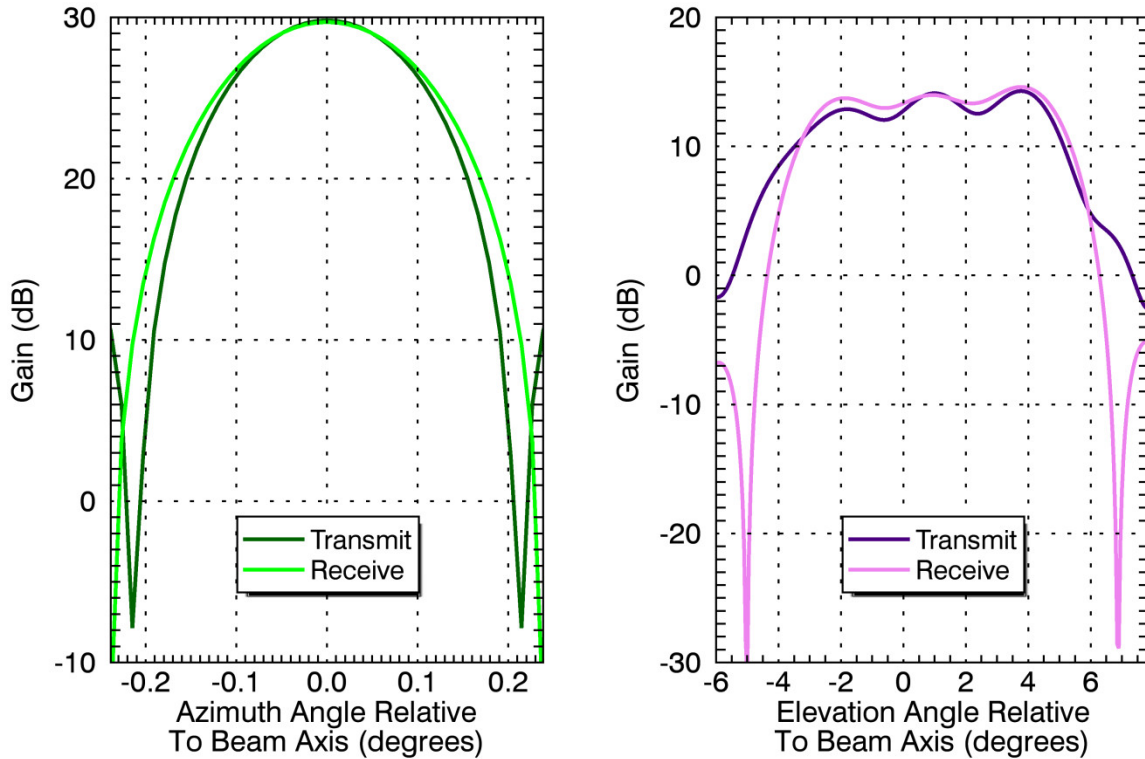


Figure 34: *Transmit and receive azimuth and elevation antenna gain patterns used for the W2 mode with HH polarization.*

7.2.2.1 Unprocessed data

The simulated unprocessed (raw) in-phase and quadrature data are the main output of this simulation. An example set of I and Q data as a function of slant range are shown in Figure 35 for pulse number 5757, which illuminates the Vancouver airport. Range bins from 0 to ~4200 correspond to the land region and range bins greater than ~4200 correspond to the sea region. The largest magnitude values correspond to the structures at the Vancouver airport. Since the “Vancouver_20101222_0347901” data set was collected with a standard RADARSAT-2 mode (W2), no real, raw signal data are available for any point in the image formation processing. Consequently, only the properties of the real, image data can be compared with the simulated data.

7.2.2.2 Image Comparison

The real image data are provided in Tag Image File Format (TIFF) or National Imagery Transmission Format (NITF) files. These data can be converted into radar brightness values (β^o) using the metadata supplied with the RADARSAT-2 data set [13]. These β^o values correspond to image pixel power. Consequently, the real image amplitude data used for the comparisons in this section are calculated by taking the square root of these values and scaling the result such that the mean value is equal to the mean value of the simulated image amplitude data.

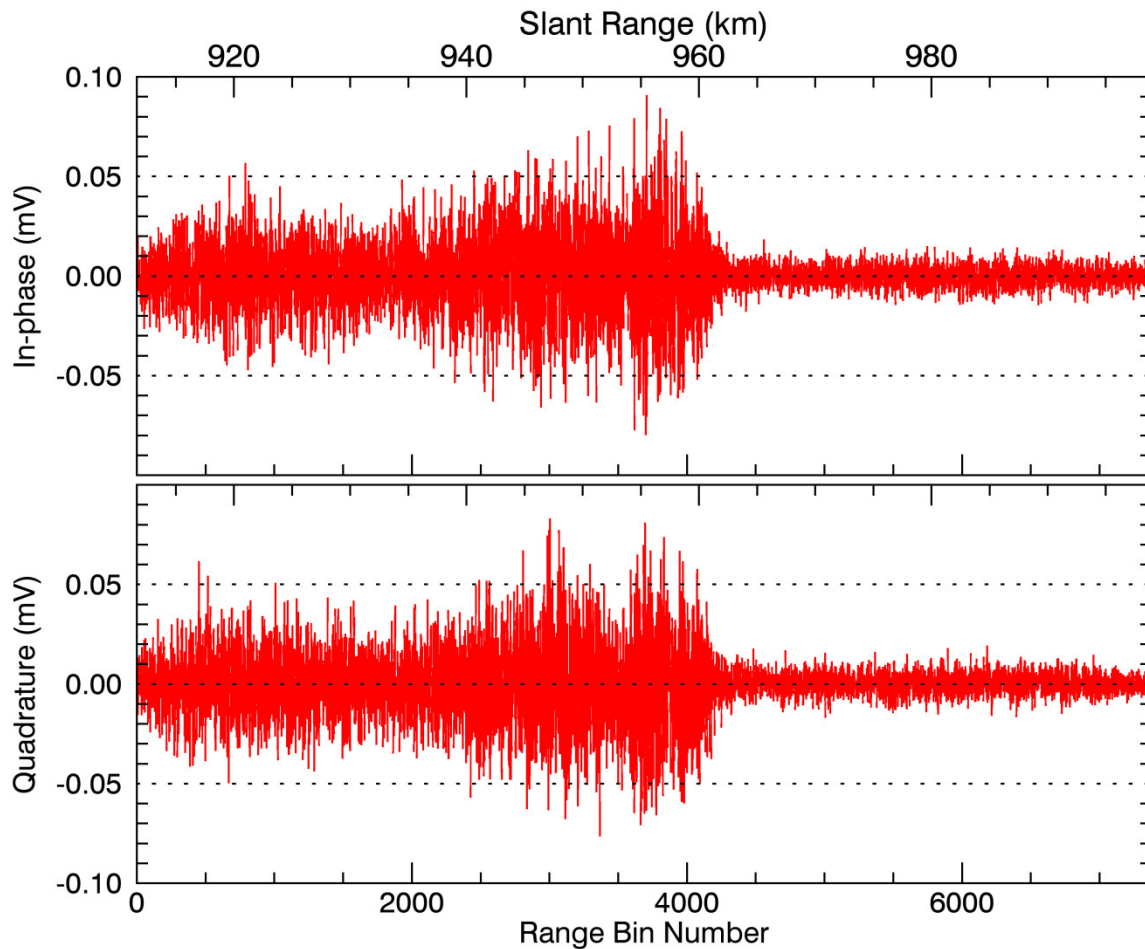


Figure 35: *Simulated unprocessed in-phase and quadrature data for pulse number 5757.*

The complete real and simulated images corresponding to the W2 mode case are compared in Figure 36. The region of no data (black area) in the simulated image is again caused by the limited extent of the inputted surface reflectivity data and range registration. The two images are visually similar. Since all of the details in the actual image data cannot be displayed on this scale, further image comparisons are made for the smaller regions marked with the cyan and yellow boxes.

Images of the mountainous region north of Vancouver are compared in Figure 37. The comparison shows that terrain features and shadowing effects have been effectively captured in the simulated data.

Images of the region extending from Vancouver airport to the Burrard Inlet are shown in Figure 38. This comparison shows that approximately the same level of detail, in terms of objects such as roads, buildings, ships, etc., is present in both images. Close examination, however, reveals that the simulated image is slightly more blurry as expected, similarly to the MODEX case discussed in Section 7.2.1.

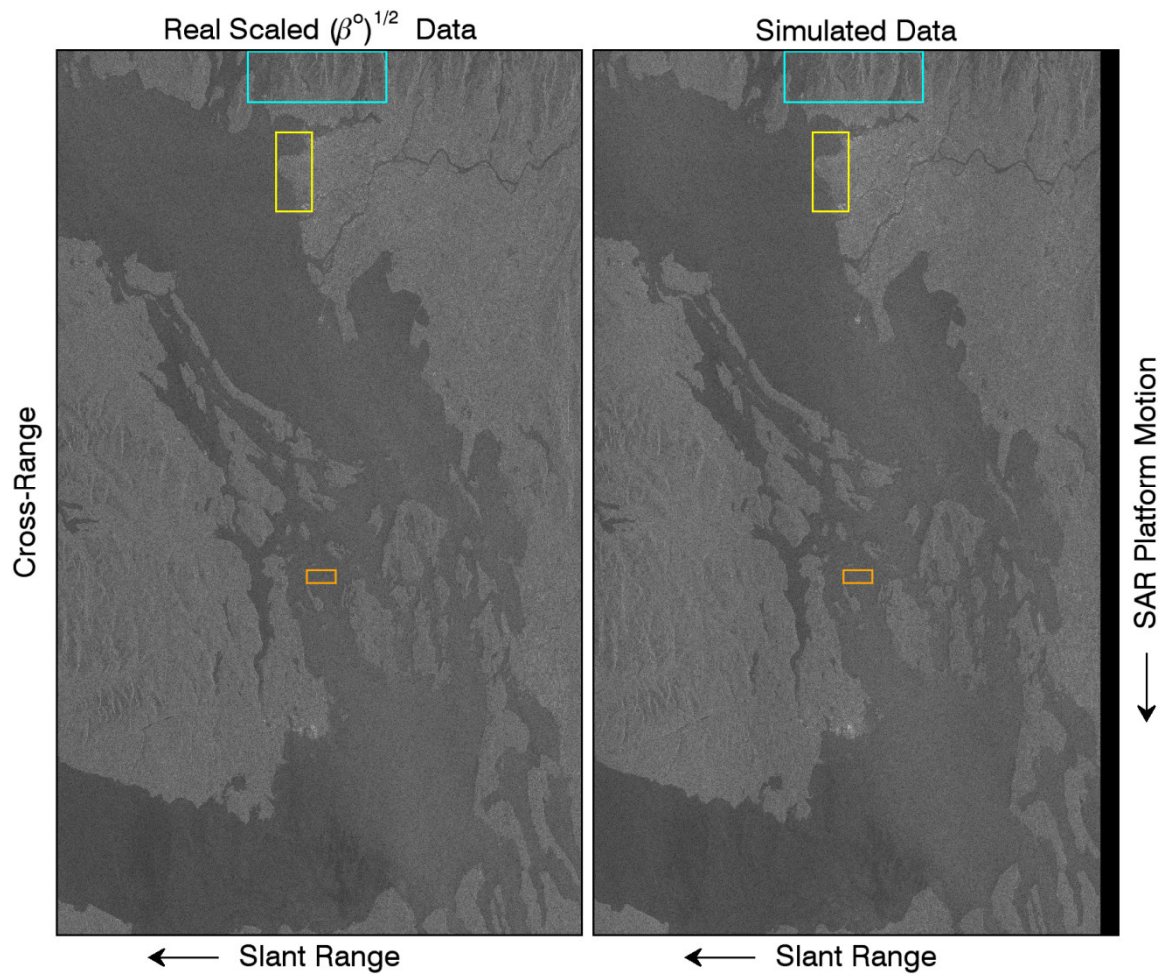


Figure 36: SAR images corresponding to the real, scaled $(\beta^0)^{1/2}$ data (left) and the simulated signals (right).

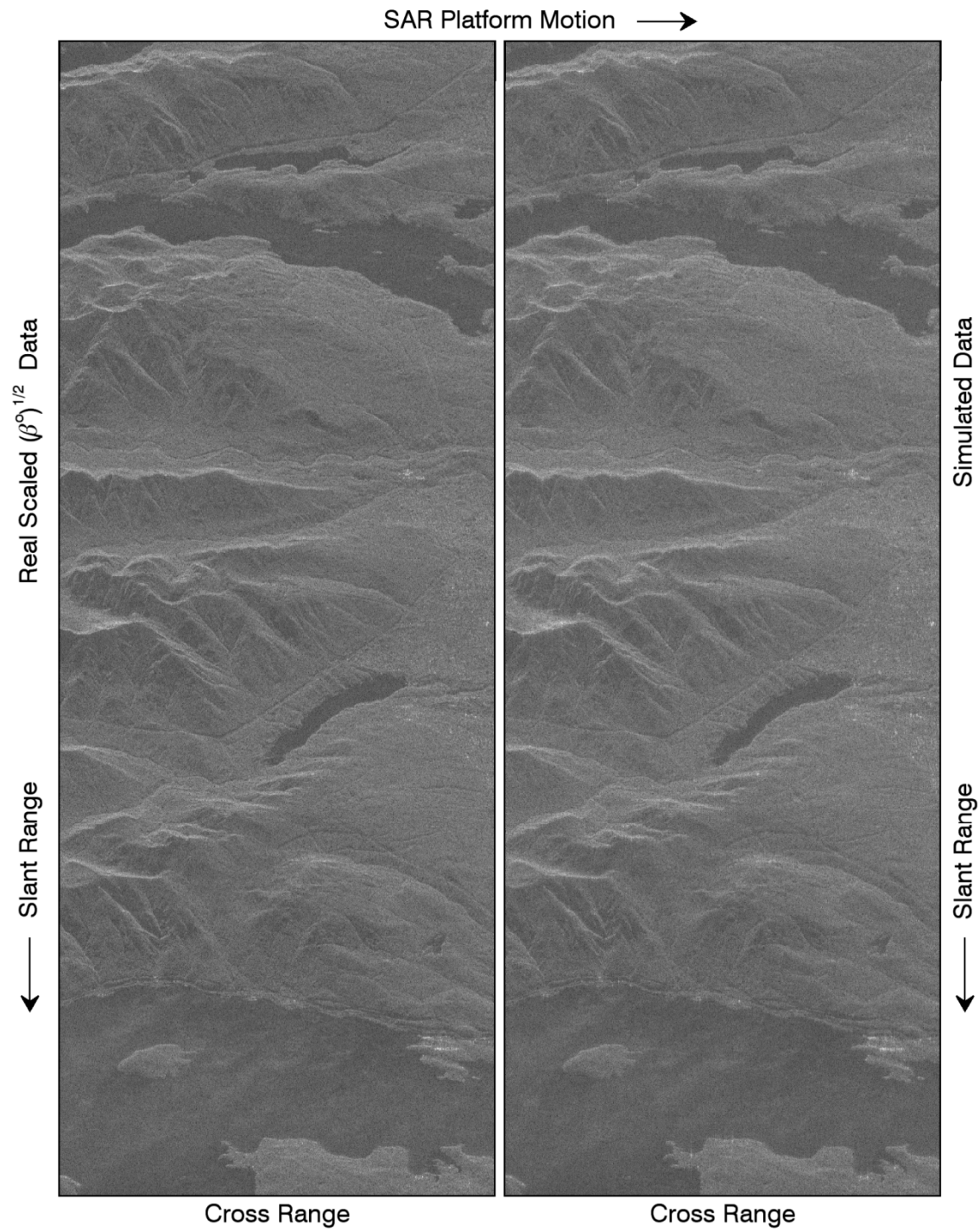


Figure 37: SAR images of the mountainous region north of Vancouver (cyan box in Figure 37) corresponding to the real, scaled $(\beta^0)^{1/2}$ data (left) and the simulated signals (right).

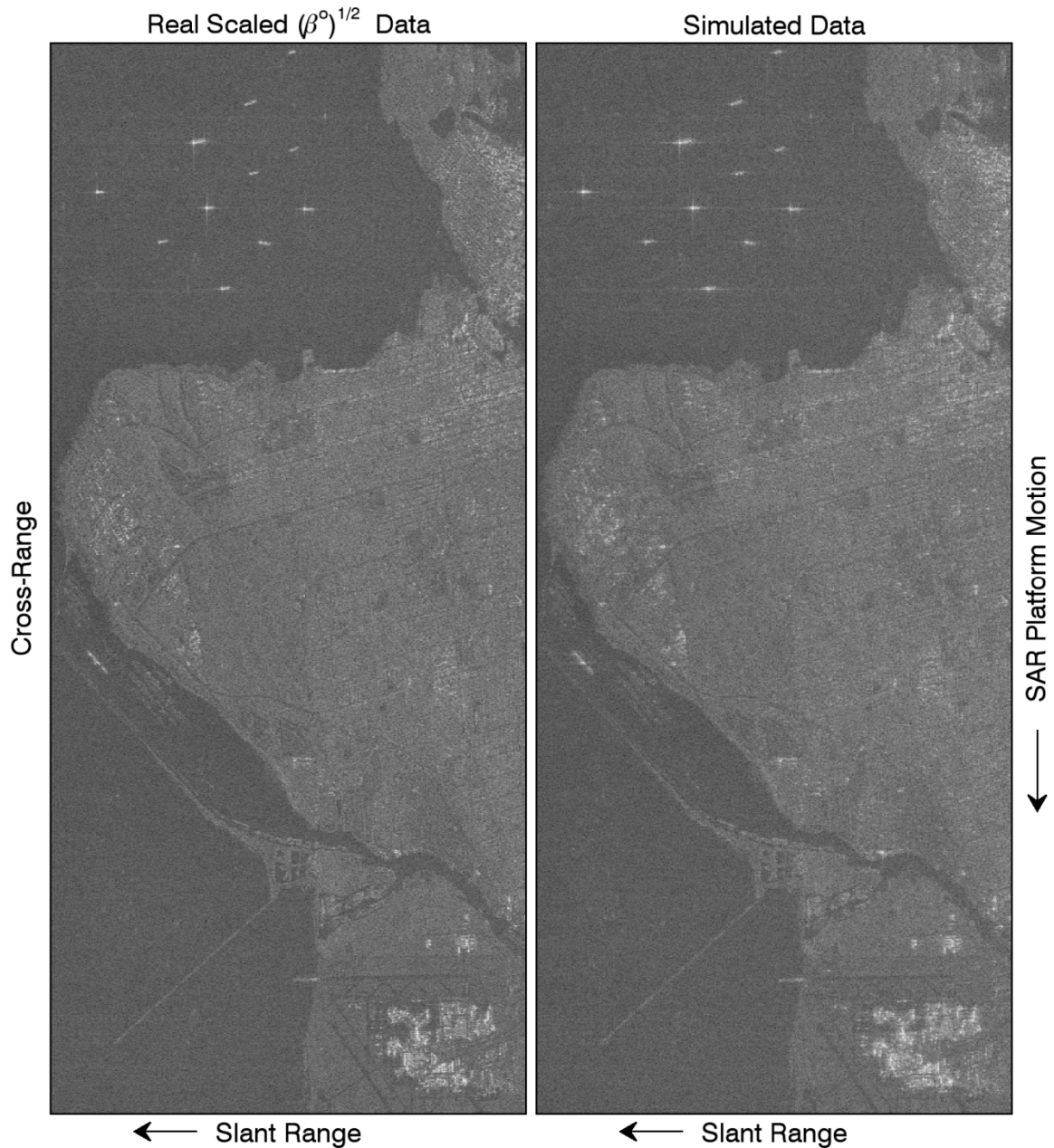


Figure 38: SAR images of the region extending from the Vancouver airport to Burrard Inlet (yellow box in Figure 37) corresponding to the real, scaled $(\beta^0)^{1/2}$ data (left) and the simulated signals (right).

7.2.2.3 Comparison of image statistics

In the Case 1, MODEX 1 comparisons, the image data corresponding to the real, scaled signals were generated using the exact same image formation processing as the image data for the simulated signals. Consequently, the image formation processing could not introduce a difference into the image data statistics. In the Case 2, W2 mode comparisons, however, the image formation processing of the real signals

was performed by MDA, whereas the simulated signals were processed with the RDA described in Annex B. This processing difference may cause the statistics of the real and simulated image data to be different. Regardless, a comparison of the image amplitude statistics and spatial autocorrelation for the uniform sea patch denoted with the orange box in Figure 36 is performed.

A zoomed view of the sea patch is shown in Figure 39. The corresponding amplitude PDFs and their associated moments are compared in Figure 40. The dashed black line in Figure 40 shows a Rayleigh distribution based on the mean value listed in the figure. The two PDFs agree well. However, the simulated data show consistently, slightly larger values in the tail region. The level of disagreement is not large and similar to that evident for the Case 1 sea patch comparisons. Overall, the image statistics of the inputted reflectivity field cannot be expected to match exactly the statistics of the simulated image since the SAR system impulse response has been applied again to create the simulated image. However, the agreement is expected to be good enough for the stated purpose of this simulation, which is jamming studies.

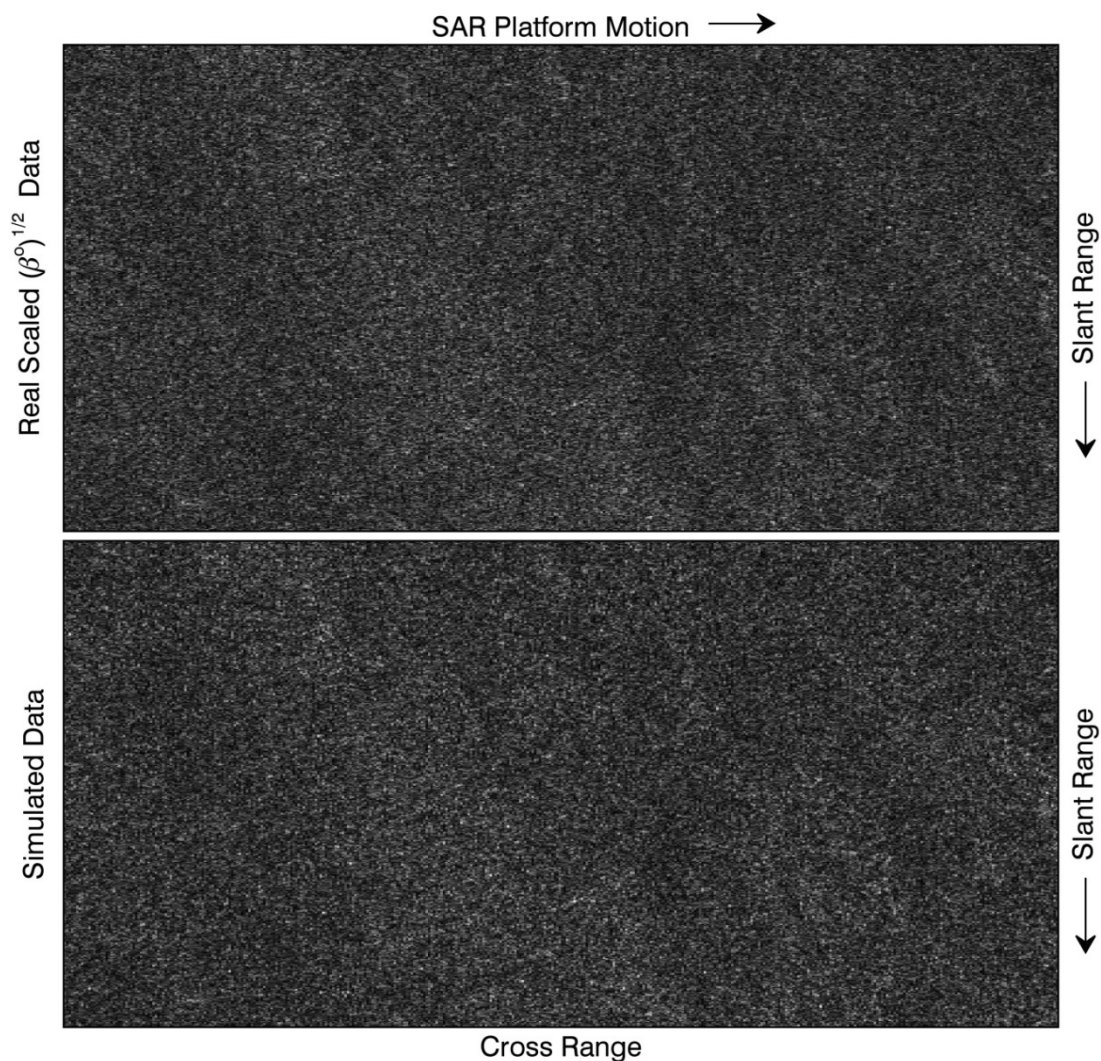


Figure 39: SAR images of a uniform sea patch (orange box in Figure 36) corresponding to the real, scaled $(\beta^0)^{1/2}$ data (upper) and the simulated signals (lower).

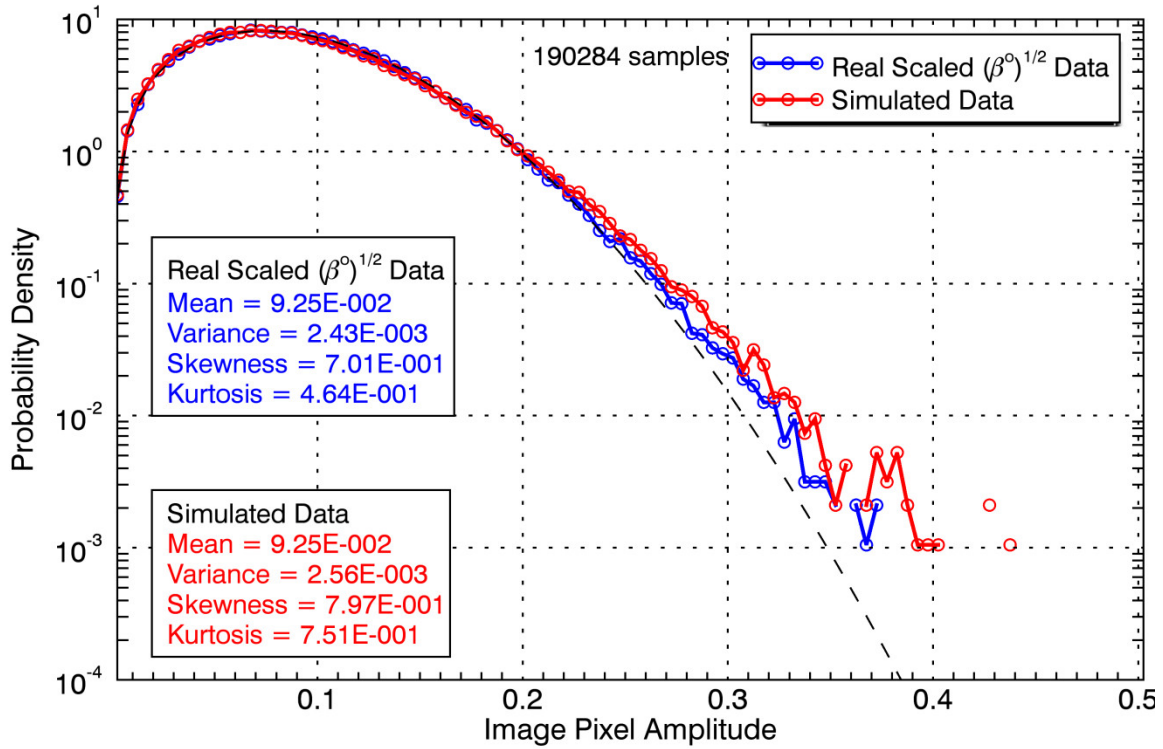


Figure 40: Image amplitude probability density functions for the uniform sea patch shown in Figure 39.

The surface views of the normalized image amplitude spatial autocorrelation functions corresponding to the Case 2 sea patch is shown in Figure 41. Again the surfaces corresponding to the real and simulated data are visually similar. Cuts along these surfaces, in the region of peak autocorrelation, for zero cross-range lag and zero slant-range lag are shown in Figure 42. Good agreement between the real and simulated data is found.

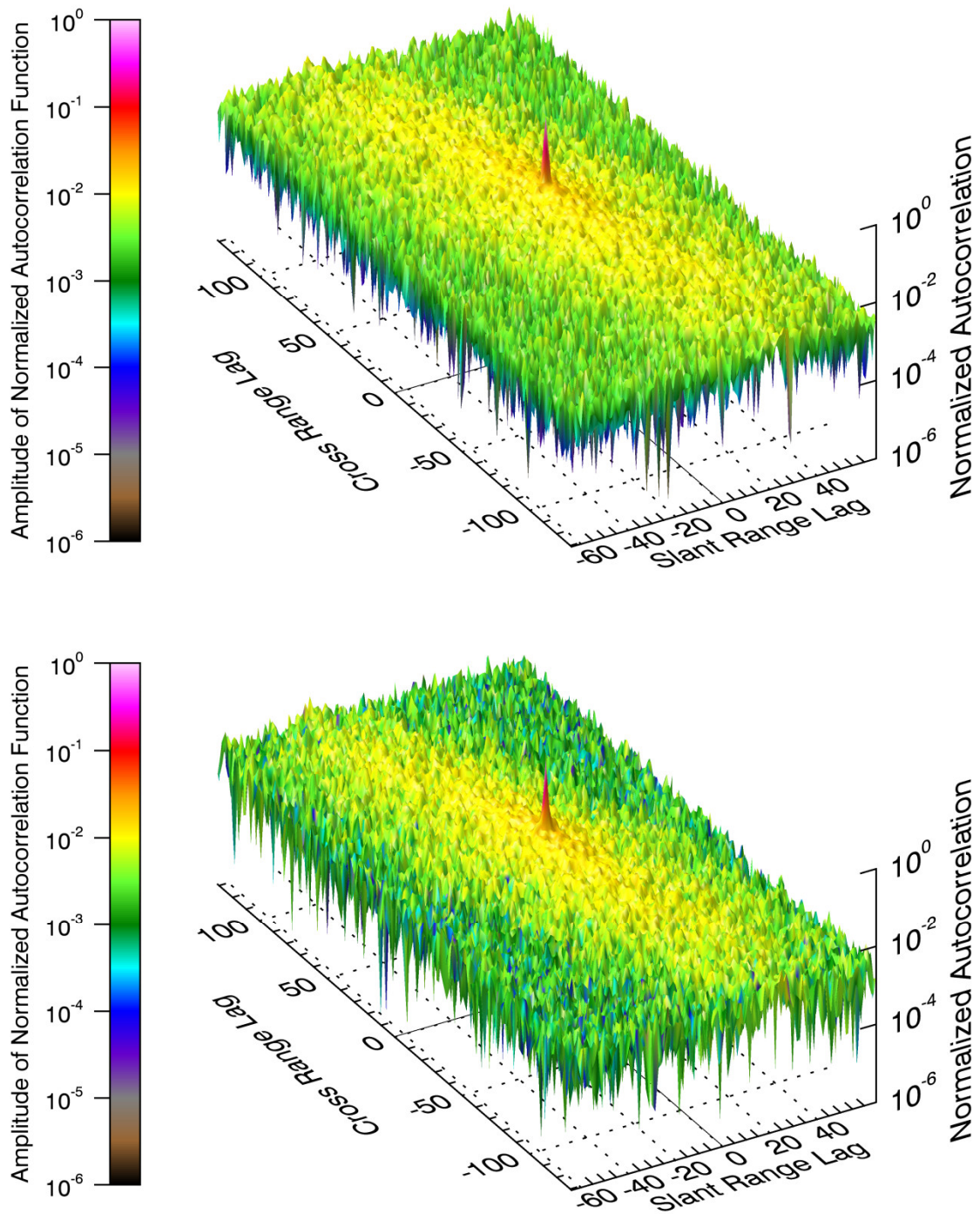


Figure 41: Normalized spatial autocorrelation functions corresponding to the real, scaled $(\beta^0)^{1/2}$ data (upper) and the simulated image data (lower) for the uniform sea patch (Figure 39).

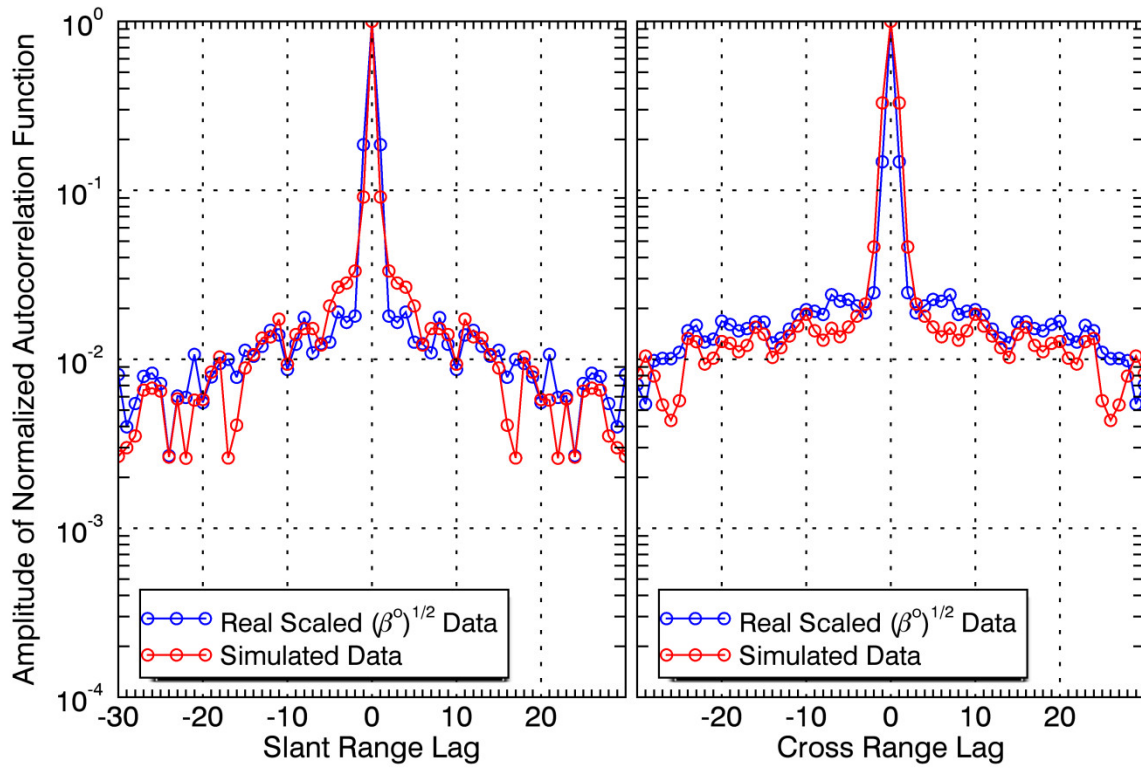


Figure 42: Normalized spatial autocorrelation functions at zero cross-range lag (left) and zero slant-range lag (right) for the uniform sea patch (Figure 39).

8 Summary and conclusions

This report has presented a method to simulate the raw in-phase and quadrature signals at the output of the analogue-to-digital converter within the receiver of a space-based SAR. The absolute magnitudes of these signals are calculated for specific scenario geometry within the simulated environment. This will allow the later introduction of jamming signals and for a quantitative assessment of the effects of the jamming as a function of the jammer parameters, such as transmitted power. The long term objective is to use the simulation to develop electronic protection measures that allow the space-based SAR to operate effectively in a contested environment.

This report has presented a detailed mathematical description of the approach used to simulate the received signals. These signals correspond to scatterers on the surface of the earth, radar system noise, and simulated test targets.

The accuracy of the simulation has been evaluated by comparing the properties of the simulated signals and their associated SAR image with theoretical expectations and with the signal properties of real data collected in the MODEX 1 mode by the RADARSAT-2 system. In addition, the properties of simulated image data were compared against those of a real image collected by RADARSAT-2 in the W2 mode. Good agreement was achieved in all aspects of the comparisons, which included comparisons of amplitude, phase, signal frequency, SAR impulse response, terrain effects, image amplitude statistics, and image amplitude spatial autocorrelation.

Comparisons of high-contrast portions of the real and simulated images allow the main weakness of the simulation approach to be observed. Since an actual SAR image is used to represent the reflectivity field on the surface of the Earth that is “measured” by the simulated SAR, the blurring of this reflectivity field caused by the impulse response of the processing system is effectively included twice in the simulated images. However, this is not a dominating effect in the cases considered, and a faithful representation of the real world signals corresponding to a specific SAR image is not the end objective of this research. The simulation is only required to provide realistic SAR signals and images, without and with the presence of jamming.

This simulation provides a method for approximating raw received signals corresponding to any RADARSAT-2 data collection. The favourable comparisons of real and simulated data provide confidence that the simulated signals effectively represent realistic SAR signals. Consequently, it is concluded that this simulation will address its stated purpose, which is to enable assessment of the vulnerability of space-based SAR to jamming for specific scenarios of interest and to aid in the development of methods for mitigating the effects of jamming.

References

- [1] Harness, R. S., Budge, M. C. (2014). A study on SAR noise jamming and false target insertion. In: SOUTHEASTCON, 2014, IEEE, March, 13–16, p. 8.
- [2] Dumper, K., Cooper, P. S., Wons, A. F., Condley, C. J., Tully, P. (1997). Spaceborne synthetic aperture radar and noise jamming. In: Radar 97 Conference, Institute of Electrical Engineers, Edinburgh, Scotland, October 14–16, pp. 411–414.
- [3] Franceschetti, G., Guida, R., Iodice, A., Riccio, D., Ruello, G. (2004). Efficient Simulation of Hybrid Stripmap/Spotlight SAR Raw Signals From Extended Scenes. *IEEE Transactions on Geoscience and Remote Sensing*, Vol. 42, No. 11, pp. 2385–2396.
- [4] Gierull, C., Ruppel, M. (1996). An end-to-end synthetic aperture radar simulator. In *Proceedings of EUSAR'96*, Königswinter, Germany, pp. 569–572.
- [5] Zhang, F., Hu, C., Li, W., Hu, W., Li, H. (2014). Accelerating time-domain SAR raw data simulation for large areas using multi-GPUs. *IEEE journal of selected topics in applied Earth observations and remote sensing*, Vol. 7, No. 9, pp. 3956–3966.
- [6] Franceschetti, G., Migliaccio, M., Riccio, D., Schirinzi, G. (1992). SARAS: A synthetic aperture radar (SAR) raw signal simulator. *IEEE Trans. Geosci. Remote Sens.*, 30, pp. 110–123.
- [7] Rahmanizadeh, A., Amini, J. (2017). An integrated method for simulation of synthetic aperture radar (SAR) raw data in moving target detection. *Remote Sensing*, 2017, 9, 1009; doi:10.3390/rs9101009, p. 19.
- [8] Allan, J. M., Collins, M. J., Gierull, C. (2010). Computational synthetic aperture radar (cSAR): a flexible signal simulator for multichannel SAR systems. *Can. J. Remote Sensing*, Vol. 36, No. 4, pp. 345–360.
- [9] Liu, B., He, Y. (2016). SAR raw data simulation for ocean scenes using inverse omega-K algorithm. *IEEE Transactions on Geoscience and Remote Sensing*, Vol. 54, No. 10, pp. 6151–6169.
- [10] Mori, A., De Vita, F. (2004). A time-domain raw signal simulator for interferometric SAR. *IEEE Transactions on Geoscience and Remote Sensing*, Vol. 42, No. 9, pp. 1811–1817.
- [11] Skolnik, M. I. (2001). *Introduction to radar systems*, 3rd ed. McGraw-Hill, Inc., p. 772.
- [12] Chiu, S., Livingston, C., Sikaneta, I., Gierull, C., Beaulne, P. (2008). RADARSAT-2 moving object detection experiment (MODEX). In *Proceedings of IEEE International Geoscience and remote sensing symposium*, July 7–11, Boston, MA, USA, pp. I-13–I-16.
- [13] MacDonald, Dettwiler and Associates Ltd. (2014). RADARSAT-2 product format definition. RN-RP-51-2713, Issue 1/12: July 15, 2014.

- [14] Cumming, I. G., Wong, F. H. (2005). Digital processing of synthetic aperture radar data. Artech House, Inc., Massachusetts, p. 625.
- [15] MacDonald, Dettwiler and Associates Ltd. (2015). RADARSAT-2 application look-up tables (LUTs). PG-TN-52-7196, Issue 1/3: October 16, 2015.
- [16] Allan, J. M., Collins, M. J. (2012). The generation of correlated gamma distributed random fields for the simulation of synthetic aperture radar images. Society for Industrial and Applied Mathematics Journal on Imaging Sciences, DOI: 10.1137/100801822, p. 28.
- [17] Chen, W., Young, A. (2011). Multi-domain / multiple-system high fidelity modeling and simulation (HFM&S) for R&D of radar electronic warfare system concepts. (DRDC Ottawa TM 2011-207), Technical Memorandum, Defence R&D Canada – Ottawa.
- [18] Nathanson, F. E. (1999). Radar design principles. 2nd edition, Scitech Publishing, Inc., Mendham, New Jersey, p. 720.
- [19] Doviak, R. J., Zrnić, D. S. (1993). Doppler radar and weather observations. Academic Press, p. 562.
- [20] Blake, L. V. (1986). Radar range-performance analysis. Artech House, Inc., Massachusetts, p. 443.
- [21] Orfanidis, S. J. (2016). Electromagnetic Waves and Antennas. ECE Department, Rutgers University. Available from: <http://ecweb1.rutgers.edu/~orfanidi/ewa>, p. 819. Accessed: November 5, 2018.
- [22] Raney, R. K., Freeman, T., Hawkins, R. W., Bamler, R. (1994). A plea for radar brightness. In: International Geoscience and Remote Sensing Symposium, 1994, Surface and Atmospheric Remote Sensing: Technologies, Data Analysis and Interpretation, pp. 1090–1092.
- [23] MacDonald, Dettwiler and Associates Ltd. (2015). Geolocation of RADARSAT-2 georeferenced products. RN-TN-53-0076, Issue 1/3: April 8, 2015.
- [24] Jordan, E. C., Balmain, K. G. (1968). Electromagnetic waves and radiating systems. 2nd ed. Prentice-Hall, Inc., Englewood Cliffs, New Jersey, p. 753.
- [25] Thomson, A. D. (1999). Simulation of weather clutter as measured by an X-band phased array radar. (DREO TR 1999-077). Defence Research Establishment Ottawa.
- [26] Livingstone, C. E., Sikaneta, I., Gierull, C., Chiu, S., Beaulne, P. (2005). RADARSAT-2 system and mode description. In: Integration of Space-Based Assets Within Full Spectrum Operations (pp. 15-1–15-22). Meeting Proceedings RTO-MP-SCI-150, Paper 15. Neuilly-sur-Seine, France: RTO.
- [27] Goodman, J. W. (1985). Statistical Optics. John Wiley & Sons, Inc., p. 550.

Annex A Earth intersection points

Calculation of the signals received from a reflectivity field that is constrained to the surface of the earth requires the geometry associated with the intersection of the radar beam with the earth's surface to be determined. This requirement arose in Section 3.2 in terms of the need to determine which discrete scatterers representing the reflectivity field are within the radar resolution volume. The radar resolution volume for a range bin at \vec{r}_m will be constrained within the range interval $r_m - c T_p/4 \leq r \leq r_m + c T_p/4$. Therefore, for example, the points $(r_m - c T_p/4, \phi_b, \theta_e(r_m - c T_p/4, \phi_b))$ and $(r_m + c T_p/4, \phi_b, \theta_e(r_m + c T_p/4, \phi_b))$ will be Earth intersection points. Similarly, in Section 3.3 all points $(r_i, \phi_{iq}, \theta_e(r_i, \phi_{iq}))$ are Earth intersection points. In general, the coordinates of any point (r_I, θ_I, ϕ_I) that lies on the surface of the earth will be related such that $\theta_I = \theta_e(r_I, \phi_I)$, where θ_e is a function that describes the dependence of the polar angle to the earth's surface on range and azimuth, and the subscript I is used to denote an earth intersection point. This relationship will depend upon the shape of the earth, the satellite orbit, the position of the satellite within its orbit, the yaw, roll, and pitch of the satellite, the antenna configuration, and the pointing direction of the radar beam axis. This annex describes a method for evaluating $\theta_e(r_I, \phi_I)$.

Geometrically, a specific r_I value represents a constraint such that the intersection point must lie on the surface of a sphere of radius r_I . A specific value of ϕ_I represents the constraint that the intersection point must lie within a plane. Together, these two constraints dictate that the intersection point must lie along a circle of radius r_I within the ϕ_I plane. A portion of this circle is illustrated in Figure A.1 as the green curve rising upward from the surface of the earth. The final constraint that determines the earth intersection point is the equation describing the surface of the earth. For all calculations in this document the surface of the earth is approximated using the WGS 84 ellipsoid.

The three constraints discussed above can be written mathematically as three equations with the three variables r_I , θ_I , and ϕ_I , or in their Cartesian equivalents. However, the ellipsoid describing the earth's surface is most easily written in a Cartesian coordinate system with its origin located at the centre of the earth. The transformation of this equation into a radar-centred coordinate system makes its form too complex to allow for a closed-form solution to the three equations to be found. A numerical solution to the set of equations was achieved successfully. However, the computer execution time required for this solution is too long to allow all of the I and Q values required to form a SAR image to be calculated in an acceptable amount of time. The output of the numerical solution was also found to be sensitive to the initial guess values in an unpredictable way. Therefore, an alternate iterative solution is employed.

The Earth intersection point problem can be summarized as: given known values of r_I and ϕ_I in the receive antenna coordinate system, find the value of θ_I such that (r_I, θ_I, ϕ_I) is an earth intersection point. As discussed in the previous paragraph a closed-form solution to this problem could not be found. However, if both θ_I and ϕ_I are known, then a closed-form solution exists for the determination of r_I such that (r_I, θ_I, ϕ_I) is an intersection point. Therefore, the iterative solution to the earth intersection point problem will employ an algorithm that searches through θ_I values, while maintaining ϕ_I fixed, until the calculated path length from the transmit antenna to the intersection point to the receive antenna matches the desired value, r_I as determined by the radar sampling time, to within a chosen tolerance (1 cm).

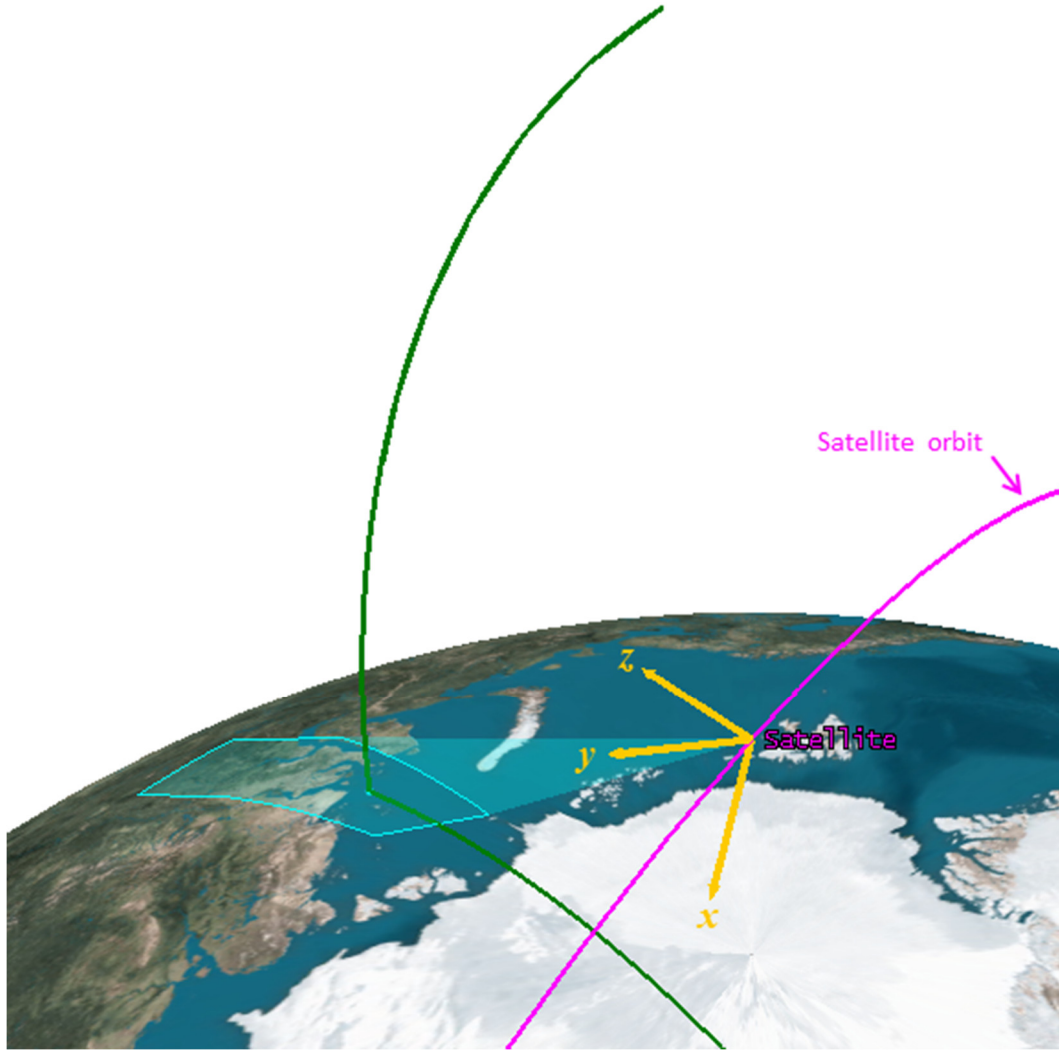


Figure A.1: Earth intersection geometry. The magenta line shows the satellite orbit. The yellow axes represent a Cartesian coordinate system centred at the radar antenna. The radar beam is shown in translucent blue. The green line extending upward from the surface of the earth represents the circle dictated by the range and azimuth constraints.

A.1 Earth intersection point calculation for known pointing direction

Figure A.2 shows the geometry of the earth intersection point problem for the case when both θ_I and ϕ_I are known. The displayed set of coordinate axes represent the earth-centred fixed coordinate system, X - Y - Z , discussed in Section 3.1. The coordinates of the intersection point in the earth-centred fixed system are given by the vector \vec{P} . The coordinates of the phase centre of the radar receive antenna are described by the vector \vec{A} . The vector \vec{U} has a length of 1 and points in the direction from the radar antenna to the intersection point. The scaling parameter d is defined such that

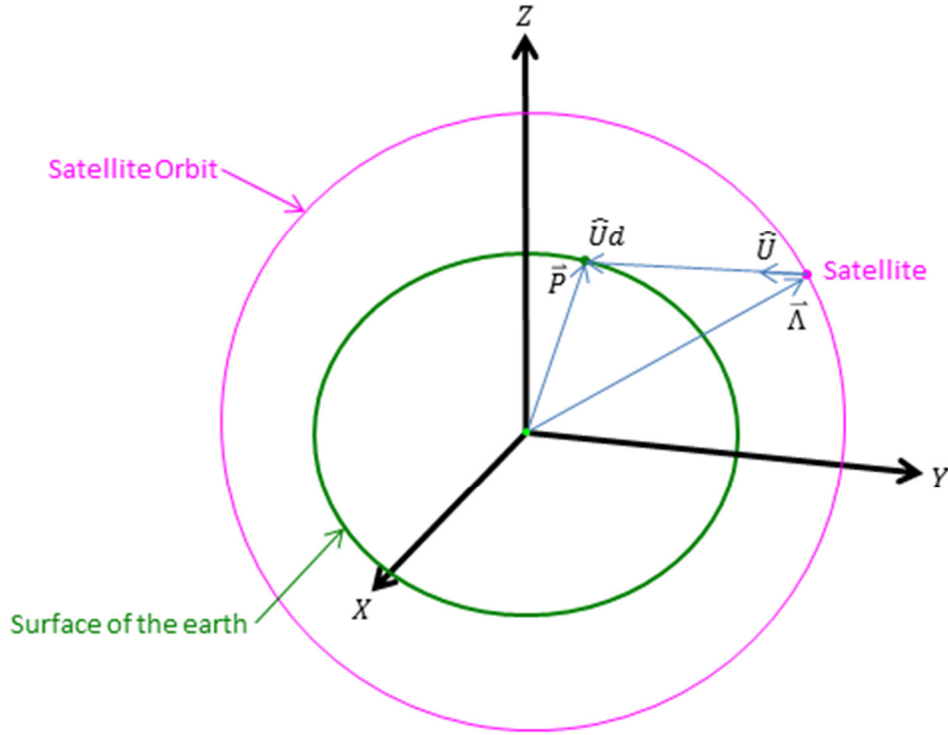


Figure A.2: Vectors associated with the solution to the earth intersection point problem.

$$\vec{P} = \vec{\Lambda} + \vec{U}d \quad (\text{A.1})$$

Any Earth intersection point $\vec{P} = (P_X, P_Y, P_Z)$ must satisfy the equation of the surface of the earth, i.e.,

$$\frac{P_X^2}{R_e^2} + \frac{P_Y^2}{R_e^2} + \frac{P_Z^2}{R_p^2} = 1 \quad (\text{A.2})$$

Using Equation (A.1) to substitute the coordinates of the receive antenna phase centre, $(\Lambda_X, \Lambda_Y, \Lambda_Z)$, and the known pointing direction within the radar beam, (U_X, U_Y, U_Z) , into Equation (A.2) and rearranging results in a quadratic equation in d ,

$$d^2 \left(\frac{U_X^2}{R_e^2} + \frac{U_Y^2}{R_e^2} + \frac{U_Z^2}{R_p^2} \right) + d \left(\frac{2\Lambda_X U_X}{R_e^2} + \frac{2\Lambda_Y U_Y}{R_e^2} + \frac{2\Lambda_Z U_Z}{R_p^2} \right) + \left(\frac{\Lambda_X^2}{R_e^2} + \frac{\Lambda_Y^2}{R_e^2} + \frac{\Lambda_Z^2}{R_p^2} - 1 \right) = 0 \quad (\text{A.3})$$

If the intersection point is such that the vector $\vec{U}d$ is not tangential to the surface of the earth, then the solution to Equation (A.3) will provide two real roots. The smaller root will give the coordinates of the intersection point in the earth-centred fixed coordinate system as

$$\vec{P} = (\Lambda_X + U_X d, \Lambda_Y + U_Y d, \Lambda_Z + U_Z d) \quad (\text{A.4})$$

To use Equations (A.3) and (A.4) to solve for the intersection point, the components of the direction vector \vec{U} in the earth-centred fixed system, (U_X, U_Y, U_Z) , must first be determined as a function of the pointing direction in the receive antenna coordinate system, (θ_I, ϕ_I) .

A.2 Direction vector transformation

Given the coordinate transformations defined in Section 3.1, the direction vector corresponding to (θ_I, ϕ_I) can now be transformed from the receive antenna coordinate system to the earth-centred fixed coordinate system. This is done by transforming the end point of the direction vector and then recalculating the direction vector as the difference between the transformed point and the location of the receive antenna phase centre.

The direction vector can be written in the receive antenna coordinate system as

$$\hat{u} = \begin{bmatrix} \sin \theta_I \cos \phi_I \\ \sin \theta_I \sin \phi_I \\ \cos \theta_I \end{bmatrix} \quad (\text{A.5})$$

Transformation of the end point of the direction vector to the x' - y' - z' coordinate system is given by

$$\begin{bmatrix} u'_x \\ u'_y \\ u'_z \end{bmatrix} = \mathbf{A}^{-1} \begin{bmatrix} \sin \theta_I \cos \phi_I \\ \sin \theta_I \sin \phi_I + \Delta y \\ \cos \theta_I \end{bmatrix} \quad (\text{A.6})$$

Transformation to the x'' - y'' - z'' is performed by the mapping

$$\begin{bmatrix} u''_x \\ u''_y \\ u''_z \end{bmatrix} = \begin{bmatrix} u'_y \\ u'_z \\ u'_x \end{bmatrix} \quad (\text{A.7})$$

Transformation to the X''' - Y''' - Z''' frame is given by the mapping

$$\begin{bmatrix} U_X''' \\ U_Y''' \\ U_Z''' \end{bmatrix} = \begin{bmatrix} -u_x'' \\ u_y'' \\ S_Z''' - u_z'' \end{bmatrix} \quad (\text{A.8})$$

where S_Z''' is the Z-component of $\vec{S}''' = \mathbf{E}_{Z''} [\mathbf{E}_{Y'} (\mathbf{E}_Z \vec{S})]$, and \vec{S} is the vector from the earth's centre to the centre of the satellite or the transmit antenna phase centre.

The direction vector end point in the earth-centred fixed coordinate frame can then be calculated as

$$\begin{bmatrix} U_X \\ U_Y \\ U_Z \end{bmatrix} = \mathbf{E}_{Z'}^{-1} \left\{ \mathbf{E}_{Y'}^{-1} \left(\mathbf{E}_{Z''}^{-1} \begin{bmatrix} U_X''' \\ U_Y''' \\ U_Z''' \end{bmatrix} \right) \right\} \quad (\text{A.9})$$

Finally, the direction vector is calculated as

$$\hat{U} = \begin{bmatrix} U_X - \Lambda_X \\ U_Y - \Lambda_Y \\ U_Z - \Lambda_Z \end{bmatrix} \quad (\text{A.10})$$

and this enables an earth intersection point to be calculated using Equation (A.4).

A.3 Algorithm initiation

The algorithm for iteratively calculating Earth intersection points for known values of r_l and ϕ_l searches through values of θ . Therefore, reasonable guesses for the intersection point and a polar angle bound over which to search are required to initiate the algorithm.

The guess calculations begin by calculating an initial guess direction vector using the approximation that the earth is a sphere. The local Earth radius at the satellite location, R_L , can be calculated by first writing the components of the intersection point vector as a function of the radius

$$\begin{aligned} \sqrt{P_x^2 + P_y^2} &= R_L \sin \vartheta'_s \\ P_z &= R_L \cos \vartheta'_s \end{aligned} \quad (\text{A.11})$$

and then substituting these values into the equation of the earth's surface (Equation (A.2)) and rearranging, i.e.,

$$R_L = \sqrt{\frac{R_e^2 R_p^2}{R_p^2 \sin^2 \vartheta'_s + R_e^2 \cos^2 \vartheta'_s}} \quad (\text{A.12})$$

The initial guess polar angle is approximated as a polar angle with respect to the transmit antenna phase centre and assumed to be good enough with respect to the receive antenna phase centre. Assuming that the earth is a sphere, it is straightforward to calculate the initial guess polar angle to the intersection point, θ''_g , in the x'' - y'' - z'' coordinate frame, since this coordinate frame has an axis aligned with the nadir direction. That is, using the law of cosines,

$$\theta''_g = \cos^{-1} \left(\frac{r_I^2 + S_Z''^2 - R_L^2}{2r_I S_Z''} \right) \quad (\text{A.13})$$

Note that this calculation uses the desired range to the intersection point, r_I , in the receive antenna coordinate system, which is acceptable at this point since only an approximate initial guess is being calculated. The z'' -coordinate of the initial guess intersection point can then be calculated in the x'' - y'' - z'' coordinate frame as

$$z''_g = r_I \cos \theta''_g \quad (\text{A.14})$$

The known azimuth places a constraint on the Cartesian coordinates of the guess intersection point in the receive and transmit antenna coordinate systems, i.e.,

$$y_g = x_g \tan \phi_I = x_{Tg} \tan \phi_I = y_{Tg} - \Delta y \quad (\text{A.15})$$

This constraint can be transformed into the x'' - y'' - z'' coordinate frame. The relation between the Cartesian coordinates of the guess intersection point in the x_T - y_T - z_T and x'' - y'' - z'' coordinate frames is given by

$$\begin{bmatrix} x_{Tg} \\ y_{Tg} \\ z_{Tg} \end{bmatrix} = \mathbf{A} \begin{bmatrix} z''_g \\ x''_g \\ y''_g \end{bmatrix} \quad (\text{A.16})$$

Expanding Equation (A.16) and substituting into Equation (A.15) gives the azimuth constraint as a linear equation, i.e.,

$$x''_g C_x + y''_g C_y + z''_g C_z - \Delta y = 0 \quad (\text{A.17})$$

where

$$\begin{aligned}
C_x &= \cos \alpha \cos \gamma - \sin \alpha \sin \beta \sin \gamma - \sin \alpha \cos \gamma \tan \phi_I - \cos \alpha \sin \beta \sin \gamma \tan \phi_I \\
C_y &= \cos \alpha \sin \gamma + \sin \alpha \sin \beta \cos \gamma - \sin \alpha \sin \gamma \tan \phi_I + \cos \alpha \sin \beta \cos \gamma \tan \phi_I \\
C_z &= -\sin \alpha \cos \beta - \cos \alpha \cos \beta \tan \phi_I
\end{aligned} \tag{A.18}$$

Another constraint relating the Cartesian coordinates is dictated by the range, r_I , i.e.,

$$x_g''^2 + y_g''^2 + z_g''^2 = r_I^2 \tag{A.19}$$

Equations (A.17) and (A.19) can be manipulated to create a quadratic equation in x_g'' , i.e.,

$$\begin{aligned}
x_g''^2 \left(1 + \frac{C_x^2}{C_y^2} \right) + x_g'' \left(\frac{2z_g'' C_x C_z}{C_y^2} - 2C_x \Delta y \right) + \dots \\
\text{for } C_y \neq 0 \tag{A.20} \\
\dots \left[\frac{z_g''^2 C_z^2}{C_y^2} + z_g''^2 - r_I^2 - \frac{2z_g'' C_z \Delta y}{C_y^2} + \frac{(\Delta y)^2}{C_y^2} \right] = 0
\end{aligned}$$

The two solutions of Equation (A.20) can be substituted into Equation (A.17) to obtain two values for y_g'' . In the case where $C_y = 0$, manipulation of Equations (A.17) and (A.19) gives

$$\begin{aligned}
x_g'' &= \frac{-z_g'' C_z}{C_x} + \frac{\Delta y}{C_x} \\
y_g'' &= \pm \sqrt{r_I^2 - z_g''^2 \left(1 + \frac{C_z^2}{C_x^2} \right) + \frac{2z_g'' C_z \Delta y}{C_x^2} - \frac{(\Delta y)^2}{C_x^2}} \tag{A.21} \\
\text{for } C_y &= 0
\end{aligned}$$

which also has two solutions. The correct solution in either case ($C_y \neq 0$ or $C_y = 0$) is determined by transforming the guess intersection point solutions back to the transmit antenna coordinate system, calculating their corresponding polar angles, and testing to see which solution has a polar angle that is closest to the radar antenna boresight. Once this is completed, the initial guess intersection point, (x_{Tg}, y_{Tg}, z_{Tg}) , will be determined in the transmit antenna coordinate system.

The guess polar angle in the transmit antenna coordinate system is assumed to be good enough as a guess polar angle in the receive antenna coordinate system. Consequently, the coordinates for the initial guess intersection point can be estimated in the receive centre coordinate system as

$$\begin{aligned}
x_g &= r_I \sin \theta_{Tg} \cos \phi_I \\
y_g &= r_I \sin \theta_{Tg} \sin \phi_I \\
z_g &= r_I \cos \theta_{Tg}
\end{aligned} \tag{A.22}$$

where

$$\theta_{Tg} = \cos^{-1} \left(\frac{z_{Tg}}{\sqrt{x_{Tg}^2 + y_{Tg}^2 + z_{Tg}^2}} \right) \tag{A.23}$$

The initial guess coordinates of Equation (A.22) can then be transformed to the earth-centred fixed coordinate system using the transformations defined in Section 3.1, i.e.,

$$\begin{bmatrix} X_g \\ Y_g \\ Z_g \end{bmatrix} = \mathbf{E}_{Z'}^{-1} \left\{ \mathbf{E}_Y^{-1} \left(\mathbf{E}_{Z''}^{-1} \begin{bmatrix} X_g''' \\ Y_g''' \\ Z_g''' \end{bmatrix} \right) \right\} \tag{A.24}$$

where

$$\begin{bmatrix} X_g''' \\ Y_g''' \\ Z_g''' \end{bmatrix} = \begin{bmatrix} -x_g'' \\ y_g'' \\ S_Z''' - z_g'' \end{bmatrix} \tag{A.25}$$

$$\begin{bmatrix} x_g'' \\ y_g'' \\ z_g'' \end{bmatrix} = \begin{bmatrix} y_g' \\ z_g' \\ x_g' \end{bmatrix} \tag{A.26}$$

$$\begin{bmatrix} x_g' \\ y_g' \\ z_g' \end{bmatrix} = \mathbf{A}^{-1} \begin{bmatrix} x_g \\ y_g + \Delta y \\ z_g \end{bmatrix} \tag{A.27}$$

This allows the initial guess direction vector to be calculated as

$$\hat{U}_g = \begin{bmatrix} \frac{X_g - \Lambda_X}{\sqrt{(X_g - \Lambda_X)^2 + (Y_g - \Lambda_Y)^2 + (Z_g - \Lambda_Z)^2}} \\ \frac{Y_g - \Lambda_Y}{\sqrt{(X_g - \Lambda_X)^2 + (Y_g - \Lambda_Y)^2 + (Z_g - \Lambda_Z)^2}} \\ \frac{Z_g - \Lambda_Z}{\sqrt{(X_g - \Lambda_X)^2 + (Y_g - \Lambda_Y)^2 + (Z_g - \Lambda_Z)^2}} \end{bmatrix} \quad (\text{A.28})$$

where

$$\bar{\Lambda} = \begin{bmatrix} \Lambda_X \\ \Lambda_Y \\ \Lambda_Z \end{bmatrix} = \mathbf{E}_{Z'}^{-1} [\mathbf{E}_{Y''}^{-1} (\mathbf{E}_{Z'''}^{-1} \bar{\Lambda}''')] \quad (\text{A.29})$$

and

$$\bar{\Lambda}''' = \begin{bmatrix} -\lambda'_y \\ \lambda'_z \\ S_{Z'''} - \lambda'_x \end{bmatrix} \quad (\text{A.30})$$

$$\begin{bmatrix} \lambda'_x \\ \lambda'_y \\ \lambda'_z \end{bmatrix} = \mathbf{A}^{-1} \begin{bmatrix} 0 \\ \Delta y \\ 0 \end{bmatrix} \quad (\text{A.31})$$

The initial guess direction vector (Equation (A.28)) can now be used in the equations of Section A.1 to calculate an initial guess intersection point, $\vec{P}_g = (X_g, Y_g, Z_g)$ in the earth-centred fixed coordinate system.

The iterative algorithm also requires a polar angle interval that can be used to interpolate a new guess intersection point. This value will be calculated as the difference in polar angles corresponding to the desired range and the current guess range, assuming a spherical Earth. That is, using the law of cosines,

$$\Delta\theta = 2 \left| \cos^{-1} \left(\frac{r_I^2 + \Lambda_{Z'''}^2 - R_L^2}{2r_I \Lambda_{Z'''}^2} \right) - \cos^{-1} \left(\frac{r_g^2 + \Lambda_{Z'''}^2 - R_L^2}{2r_g \Lambda_{Z'''}^2} \right) \right| \quad (\text{A.32})$$

where r_g can be calculated as

$$r_g = \sqrt{(\Lambda_X - X_g)^2 + (\Lambda_Y - Y_g)^2 + (\Lambda_Z - Z_g)^2} \quad (\text{A.33})$$

Similarly, the range from the transmit antenna phase centre to the initial guess point is given by

$$r_{Tg} = \sqrt{(S_X - X_g)^2 + (S_Y - Y_g)^2 + (S_Z - Z_g)^2} \quad (\text{A.34})$$

If the path length associated with the guess intersection point, $(r_{Tg} + r_g)/2$, does not match the desired range, r_I , to the required accuracy, then the iteration will begin using the two initiating quantities \vec{P}_g and $\Delta\theta$.

A.4 Iteration

The algorithm for calculating earth intersection points for known values of r_I and ϕ_I proceeds as follows:

Step 1: Transform the current guess intersection point coordinates in the earth-centred fixed system, (X_g, Y_g, Z_g) , into coordinates in the receive antenna system, (x_g, y_g, z_g) .

Step 2: calculate the polar angle bounds, $[\theta_{gL}, \theta_{gU}]$ over which to interpolate a new guess intersection point:

$$\begin{aligned} \theta_{gL} &= \cos^{-1} \left(\frac{z_g}{\sqrt{x_g^2 + y_g^2 + z_g^2}} \right) - \Delta\theta \\ \theta_{gU} &= \cos^{-1} \left(\frac{z_g}{\sqrt{x_g^2 + y_g^2 + z_g^2}} \right) + \Delta\theta \end{aligned} \quad (\text{A.35})$$

Step 3: calculate direction vectors for each of the polar angle bounds:

$$\hat{u}_{gL} = \begin{bmatrix} \sin \theta_{gL} \cos \phi_I \\ \sin \theta_{gL} \sin \phi_I \\ \cos \theta_{gL} \end{bmatrix}$$

$$\hat{u}_{gU} = \begin{bmatrix} \sin \theta_{gU} \cos \phi_I \\ \sin \theta_{gU} \sin \phi_I \\ \cos \theta_{gU} \end{bmatrix}$$
(A.36)

Step 4: transform the direction vectors for each polar angle bound into the Earth-centred fixed coordinate system using the transformations defined in Section 3.1.

Step 5: calculate guess intersection points, (X_{gL}, Y_{gL}, Z_{gL}) and (X_{gU}, Y_{gU}, Z_{gU}) , for each direction vector using the equations of Section A.1.

Step 6: calculate the longitudes, Φ , and latitudes, Θ , for each direction vector:

$$\Phi_{gL} = \tan^{-1} \left(\frac{Y_{gL}}{X_{gL}} \right)$$

$$\Phi_{gU} = \tan^{-1} \left(\frac{Y_{gU}}{X_{gU}} \right)$$

$$\Theta_{gL} = \tan^{-1} \left(\frac{\tan \Theta_{gLc}}{1 - e_E^2} \right)$$

$$\Theta_{gU} = \tan^{-1} \left(\frac{\tan \Theta_{gUc}}{1 - e_E^2} \right)$$
(A.37)
(A.38)

where the geocentric latitudes are given by

$$\begin{aligned}\Theta_{gLc} &= 90^\circ - \cos^{-1} \left(\frac{Z_{gL}}{\sqrt{X_{gL}^2 + Y_{gL}^2 + Z_{gL}^2}} \right) \\ \Theta_{gUc} &= 90^\circ - \cos^{-1} \left(\frac{Z_{gU}}{\sqrt{X_{gU}^2 + Y_{gU}^2 + Z_{gU}^2}} \right)\end{aligned}\tag{A.39}$$

Step 7: linearly interpolate new guesses for the intersection point longitude and latitude:

$$\begin{aligned}\Phi_g &= \frac{\left(r_i - \frac{r_{TgL} + r_{gL}}{2}\right)(\Phi_{gU} - \Phi_{gL})}{\left(\frac{r_{TgU} + r_{gU}}{2}\right) - \left(\frac{r_{TgL} + r_{gL}}{2}\right)} + \Phi_{gL} \\ \Theta_g &= \frac{\left(r_i - \frac{r_{TgL} + r_{gL}}{2}\right)(\Theta_{gU} - \Theta_{gL})}{\left(\frac{r_{TgU} + r_{gU}}{2}\right) - \left(\frac{r_{TgL} + r_{gL}}{2}\right)} + \Theta_{gL}\end{aligned}\tag{A.40}$$

where

$$\begin{aligned}r_{TgL} &= \sqrt{(S_X - X_{gL})^2 + (S_Y - Y_{gL})^2 + (S_Z - Z_{gL})^2} \\ r_{gL} &= \sqrt{(\Lambda_X - X_{gL})^2 + (\Lambda_Y - Y_{gL})^2 + (\Lambda_Z - Z_{gL})^2} \\ r_{TgU} &= \sqrt{(S_X - X_{gU})^2 + (S_Y - Y_{gU})^2 + (S_Z - Z_{gU})^2} \\ r_{gU} &= \sqrt{(\Lambda_X - X_{gU})^2 + (\Lambda_Y - Y_{gU})^2 + (\Lambda_Z - Z_{gU})^2}\end{aligned}\tag{A.41}$$

Step 8: calculate the Cartesian coordinates of the new guess intersection point in the earth-centred fixed coordinate system:

$$Z_g = \sqrt{\frac{1}{\frac{\tan^2(90^\circ - \Theta_{gc})}{R_e^2} + \frac{1}{R_p^2}}} \quad (\text{A.42})$$

$$X_g = \begin{cases} -\sqrt{Z_g^2 \cos^2 \Phi_g \tan^2(90^\circ - \Theta_{gc})} & \text{for } 90^\circ \leq \Phi_g < 270^\circ \\ +\sqrt{Z_g^2 \cos^2 \Phi_g \tan^2(90^\circ - \Theta_{gc})} & \text{for } \Phi_g < 90^\circ \text{ or } \Phi_g \geq 270^\circ \end{cases} \quad (\text{A.43})$$

$$Y_g = X_g \tan \Phi_g \quad (\text{A.44})$$

where the geocentric latitude is given by

$$\Theta_{gc} = \tan^{-1}[(1 - e_E^2) \tan \Theta_g] \quad (\text{A.45})$$

Step 9: calculate a new bound, $\Delta\theta$, for the polar angle by using the new value of r_g in Equation (A.32).

Step 10: test to see if the path length $(r_{Tg} + r_g)/2$ matches the desired range, r_I , to the required accuracy. If not, then repeat the process beginning at Step 1 until the accuracy requirement is met. If the accuracy requirement is met then proceed to Step 11 and stop the iteration.

Step 11: Assign the final guess values as the intersection point, $\vec{P} = (X_I, Y_I, Z_I) = (X_g, Y_g, Z_g)$, transform the coordinates of the intersection point back to the receive antenna coordinate system, and calculate the polar angle to the intersection point:

$$\theta_I = \cos\left(\frac{z_I}{\sqrt{x_I^2 + y_I^2 + z_I^2}}\right) \quad (\text{A.46})$$

Annex B Implementation of Range-Doppler Algorithm

Image formation processing can be used to create an image from the simulated in-phase and quadrature signal samples. Ideally, this image will be representative of the surface reflectivity field that was used as input to generate the simulated signals. In reality, there will be some differences. Regardless, a useful test of the simulation accuracy is to compare the image formed from the simulated signals, or a reflectivity field derived from it, with the inputted reflectivity field. A good comparison and an explanation of the differences will provide confidence in the simulation.

Image data are generated for this document using the basic Range-Doppler Algorithm (RDA) described in Figure 6.1 of [14]. This version of the RDA requires that the radar squint angle is relatively small. The main steps of the algorithm include range compression, range cell migration correction, and azimuth compression. RDA is a well-known algorithm that has been in use for over forty years. The purpose of this annex is to document the assumptions that have been made in this particular implementation and to provide a reference for later use.

B.1 Range compression

The range compression process is performed in the range-frequency, azimuth-time domain. The required frequency domain matched filter is calculated using option 2 discussed in Section 3.4 of [14]. That is, the matched filter is the complex conjugate of the DFT of the zero-padded pulse replica,

$$\tilde{H}_{Rm} = (\sqrt{N_p} \mathbf{DFT}\{\tilde{V}_{Rm}\})^* \quad (\text{B.1})$$

where $\sqrt{N_p}$ is a normalization factor, based on the DFT definition in Equation (62), designed to preserve the correct signal magnitude, the tilde (\sim) symbol denotes zero-padding, and the $*$ operator denotes complex conjugation. The subscript R is only used to indicate correspondence to the pulse replica. The zero-padded pulse replica is calculated as in Equation (58), i.e.,

$$\tilde{V}_{Rm} = \begin{cases} \exp(j \pi K_p \tau_m^2) & \text{for } 0 \leq m \leq T_p f_s - 1 \\ 0 + j0 & \text{for } T_p f_s \leq m \leq N_p - 1 \end{cases} \quad (\text{B.2})$$

The radar sampling frequency, f_s , is chosen such that $T_p f_s$ is an integer. The time variable τ_m is calculated as

$$\tau_m = \frac{m}{f_s} \quad \text{for } i = 0, 1, \dots, N_p - 1 \quad (\text{B.3})$$

where the number of elements in the zero-padded pulse replica, N_p , is given by

$$N_p = 2^{\left\lceil \frac{\ln(M+T_p f_s - 1)}{\ln(2)} \right\rceil} \quad (\text{B.4})$$

The operator $\lceil \cdot \rceil$ returns the nearest larger integer of its argument.

Range-compressed data corresponding to the n^{th} transmitted pulse are then calculated as

$$\tilde{V}'_{mn} = \frac{\mathbf{DFT}_m^{-1} \{ \tilde{H}_{RM} \mathbf{DFT}_m \{ \tilde{V}_{mn} \} \sqrt{N_p} \}}{\sqrt{N_p}} \quad \text{H}$$

where the subscript m applied to the DFT indicates that the transform is calculated across the dimension corresponding to the m index (range-time), and the zero-padded received signal is given by

$$\tilde{V}_{mn} = \begin{cases} V_{mn} & \text{for } 0 \leq m \leq M - 1 \\ 0 + j0 & \text{for } M \leq m \leq N_p - 1 \end{cases} \quad (\text{B.5})$$

where the V_{mn} are the signal samples calculated, for example, in Equations (42), (61), and (82). The values of \tilde{V}'_{mn} corresponding to $M \leq m \leq N_p - 1$ are then cast off to leave only V'_{mn} corresponding to $0 \leq m \leq M - 1$. In addition, to register targets correctly in range the values of V'_{mn} are shifted in range (fast-time) by $T_p f_s / 2$ elements. That is, the range-compressed signal samples in the M range bins of interest are given by

$$V'_{mn} = \begin{cases} 0 + j0 & \text{for } 0 \leq m \leq \frac{T_p f_s}{2} - 1 \\ \tilde{V}'_{\left(m - \frac{T_p f_s}{2}\right)n} & \text{for } \frac{T_p f_s}{2} \leq m \leq M - 1 \end{cases} \quad (\text{B.6})$$

B.2 Range cell migration correction

Range cell migration correction is performed in the range-Doppler domain (range-time, azimuth-frequency). The range-Doppler data, \tilde{H}'_{mn} , are calculated from the zero-padded range-compressed data, \tilde{V}'_{mn} , using discrete Fourier transforms across the azimuth-time (slow-time) dimension, i.e.,

$$\tilde{H}'_{mn} = \mathbf{DFT}_n \{ \tilde{V}'_{mn} \} \sqrt{N_c} \quad (\text{B.7})$$

where in this case the zero-padded range-compressed data are given by

$$\tilde{V}'_{mn} = \begin{cases} V'_{mn} & \text{for } 0 \leq n \leq N_c - 1 \\ 0 + j0 & \text{for } N_c \leq n \leq N_p - 1 \end{cases} \quad (\text{B.8})$$

and

$$N_p = 2^{\left\lceil \frac{\ln(N_c)}{\ln(2)} \right\rceil} \quad (\text{B.9})$$

The result is then shifted so that the zero-frequency component is at the centre of the array, i.e.,

$$\tilde{H}'_{mn} \rightarrow \begin{cases} \tilde{H}'_{m(n+\frac{N_p}{2}+1)} & \text{for } 0 \leq n \leq \frac{N_p}{2} - 2 \\ \tilde{H}'_{m(n-\frac{N_p}{2}+1)} & \text{for } \frac{N_p}{2} - 1 \leq n \leq N_p - 1 \end{cases} \quad (\text{B.10})$$

The Doppler frequencies associated with the \tilde{H}'_{mn} are adjusted for the range-dependent Doppler centroid frequency, f_{Dm} . That is, the Doppler frequencies are given by

$$f_{mn} = \begin{cases} \frac{(n + n_D)}{N_p T_s} - \frac{1}{2 T_s} + f_{Dm} & \text{for } 0 \leq n \leq N_p - n_D \\ \frac{[n - (N_p - n_D)]}{N_p T_s} - \frac{1}{2 T_s} + f_{Dm} & \text{for } N_p - n_D + 1 \leq n \leq N_p - 1 \end{cases} \quad (\text{B.11})$$

where

$$n_D = \begin{cases} \lfloor -f_{Dm} N_p T_s + 0.5 \rfloor & \text{for } -f_{Dm} N_p T_s \geq 0 \\ \lceil -f_{Dm} N_p T_s + 0.5 \rceil & \text{for } -f_{Dm} N_p T_s < 0 \end{cases} \quad (\text{B.12})$$

and f_{Dm} is provided in the RADARSAT-2 metadata. Again, the operator $\lfloor \cdot \rfloor$ returns the nearest smaller integer of its argument and the operator $\lceil \cdot \rceil$ returns the nearest larger integer of its argument.

The range migration experienced by a stationary target as the SAR passes can be estimated from the Doppler frequencies as

$$\delta r_{mn} = \frac{\lambda_c^2 r_m f_{mn}^2}{8 v_{em}^2} \quad (\text{B.13})$$

where the effective SAR velocity is given by

$$v_{em} = \sqrt{\frac{K_{am} \lambda_c r_m}{2}} \quad (\text{B.14})$$

Equation (B.14) assumes that the rectilinear squint angle at the time of beam centre crossing is small enough such that the cosine squared of this angle is approximately 1 (see Equations 4.38 and 6.7 of [14]). The Doppler rate values, K_{am} , are provided in the RADARSAT-2 metadata. The range cell migration can be calculated as

$$\delta m_{mn} = \frac{2 f_s \delta r_{mn}}{c} \quad (\text{B.15})$$

Given the above quantities the range-Doppler data are adjusted for range-cell migration using a sine cardinal function (sinc or sampling function) interpolation process, i.e.,

$$\tilde{H}_{mn}'' = \sum_{i=m + \lceil \delta m_{mn} \rceil - \frac{N_i}{2}}^{m + \lceil \delta m_{mn} \rceil + \frac{N_i}{2} - 1} \frac{w_{Ki} \sin[\pi(m + \delta m_{mn} - i)]}{\pi(m + \delta m_{mn} - i)} \tilde{H}_{in}' \quad (\text{B.16})$$

where the number of interpolates, N_i , is a user defined parameter, and the weights w_{Ki} apply a Kaiser window with smoothing coefficient β_K to the sinc function. That is,

$$w_{Ki} = \frac{I_0 \left(\beta_K \sqrt{1 - \left[\frac{2i}{(T_p f_s - 1)} - 1 \right]^2} \right)}{I_0(\beta_K)} \quad (\text{B.17})$$

where I_0 is the zero-order I Bessel function, and β_K is a user defined parameter.

The \tilde{H}_{mn}'' are then repositioned with respect to Doppler frequency so that they can be transformed back to the time domain, i.e.,

$$\tilde{H}_{mn}'' \rightarrow \begin{cases} \tilde{H}_{m(n+\frac{N_p}{2}-1)}'' & \text{for } 0 \leq n \leq \frac{N_p}{2} \\ \tilde{H}_{m(n-\frac{N_p}{2}-1)}'' & \text{for } \frac{N_p}{2} + 1 \leq n \leq N_p - 1 \end{cases} \quad (\text{B.18})$$

The zero-padded time domain data are then calculated as

$$\tilde{V}_{mn}'' = \frac{\mathbf{DFT}^{-1}\{\tilde{H}_{mn}''\}}{\sqrt{N_p}} \quad (\text{B.19})$$

Finally, the excess data are cast off to give the time domain data, after range compression and range cell migration correction, as

$$V_{mn}'' = \tilde{V}_{mn}'' \quad \text{for } 0 \leq n \leq N_c - 1 \quad (\text{B.20})$$

B.3 Azimuth compression

The first step in the azimuth compression process is to determine the length of the filter to be used such that an appropriate azimuth oversampling ratio is achieved. A typical oversampling ratio, α_a , is between 1.1 and 1.4 [14]. The azimuth oversampling ratio is calculated as the ratio of the pulse repetition frequency to the Doppler bandwidth, B_f , associated with the filter length, or equivalently

$$\alpha_{am} = \frac{1}{T_s B_{fm}} \quad (\text{B.21})$$

An initial estimate for the filter length, L'_{fm} , corresponding to the m^{th} range bin, is calculated based on the slow-time interval for which a stationary target is within the average one-way 3 dB azimuth beamwidth, i.e.,

$$L'_{fm} = \left\lceil \frac{2 r_m}{v_{gm} T_s} \tan\left(\frac{\bar{\phi}_3}{2}\right) + 0.5 \right\rceil \quad (\text{B.22})$$

where $\bar{\phi}_3$ is the 3 dB beamwidth corresponding to $\sqrt{f_{\phi_T}^2(\phi_T, \phi_b) f_{\phi}^2(\phi, \phi_b)}$. The SAR beam velocity on the ground is given by (Equation (4.10) of [14])

$$v_{gm} = \frac{v_{em}^2}{|\vec{v}_p|} \quad (\text{B.23})$$

The Doppler bandwidth corresponding to this initial filter length estimate is given by

$$\begin{aligned} B'_{fm} = & \frac{2 v_{gm}}{\lambda_c} \sin \left(\tan^{-1} \left\{ \frac{v_{em}}{r_m} \left[t_{Dm} + \frac{(L'_{fm} - 1) T_s}{2} \right] \right\} \right) - \dots \\ & \dots \frac{2 v_{gm}}{\lambda_c} \sin \left(\tan^{-1} \left\{ \frac{v_{em}}{r_m} \left[t_{Dm} - \frac{(L'_{fm} - 1) T_s}{2} \right] \right\} \right) \end{aligned} \quad (\text{B.24})$$

where the Doppler centroid time, t_{Dm} , is calculated as

$$t_{Dm} = \frac{-\lambda_c r_m f_{Dm}}{2 V_{em}^2} \quad (\text{B.25})$$

This gives an initial estimate for the oversampling ratio as

$$\alpha'_{am} = \frac{1}{T_s B'_{fm}} \quad (\text{B.26})$$

If α'_{am} is within the range $\alpha_{al} \leq \alpha'_{am} \leq \alpha_{au}$, where α_{al} and α_{au} are user defined parameters representing the upper and lower bounds of acceptable azimuth oversampling ratio, respectively, (e.g., $\alpha_{al} = 1.1$, $\alpha_{au} = 1.4$), then the estimated filter length is accepted, i.e., $L_{fm} = L'_{fm}$. Otherwise, α_{am} is set to

$$\alpha_{am} = \begin{cases} \alpha_{al} & \text{for } \alpha'_{am} \leq \alpha_{al} \\ \alpha_{au} & \text{for } \alpha'_{am} \geq \alpha_{au} \end{cases} \quad (\text{B.27})$$

and L_{fm} is calculated as

$$L_{fm} = \left\lceil \frac{\lambda_c r_m}{2 V_{em}^2 \alpha_{am} T_s^2} + 0.5 \right\rceil \quad (\text{B.28})$$

Given the filter length, the signal replica required for azimuth compression is then calculated as

$$\tilde{V}_{Rmn}'' = \begin{cases} \exp\left(-j \frac{4\pi r_{fmn}}{\lambda_c}\right) & \text{for } 0 \leq n \leq L_{fm} - 1 \\ 0 + j0 & \text{for } L_{fm} \leq n \leq N_p - 1 \end{cases} \quad (\text{B.29})$$

where

$$r_{fmn} = \sqrt{r_m^2 + v_{em}^2 t_{fmn}^2} \quad (\text{B.30})$$

and slow-time relative to the Doppler centroid is given by

$$t_{fmn} = n T_s + t_{Dm} - \frac{T_s (L_{fm} - 1)}{2} \quad \text{for } n = 0, 1, 2, \dots, L_{fm} - 1 \quad (\text{B.31})$$

The padded length of the azimuth signal replica is given by

$$N_p = 2^{\left\lceil \frac{\ln(N_c + L_{fm} - 1)}{\ln(2)} \right\rceil} \quad (\text{B.32})$$

The azimuth matched filter is then calculated as

$$\tilde{H}_{Rmn}'' = (\sqrt{N_p} \mathbf{DFT}_n\{\tilde{V}_{Rmn}''\})^* \quad (\text{B.33})$$

Azimuth compression is performed as

$$\tilde{V}_{mn}''' = \frac{\mathbf{DFT}_n^{-1}\{\tilde{H}_{mn}'' \tilde{H}_{Rmn}''\}}{\sqrt{N_p}} \quad (\text{B.34})$$

where

$$H_{mn}'' = \sqrt{N_p} \mathbf{DFT}_n\{\tilde{V}_{mn}''\} \quad (\text{B.35})$$

and

$$\tilde{V}_{mn}'' = \begin{cases} V_{mn}'' & \text{for } 0 \leq n \leq N_c - 1 \\ 0 + j0 & \text{for } N_c \leq n \leq N_p - 1 \end{cases} \quad (\text{B.36})$$

Excess samples are then cast off and the result is shifted in slow-time to correctly register the compressed data in azimuth, i.e.,

$$V'''_{mn} = \begin{cases} 0 + j0 & \text{for } 0 \leq n \leq n_0 - 1 \\ \tilde{V}'''_{m(n-n_0)} & \text{for } n_0 \leq n \leq N_c - 1 \end{cases} \quad (\text{B.37})$$

where

$$n_0 = \left\lfloor \frac{L_{fm} - 1}{2} - t_{Dm} T_s + 0.5 \right\rfloor \quad (\text{B.38})$$

The V'''_{mn} are the final range and azimuth compressed data. SAR image amplitude can be calculated from these data as

$$A_{Imn} = |V'''_{mn}|^{x_c} \quad (\text{B.39})$$

where $x_c = 1$. The contrast of the image can be increased by decreasing the x_c value (typically to ~ 0.1).

B.4 Geolocation

Although not part of the RDA, the resulting compressed data must be positioned correctly in range (fast-time) and cross-range (azimuth or slow-time). The correct absolute range values are

$$r_m = m \frac{c}{2 f_s} + r_N \quad (\text{B.40})$$

where r_N is the slant range to the near edge of the image provided in the RADARSAT-2 metadata. The m index in Equation (B.40) will correspond to the pixel index of the image.

The data must be similarly adjusted in azimuth to align the data with the zero-Doppler time of the first image line, i.e.,

$$V'''_{mn} \rightarrow \begin{cases} V'''_{m(n+n_{zD})} & \text{for } 0 \leq n \leq N_c - n_{zD} \\ 0 + j0 & \text{for } N_c - n_{zD} + 1 \leq n \leq N_c - 1 \end{cases} \quad (\text{B.41})$$

where

$$n_{zD} = \left\lfloor \frac{t_{zD}}{T_s} + 0.5 \right\rfloor \quad (\text{B.42})$$

and t_{zD} is the zero-Doppler time of the first image line provided in the RADARSAT-2 metadata. The n index will now correspond to the line index of the image.

List of symbols/abbreviations/acronyms/initialisms

ADC	Analogue-to-Digital Converter
CEOS	Committee for Earth Observation Satellites
DFT	Discrete Fourier Transform
DRDC	Defence Research and Development Canada
IDL	Interactive Data Language
MDA	MacDonald, Dettwiler and Associates
MODEX	Moving Object Detection EXperiment
NITF	National Imagery Transmission Format
PDF	Probability Density Function
PRF	Pulse Repetition Frequency
RCS	Radar Cross Section
RDA	Range-Doppler Algorithm
RSE	Radar Sensing and Exploitation
SAR	Synthetic Aperture Radar
STK	Systems ToolKit
TIFF	Tag Image File Format
WGS	World Geodetic System

DOCUMENT CONTROL DATA		
*Security markings for the title, authors, abstract and keywords must be entered when the document is sensitive		
1. ORIGINATOR (Name and address of the organization preparing the document. A DRDC Centre sponsoring a contractor's report, or tasking agency, is entered in Section 8.) DRDC – Ottawa Research Centre Defence Research and Development Canada, Shirley's Bay 3701 Carling Avenue Ottawa, Ontario K1A 0Z4 Canada		2a. SECURITY MARKING (Overall security marking of the document including special supplemental markings if applicable.) CAN UNCLASSIFIED
		2b. CONTROLLED GOODS NON-CONTROLLED GOODS DMC A
3. TITLE (The document title and sub-title as indicated on the title page.) Simulation of Raw Digital Signals Received by Space-Based Synthetic Aperture Radar for use in Jamming Studies		
4. AUTHORS (Last name, followed by initials – ranks, titles, etc., not to be used) Thomson, A. D.		
5. DATE OF PUBLICATION (Month and year of publication of document.) June 2019	6a. NO. OF PAGES (Total pages, including Annexes, excluding DCD, covering and verso pages.) 117	6b. NO. OF REFS (Total references cited.) 27
7. DOCUMENT CATEGORY (e.g., Scientific Report, Contract Report, Scientific Letter.) Scientific Report		
8. SPONSORING CENTRE (The name and address of the department project office or laboratory sponsoring the research and development.) DRDC – Ottawa Research Centre Defence Research and Development Canada, Shirley's Bay 3701 Carling Avenue Ottawa, Ontario K1A 0Z4 Canada		
9a. PROJECT OR GRANT NO. (If appropriate, the applicable research and development project or grant number under which the document was written. Please specify whether project or grant.) 05bb	9b. CONTRACT NO. (If appropriate, the applicable number under which the document was written.)	
10a. DRDC PUBLICATION NUMBER (The official document number by which the document is identified by the originating activity. This number must be unique to this document.) DRDC-RDDC-2018-R297	10b. OTHER DOCUMENT NO(s). (Any other numbers which may be assigned this document either by the originator or by the sponsor.)	
11a. FUTURE DISTRIBUTION WITHIN CANADA (Approval for further dissemination of the document. Security classification must also be considered.) Public release		
11b. FUTURE DISTRIBUTION OUTSIDE CANADA (Approval for further dissemination of the document. Security classification must also be considered.)		
12. KEYWORDS, DESCRIPTORS or IDENTIFIERS (Use semi-colon as a delimiter.) Space based Radars; Synthetic Aperture Radar (SAR); signal; modelling & simulations		

13. ABSTRACT (When available in the document, the French version of the abstract must be included here.)

A simulation of digital signals produced by a space-based Synthetic Aperture Radar (SAR) receiver is developed to provide a source of raw signal data that can be used to assess the vulnerability of space-based SAR to jamming and to investigate protection measures that may allow space-based SAR to operate in a contested electromagnetic environment. Key features of the simulation are a flexible time-domain approach, rotating spheroidal Earth geometry, calculation of absolute signal magnitudes, and the ability to generate large scenes. These are required so that jamming signals with specific quantitative properties (e.g., transmitted power) can be easily introduced into the simulation environment for specific geometries of interest and so that the effects of the jamming can be properly assessed in a quantitative fashion. The simulation uses the metadata of an actual space-based SAR collection to define the geometry for a given case. The image data corresponding to the real SAR collection is used to define the Earth surface reflectivity field that is measured by the simulated space-based SAR. Signal data corresponding to the surface of the earth, radar system noise, and test targets are generated, coherently combined, and converted into digital signals that can be processed using SAR image formation algorithms. An option to decompress and scale real, raw, range-compressed signals, measured by the RADARSAT-2 MODEX mode and combine them with test target signals is also developed. The scaling of the real data is required to adjust the absolute magnitudes of data measured in the real world to the levels that would be measured in the simulated environment. This option allows the validity of the simulated signals to be assessed through comparison with real data. The accuracy of the simulation is evaluated by comparing the properties of simulated signals and images with theoretical expectations and with the properties of real signal and image data. Good agreement is achieved for all aspects compared. This provides confidence that the simulated signals effectively approximate realistic raw received SAR signals and that the simulation can be used for its stated purpose.

La simulation des signaux numériques produits par un récepteur radar à synthèse d'ouverture (RSO) spatial fournit une source de données brutes pouvant servir à évaluer sa vulnérabilité au brouillage et à explorer les mesures de protection qui lui permettraient de fonctionner dans un environnement électromagnétique contesté. Les principales caractéristiques d'une telle simulation sont la souplesse de l'approche utilisée dans le domaine temporel, la géométrie sphéroïdale de la Terre en rotation, le calcul de l'amplitude absolue des signaux et la capacité de générer des scènes radar de grandes dimensions. Ces caractéristiques facilitent l'intégration des signaux de brouillage aux propriétés quantitatives spécifiques (p. ex., la puissance d'émission) dans l'environnement de simulation des géométries à l'étude et permettent d'évaluer correctement les effets du brouillage sur le plan quantitatif. Durant la simulation, les géométries sont définies à partir des métadonnées fournies par un ensemble de RSO spatiaux réels. Les données d'image réelles permettent de définir le champ de réflectivité de la surface de la Terre qui est mesuré par le RSO spatial simulé. Les données sur la surface de la Terre, le bruit radar et les cibles d'essai sont alors générées, combinées de façon cohérente et converties en signaux numériques pouvant être traités au moyen d'algorithmes de formation d'images RSO. Une option permettant de décompresser les signaux à compression de portée bruts réels mesurés en mode MODEX de RADARSAT-2, de les mettre à l'échelle et de les combiner aux signaux des cibles d'essai est également en cours de conception. En effet, les données réelles doivent être mises à l'échelle pour que l'amplitude absolue mesurée dans le monde réel reflète celle qui serait mesurée dans l'environnement de simulation. Cette option permet donc d'évaluer la validité des signaux simulés en les comparant avec des données réelles. Pour évaluer la précision de la simulation, on compare les propriétés des signaux et des images simulés avec les attentes théoriques et les propriétés des signaux et des images réels. La concordance observée entre tous les aspects comparés confirme que les signaux simulés se rapprochent effectivement des signaux RSO bruts réellement reçus et que la simulation peut être utilisée aux fins prévues.